

STRUCTURAL AND OPTICAL  
PROPERTIES OF SEMICONDUCTOR  
NANOPARTICLE CLUSTERS

**Dissertation**

zur Erlangung des Doktorgrades  
des Fachbereiches Chemie  
der Universität Hamburg

vorgelegt von

**Mona Rafipoor**

Hamburg  
2018

Evaluators of the dissertation: Prof. Dr. Holger Lange  
Prof. Dr. Stephanie Reich

Evaluators of the disputation: Prof. Dr. Holger Lange  
Prof. Dr. Ralph Holl  
PD. Dr. Tobias Kipp

Date of the disputation: October 12<sup>th</sup>, 2018

# Abstract

The properties of semiconductor nanocrystals depend not only on their chemical composition, but also on their size and shape. In order to improve the optical properties of nanocrystals, these are often synthesized as core/shell structures. Where the shell nanocrystal can improve the surface passivation of the core nanocrystal. However, differences of the crystal structures of core and shell may lead to a lattice mismatch at the core/shell interface. This can result in compressive or tensile strain in the core and the shell, which leads to the formation of surface traps, alters the emission properties of the nanocrystals and reduces the fluorescence quantum efficiency. Instead of using one material for the shell, one can use an alloy of components to gradually adjust the lattice constant between the core and the shell. Concerning applications core/shell nanocrystals are usually used as ensembles. Because of the small interparticle distance in such ensembles, potential interaction between the nanocrystals in ensembles are an important issue.

The focus of this dissertation is on the spectroscopic investigation of the structural and optical properties of such semiconductor nanocrystals. To enable optimizations towards applications Raman spectroscopy is used to determine the strain in InP/(Zn,Cd)Se core/shell quantum dots. Here, the longitudinal optical phonon's frequency changes with inherent the strain. Tracking the longitudinal optical phonon frequencies helps to adjust the shell compositions.

Within the ensembles of nanocrystals, the distance between the nanocrystals can affect their interaction behavior. Förster resonance energy transfer (FRET) is a possible interaction between neighboring nanocrystals. In highly excited nanocrystals, multiexcitons can recombine nonradiatively and compete with the energy transfer. CdSe/CdS quantum dots/quantum rods encapsulated in amphiphilic micelles with inter-particle distance control by spacer ligands are used as a model system. Photoluminescence spectroscopy accompanied by transient absorption spectroscopy shows that at exciton populations of approximately one per nanocrystal, energy transfer between the nanocrystals can lead to generation of multiexcitons in neighboring nanocrystals. The generated multiexciton can recombine nonradiatively. This is unfavorable for solar cells. Photogenerated carrier have to be extracted in order to generate electric power and the generated multiexciton annihilates the photogenerated carriers before they can be extracted. In this thesis, the duration

of the charge separation is investigated by transient absorption spectroscopy. Low concentration of nanocrystals and interparticle distances of  $> 7.9$  nm can present the generation of transferred multiexcitons, thus allowing to tune the conditions for a high-yield extraction of photogenerated carriers.

# Zusammenfassung

Die Eigenschaften von Halbleiternanokristallen hängen neben ihrer chemischen Zusammensetzung auch von ihrer Größe und Form ab. Um die Photolumineszenzeigenschaften von Nanokristallen zu verbessern, werden diese häufig in Form von Kern/Schale Strukturen synthetisiert. Dadurch verringert sich die Anzahl an Fehlstellen an der Oberfläche des Kerns, was es zur Verbesserung der Photolumineszenzeigenschaften führt. Die Materialunterschiede der beiden Halbleiter von Kern und Schale können jedoch aufgrund unterschiedlicher Gitterkonstanten zu einer Gitterfehlanpassung an der Grenzfläche führen. Die Gitterfehlanpassung führt zu einer Druck- oder Zugspannung im Kern und der Schale, wodurch sich die Emissionseigenschaften der Nanokristalle verändern und die Fluoreszenz-Quantenausbeute verringert wird. Anstatt lediglich ein Material als Schale zu nutzen, ist es auch möglich die Schale aus einer Legierung von weiteren Komponente herzustellen um so den Gitterparameter kontinuierlich anzupassen und so die Spannungen zu verringern. Kern/Schale-Nanokristalle liegen üblicherweise nicht einzeln und isoliert vor, sondern werden je nach Anwendungsbereich in großen Mengen und mit geringer Distanz zueinander verwendet. Daher ist die Wechselwirkung und gegenseitige Beeinflussung (kollegiale Wechselwirkungen) zwischen den Nanokristallen in Ensembles ein wichtiges Thema.

Der Fokus dieser Dissertation liegt auf der spektroskopischen Untersuchung und dem Verständnis der optischen Eigenschaften von Halbleiternanokristallen im Ensemble. In dieser Arbeit wird die Raman-Spektroskopie zur Bestimmung der Verspannung in InP/(Zn,Cd) Se Kern/Schale-Quantenpunkten verwendet, welche von der Änderung des Gitterparameters rührt und durch eine Verschiebung der longitudinale optische Phononenfrequenz nachweisbar ist. Dementsprechend hilft die Verfolgung der longitudinalen optischen Phononenfrequenzen zur kontinuierlichen Anpassung der Verspannungen. Zeitaufgelöste Photolumineszenz Spektroskopie wurde durchgeführt um die optischen Eigenschaften von Kern/Schale Nanokristallensembles zu untersuchen.

Wechselwirkungen zwischen Nanokristallen in Ensembles können die optischen Eigenschaften der Nanokristalle beeinflussen. Dabei ist der Abstand zwischen den Nanokristallen in einem Ensemble ein signifikanter Parameter, welcher das Wechselwirkungsverhalten beeinflusst. Der Förster-Resonanz-Energie-Transfer (FRET) ist eine mögliche Wechselwirkung zwischen naheliegende benachbarten Nanokristallen. Bei einem Abstand von unter 10 nm

kommt es zu einer Energieübertragung von kleineren zu größeren Nanokristallen. In hochangeregten Nanokristallen können Multiexzitonen nichtstrahlend rekombinieren und mit dem Energietransferprozess konkurrieren. Als Referenzmaterialien für diese Untersuchungen dienen CdSe/CdS Quantenpunkte/Quantenstäbe, die in amphiphilen Mizellen verkapselt sind und deren Abstand innerhalb der Mizelle durch Liganden genau eingestellt werden konnten. Photolumineszenzspektroskopie und transiente Absorptionsspektroskopie zeigen, dass bei einer Exzitonenpopulationen von ungefähr eins der Energietransfer zwischen den Nanokristallen zur Erzeugung von Multiexziton führen kann. Das erzeugte Multiexziton kann zur Vernichtung der photogenertierten Ladungen in den Nanokristallen führen. In Solarzellen müssen photogenerierte Ladungsträger extrahiert werden, um Elektrizität zu erzeugen. Das erzeugte Multiexziton kann jedoch die photogenerierten Ladungen vernichten, bevor sie extrahiert werden können. In dieser Dissertation wurde die Ladungstrennungsdauer durch transiente Absorptionsspektroskopie untersucht. Eine niedrige Konzentration der Nanokristalle und ein Abstand größer als 7.9 nm zwischen den Nanokristallen kann das Problem beheben, was es ermöglicht, die Effizienz von Nanokristallen-basierten Solarzellen präzise zu optimieren.

# List of Publications

Part of this thesis have already been published:

Coupled multiexciton and energy transfer dynamics in dense nanocrystal ensembles.

Mona Rafipoor, Rieke Koll, Jan Philip Merkl, Lisa Sarah Fruhner, Horst Weller, Holger Lange.

*Submitted.*

Strain Engineering in InP/(Zn,Cd) Se Core/Shell Quantum Dots.

Mona Rafipoor, Dorian Dupont, Hans Tornatzky, Mickael D. Tessier, Zeger Hens, Janina Maultzsch, Holger Lange.

*Chemistry of Materials* 30, 4393-4400 ( **2018**).

Clustering of CdSe/CdS Quantum Dot/Quantum Rods into Micelles Can Form Bright, Non-blinking, Stable, and Biocompatible Probes.

Mona Rafipoor, Christian Schmidtke, Christopher Wolter, Christian Strelow, Horst Weller, Holger Lange.

*Langmuir* 31, 9441 (**2015**).

## Further Publications

Ultrastable, Zerodur-based optical benches for quantum gas experiments.

Hannes Duncker, Ortwin Hellmig, André Wenzlawski, Alexander Grote, Amir Jones Rafipoor, Mona Rafipoor, Klaus Sengstock and Patrick Windpassinger.

*Applied Optics* 53, 4468 (**2014**).



# Contents

<b>Abstract</b>	<b>3</b>
<b>Zusammenfassung</b>	<b>5</b>
<b>List of Publications</b>	<b>7</b>
<b>1 Introduction</b>	<b>11</b>
<b>2 Semiconductor Nanocrystals</b>	<b>15</b>
2.1 Fundamentals . . . . .	15
2.2 Synthesis . . . . .	18
2.2.1 Core/Shell Nanocrystals . . . . .	20
2.2.2 Core/Shell QDs Alloy . . . . .	21
2.2.3 Micelles . . . . .	24
2.3 Methods . . . . .	28
2.3.1 Raman Spectroscopy . . . . .	28
2.3.2 Time-resolved Photoluminescence Spectroscopy . . . . .	31
2.3.3 Transient Absorption Spectroscopy . . . . .	35
<b>3 Structural properties of Core/Shell Quantum Dots</b>	<b>41</b>
3.1 Optical Phonons of Core/Shell QDs . . . . .	41
3.2 Strain in Core/Shell QDs . . . . .	42
<b>4 Optical properties of Core/Shell Quantum Dots/Quantum Rods in Micelles</b>	<b>49</b>
4.1 Blinking . . . . .	49
4.2 Photoluminescence Spectra and Decays . . . . .	52
4.3 Stability and Possible Interparticle Interactions . . . . .	53
<b>5 Inter-Particle Interactions between Core/Shell Quantum Dots/Quantum Rods</b>	<b>57</b>
5.1 Nonradiative Recombination Channels in QDs/QRs . . . . .	57
5.1.1 Förster Resonance Energy Transfer . . . . .	57

5.1.2	Auger Recombination . . . . .	59
5.2	Coupled Auger Recombination and Energy Transfer . . . . .	60
5.2.1	Characterization of the Encapsulated QDs/QRs . . . . .	60
5.2.2	Biexciton Generation . . . . .	62
5.2.3	Förster Resonance Energy Transfer Analysis . . . . .	64
5.2.4	Coupled Förster Resonance Transfer and Auger Recombination . . . . .	66
<b>6</b>	<b>Charge Separation in Quantum Dots</b>	<b>73</b>
6.1	Coupling of CdSe QDs to Methyl Viologen . . . . .	73
6.1.1	Transient Absorption Dynamics of Charge Transport . . . . .	73
6.1.2	Photoluminescence of CdSe QDs coupled to Methyl Viologen . . . . .	77
<b>7</b>	<b>Summary</b>	<b>79</b>
<b>8</b>	<b>Bibliography</b>	<b>81</b>
	<b>Appendix</b>	<b>99</b>
	Chemicals . . . . .	110
	Danksagung . . . . .	111
	Eidesstattliche Versicherung . . . . .	112

# 1 Introduction

Colloidal semiconductor nanocrystals are tiny light emitting particles with a regular crystal structure and an average size of around 10 nm, which can equate to 10000 atoms. Their optical and electronic properties are size and shape dependent,[1] which makes them very popular for different applications such as optoelectronic devices, light emitting diodes, photodetectors, solar energy conversion and biosensing.[2–6] The fluorescence of the nanocrystals plays the main role in light emitting diodes.[7–9] The nanocrystals can also be used as fluorescence markers for medical purposes.[10, 11] For applications such as solar energy conversion, semiconductor nanocrystals are mainly used for converting light to electrical energy. Beside their widespread potential applications, they are also a popular material for fundamental research. The nanocrystals can be fabricated in high amounts and narrow size distributions in solution. They are made of binary (II-VI and III-V ) compounds such as ZnS, ZnSe, CdS, CdSe, InP.

One of the most extensively investigated nanocrystal material is CdSe, because of advanced large-scale preparation possibilities and its band gap in the visible spectrum. The full visible spectrum can be achieved by tuning the nanocrystal sizes. The electrons in such nanocrystals can be confined over a different number of dimensions. Confining them in 3 dimensions leads to the fabrication of quantum dots, a confinement in two dimensions leads to quantum wires or rods, and a confinement in one dimension leads to the fabrication of quantum wells or disks. The higher the number of confined dimensions the stronger the electronic confinement of the nanocrystals, leading to a wider range in the band gap tunability.

The small size of the nanocrystals leads to an increase in the number of atoms at the surface, which are incompletely bonded to the other atoms in the crystal structure. These surface atoms disrupt the periodicity of the crystal lattice and can lead to dangling orbitals. The nanocrystal surface is unpassivated, which may also form a similar states in addition to the actual nanocrystal band structure.[12, 13] If these formed energy states are within the nanocrystal band gap, it can lead to a trapping of charge carriers.[14–16] This surface trapping of the nanocrystals influences their electrical and optical properties and leads to an on/off fluorescence intensity behavior, also called blinking behavior.

To increase the amount of radiative recombination, the overlap between the electrons and

the holes in the semiconductor nanocrystals need to be increased. An advantageous procedure is to coat the nanocrystals with an inorganic shell. The major process is coating them with a wider band gap nanocrystal material forming core/shell nanocrystals. With this approach, the charge carriers in the core remain distant from the surface and the trapping behavior can be reduced. The wider shell band gap insulates the core electronically. For example, coating CdSe with CdS nanocrystals can not only lead to the confinement of the carriers in core, but also the lower oxidation potential of  $S^{-2}$  relative to  $Se^{-2}$ , leading to a surface defect formation threshold.[17]

Most of the semiconductor nanocrystals are synthesized in organic solvents or in the solid phase and stabilized afterwards with hydrophobic ligands (small molecules on the surface). These hydrophobic ligands are not soluble in water, which is a disadvantage for biological applications of the nanocrystals, for example imaging and drug delivery.[10, 11, 18] The nanocrystals can be made water-soluble by using block-copolymer, which will cause them to self-assemble into micelles in water.[19–24]

In this thesis, this method is introduced for reducing the blinking behavior of CdSe/CdS core/shell nanocrystals and increasing their optical stability. The number of nanocrystals encapsulated in micelles can be controlled. In almost all of the applications, the nanocrystals are used as a close packed group of nanocrystals. The encapsulation of nanocrystals in micelles is found also to be a presentation of a good platform for investigating the interaction between the nanocrystals.

This thesis investigates the structural and optical properties of core/shell nanocrystals. This work starts with the fundamental background of semiconductor nanocrystals. The investigated nanocrystals and the methods used in this work are described in Chapter 2. In Chapter 3, Raman spectroscopy used to investigate the structural properties of InP/ZnSe, InP/CdSe and InP/(Zn,Cd)Se core/shell nanocrystals. The core and the shell related longitudinal phonons are studied by Raman spectroscopy to obtain the strain in core and the shell. To eliminate the strain from the interface, the lattice constant of the components are changed step-by-step. A strain free regime at a specific shell components ratio is found.

In Chapter 4, photoluminescence time-resolved spectroscopy is utilized to investigate the optical properties of the nanocrystals. The optical properties of CdSe/CdS core/shell nanocrystals encapsulated in micelles are studied and the optical stability of this material is proven.

In Chapter 5, photoluminescence time and wavelength resolved spectroscopy is used for investigating the possible interaction between the nanocrystals encapsulated in the micelles. Varying the distance between the nanocrystals in the micelles resolved distance-dependent interactions, mainly Förster or fluorescence resonance energy transfer. Multiexciton Auger

---

recombination is investigated by changing the excitation power.

In Chapter 6, another important property of the nanocrystals for their potential application in solar cells is introduced. For this approach, very small CdSe quantum dots are coupled to electron acceptor molecules and the charge transport from CdSe quantum dots to the Methyl Viologen electron acceptor is probed by performing transient absorption spectroscopy.

Chapter 7 concludes the summary of these investigations for an improvement in current nanocrystal applications.



## 2 Semiconductor Nanocrystals

Semiconductor materials are defined by their band structure. The following Chapter introduces the basic theoretical concept of the semiconductor band structure and the behavior of excited electrons in these materials.

### 2.1 Fundamentals

In general, the band structure defines the states (energy, momentum) an electron can reach, which can be quantum mechanically calculated from the Schrödinger equation. Semiconductor materials are crystals with a periodic structure. The periodic structure is an advantage for calculating the states of electrons in the potential.[25, 26] The wave function of the electron can be defined with the Bloch theorem.[27] The wave function  $\psi_k(r)$  of a free electron is the solution of Schrödinger's equation  $H\psi = \epsilon\psi$ . According to the Bloch theorem for a periodic potential,[28] the Eigenfunctions of the wave equation are the wave function of the free electron multiplied by the Bloch function  $u_k(r)$ , which has the same periodicity as the crystal lattice and therefore can be expanded into a Fourier series with the wave vector of the reciprocal lattice  $G$ .  $u_k(r) = \sum_G C_G \exp(iGr)$  defines a function with the same periodicity of the direct lattice.  $C_G$  represent the plane wave expansion coefficients and specifies the wave functions ( $\psi_k(r)$ ) form.

$$\psi_k(r) = u_k(r) e^{ikr} \quad (2.1)$$

Where  $k$  represents the wave vector.

Assuming just one particular  $G$  in the first Brillouin zone in 2D, the Hamiltonian consist of the kinetic energy term:

$$H = -\frac{\hbar^2}{2m} \nabla^2 \quad (2.2)$$

The wave function for one particular point according to the Bloch function  $u_k(r)$  and equation 2.1 is:

$$\psi(r) = C_G e^{i(k+G)r} \quad (2.3)$$

Applying the Laplacian ( $\nabla^2$ ) operator on the wave function gives

$$\nabla^2 \psi(r) = -(k+G)^2 \psi(r). \quad (2.4)$$

The energy of the electron for just one point in the reciprocal lattice is defined with:

$$E(k) = -\frac{\hbar^2}{2m} \int \psi^*(r) \nabla^2 \psi(r) d^3r \quad (2.5)$$

$$= \frac{\hbar^2}{2m} (k + G)^2 \quad (2.6)$$

According to Equation 2.6  $E(k)$  varies quadratically with  $k$  for each point of the reciprocal

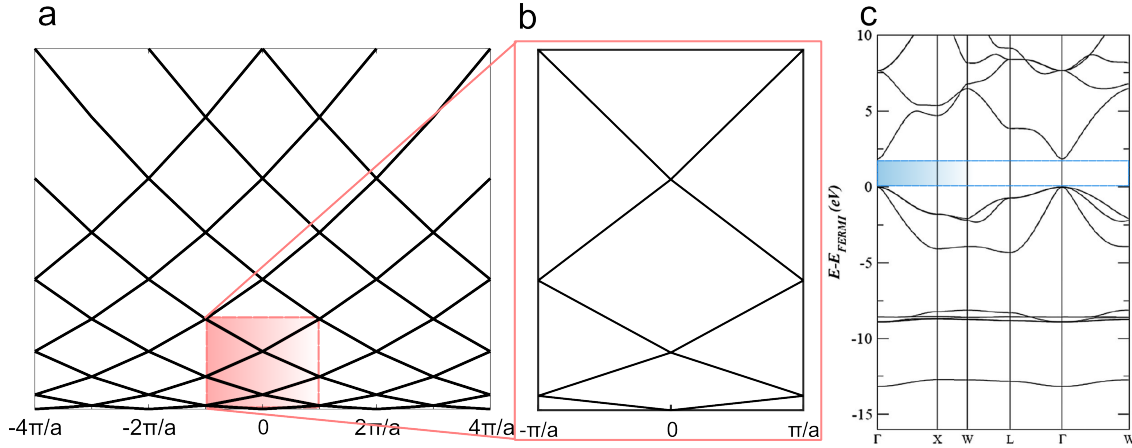


**Figure 2.1:** a) The energy of a free electron  $E(k)$  in 2D cubic reciprocal lattice varies quadratic with the wave vector  $k$ . b) First Brillouin zone (reduced zone scheme).

c) Band structure of CdSe. (Reprinted (adapted) with permission from Investigation of the bulk and surface properties of CdSe: insights from theory, Alexandra Szemjonov, Thierry Pauporté, Ilaria Ciofini and Frédéric Labat. Copyright (2014) Physical Chemistry Chemical Physics.) [29]

lattice, and the lowest energy state occurs at  $G=0$ .

In a lattice, where the reciprocal lattice dose not have a simple cubic form and the Brillouin zones have all possible kinds of shapes in 3D space, the energy of an electron in the energy space is not as simple as Equation 2.6. The change of the energy with the wave vector is called band structure (Figure 2.1 c).

The semiconductor band structures consist of a fully occupied continuous valence band and a mostly unoccupied continuous conduction band with a band gap in between (the blue area in Figure 2.1 c and Figure 2.2). In general photons with sufficient energy can excite the electrons from the valence band (VB) to the conduction band (CB) and leave holes in the valence band behind.

An electron or a hole with a mass  $m$  in the semiconductor responds to an applied field like a free electron but with an effective mass of  $m^*$  given by

$$\frac{1}{m^*} = \frac{1}{\hbar^2} \frac{d^2 \epsilon(k)}{dk^2}, \quad (2.7)$$

where  $\epsilon(k)$  is the energy of the electron near the conduction band or the energy of a hole near the valence band at wave vector  $k$ . A negatively charged electron and a positively

charged hole can be electrostatically bound together via the Coulomb force and can form a so called "exciton".

The possibility for controlling the band gap energy of a semiconductor provides a great control over the optical and electronic properties of this material.[30] Semiconductor Nanocrystals

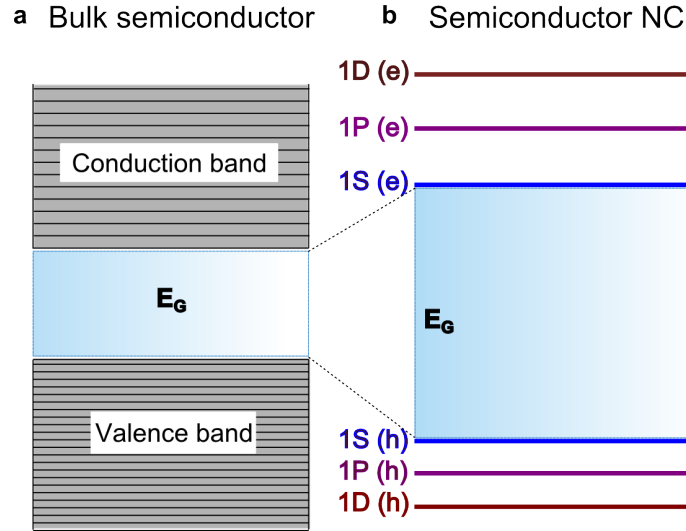


**Figure 2.2:** a) Bulk semiconductor materials consist of continuous conduction and valence bands, separated by a band gap  $E_G$ , while semiconductor NCs have discrete energy levels and their band gap energy is size dependent (assuming simply a two-band semiconductor, which contains of a single parabolic conduction band and a single parabolic valence band.).

NCs) have the same lattice structure as semiconductor bulk materials. The increase of their surface-to-volume ratio and their size-dependent properties are the main differences to bulk materials. The "Quantum-size effect" phenomenon appears when the dimension of the semiconductor NC gets below the bulk semiconductor exciton Bohr radius which results in a blue shift of the exciton energies.

Ekimov and Onushchenk have shown the first experimental evidence for quantum-size effects of excitons in all three dimensions for CuCl and the blue shift of the excitonic absorption spectrum.[31–33] The size, at which the transition from bulk to NCs happens, usually corresponds to a number of approximately 100 to 10000 atoms.[34] In 1984 Louis Brus explained the size dependence of the lowest excited electron state. As the result of the quantum confinement effect,[33, 35] the continuous energy bands of the bulk semiconductors material will be replaced with discrete energy levels in semiconductor NCs with a band gap energy related to the one of the bulk semiconductor by Brus-Formel.

$$E_g(NC) = E_{bulk} + \frac{\pi^2 \hbar^2}{2m_r R^2} - 1.8 \frac{e^2}{\epsilon R} \quad (2.8)$$

Here  $R$  represent the average radius of the NCs. The first term in this equation is the quantum energy of localization of electrons and holes and shifts  $E_g(NC)$  to higher energies by the factor of  $R^{-2}$ . The second term defines the Coulomb interaction induced by the correlation between electron and hole positions, which shifts  $E_g(NC)$  to lower energies as  $R^{-1}$ . [33, 36] The reduced exciton mass  $m_r$  is defined as [32, 34]

$$\frac{1}{m_r} = \frac{1}{m_e^*} + \frac{1}{m_h^*}. \quad (2.9)$$

Transient absorption spectroscopy, which will be explained later, is a method that has direct access to the carrier population in the band structure of the NCs.

## 2.2 Synthesis

In 1950 Victor LaMer and Robert Dinegar developed a method of synthesizing monodisperse colloids. [37] They further explained the colloidal synthesis in three phases, where in the first phase the concentration of the system (in their case sulfur) grows until it reaches a critical concentration ( $C_{min}$ ), where the system enters a second phase, the nucleation phase, until it reaches a supersaturating point at which the nucleation phase rate becomes zero. The nucleation phase can be controlled by controlling the initial concentration of the components (in their case acid and thiosulfate). The shorter the nucleation phase, the more monodisperse colloids will result. After the concentration reaches its maximum, the nucleation rate starts to decrease. The system enters a third phase the so-called growth phase, where discrete particles start to grow. In this phase the growth rate can be controlled by the rate of the chemical reaction (Figure 2.3). In a high monomer concentration small crystals will grow faster than large crystals, which is known as Ostwald ripening. At a critical size (given at any monomer concentration) NCs can not grow further. If the monomer concentration is high enough, the critical size is small and all particles can grow. The smaller particles grow then faster, so that the size distribution can be kept down to a nearly monodisperse distribution. Large crystals with smaller surface-to-volume ratio have a higher stability and are energetically convenient for growing further. If the monomer concentration is below a critical threshold, small particles are dissolved on the surface of the large particles, which lead to the further growth of the large particles. [39]

The growth can be performed in several ways, one is the hot injection method. [40] The first step for synthesis is to find a temperature for the growth. The method then contains two main steps: one to make the nucleation process very fast, in a way that the precursors are injected very fast in a hot solvent (250-350°C) to form a supersaturation of monomers, which is followed by the fast nucleation of NCs, and the other is to separate the nucleation phase from the growth phase of the NCs by decreasing the temperature. If these two

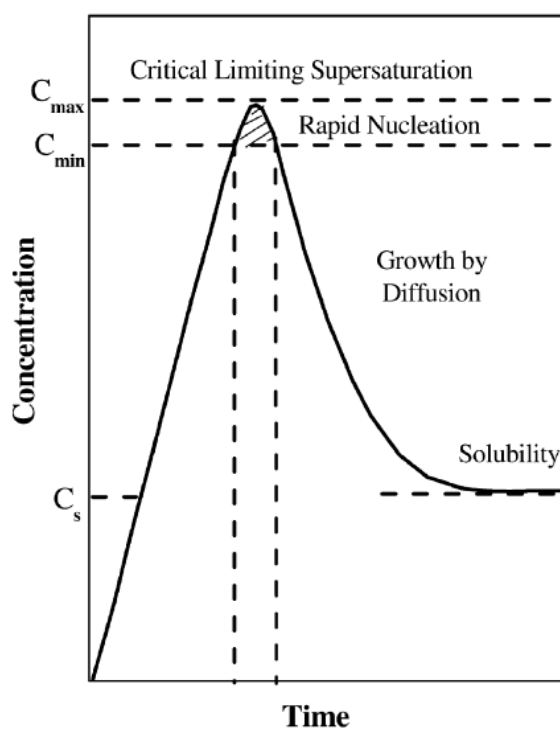


**Figure 2.3:** An illustration of LaMer's condition of the concentration of the system before and after nucleation as a function of time.

(Reprinted (adapted) with permission from Growth of nanocrystals in solution, Ranjani Viswanatha and Dipankar Das Sarma. Copyright (2007) Nanomaterials chemistry.)[38]

process take place separately, the size distribution can be narrow and the control over the size-distribution can be precise.

In the next Chapter the structural properties of exemplary InP QDs are introduced. The InP QDs are formed by mixing indium(III) chloride, zinc(II) chloride and technical oleylamine (OLA) under a temperature of 180 °C. A quick injection of tris(dimethylamino) to this mixture leads to the formation of InP QDs.[41]

### 2.2.1 Core/Shell Nanocrystals

A general way to avoid potential surface trapping and to increase the PLQY of the NCs is to embed the NCs in another semiconductor material and to generate so-called core/shell NCs. This approach isolates the photo-excited carrier from the other surface. The core/shell combination can be also applied for different shape of NCs. Core/shell QDs/QRs are applied as fluorescence reporters and also in bioanalysis.[42, 43] The high molar extinction coefficients and PLQY of core/shell QDs/QRs often exceed those of QDs.[44, 45] If the shells have a larger band gap than the core NCs, the electron and hole carrier will be confined in the core (so-called type I core/shell NCs) and the overlap with the trap states will be reduced.[46–48]

The synthesis of core/shell NCs can be conducted by the SILAR-method (*successive ion layer adhesion and reaction*). The growth of the shell is performed by growing monolayer by monolayer by alternating injection of cationic and anionic precursors into the reaction mixture of the core NCs.[49, 50] After the synthesis of the core NCs, they can be purified and the shell precursor is slowly added to the solution in a lower temperature than for the fabrication of the cores to avoid the direct nucleation of the shell.

Another approach is to prepare them in a so called one pot synthesis, where the shell precursors will be added with a syringe pump slowly to the core solution. There the purification process of the core is not necessary. The thickness of the shell can be controlled via the amount of shell precursor added to the solution.

In order to prepare an alloyed shell, instead of adding a single shell precursor, the two alloy component precursors will be inject to the solution.

In this work, different type I core/shell NCs are investigated such as CdSe/ZnS, CdSe/CdS, InP/ZnS and InP/ZnSe.

In the following, the syntheses of core/shell NCs used in this work are presented. InP/ZnSe core/shell QDs were synthesized after reducing the temperature of the InP core mixture (introduced before) by stoichiometric injection of TOP-Se and Zn(stearate)<sub>2</sub>, octadecene (ODE) and OLA. After increasing the temperature, TOP-Se was injected drop-by-drop.

InP/ZnSe QDs were precipitated once in ethanol and suspended in toluene.

CdSe/CdS core/shell QDs/QRs were synthesized from CdSe QD seeds in a high boiling organic solvents such as trioctylphosphine (TOP), trioctylphosphine oxide (TOPO), hexylphosphonic acid (HPA), and octadecylphosphonic acid (ODPA).[43, 51]

The lattice constant of the shell usually is different than the one of the core QDs. At the interface of these two, the lattice constant of the shell will adjust to the one of the core (Figure 2.4). This lattice mismatch between the two materials can cause a tensile or

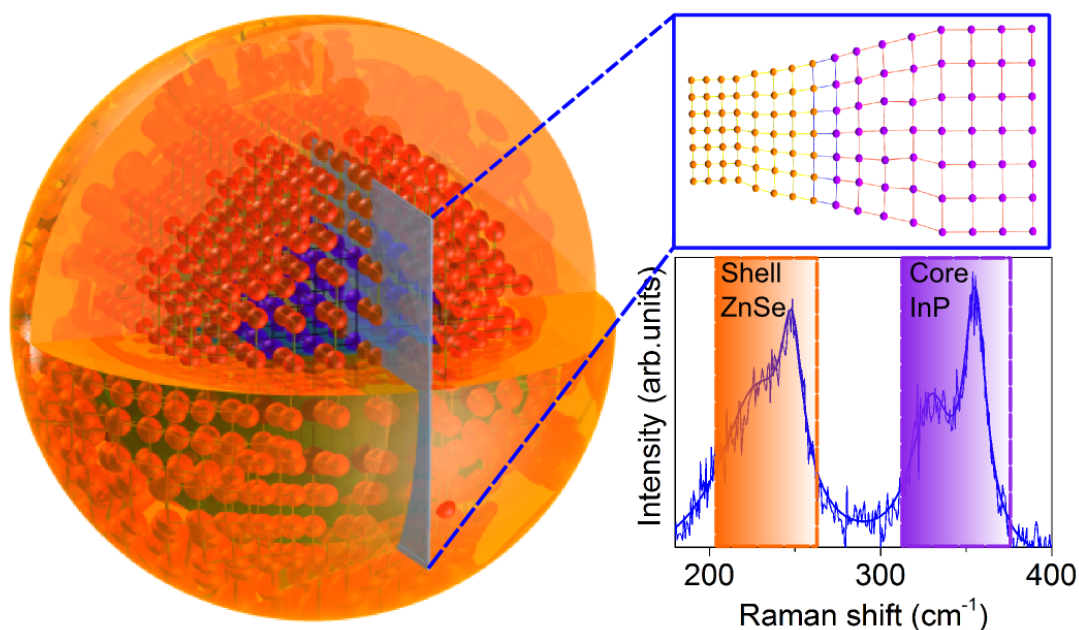


**Figure 2.4:** Schematic illustration of InP/ZnSe core/shell QDs. The lattice constant of the shell is smaller than the core lattice constant, which leads to a lattice mismatch at the interface of core and shell.

(Reprinted (adapted) with permission from Strain Engineering in InP/(Zn,Cd)Se Core/Shell Quantum Dots, Mona Rafipoor, Dorian Dupont, Hans Tornatzky, Mickael D. Tessier, Janina Maultzsch, Zeger Hens and Holger Lange. Copyright (2018) American Chemical Society.)

compressive strain in the core (Figure 2.5). If the strain reaches a critical values,[52] it can also generate defects at the surface and changes the electronic structure, which lead to a trapping of the photo excited carrier and a reduction of the PLQY.[53, 54]

### 2.2.2 Core/Shell QDs Alloy

Tuning the lattice constant of the core/shell QDs continuously can be applied by gradual alloying. Changing the shell composition can be accomplished by using solid solutions for either the core or the shell component.[55–60] At a constant temperature, the crystal lattice constant of an alloy builds a linear relationship with the concentration of the constituent of the alloy elements. This empirical rule known as "Vegard's law", was observed by Vegard

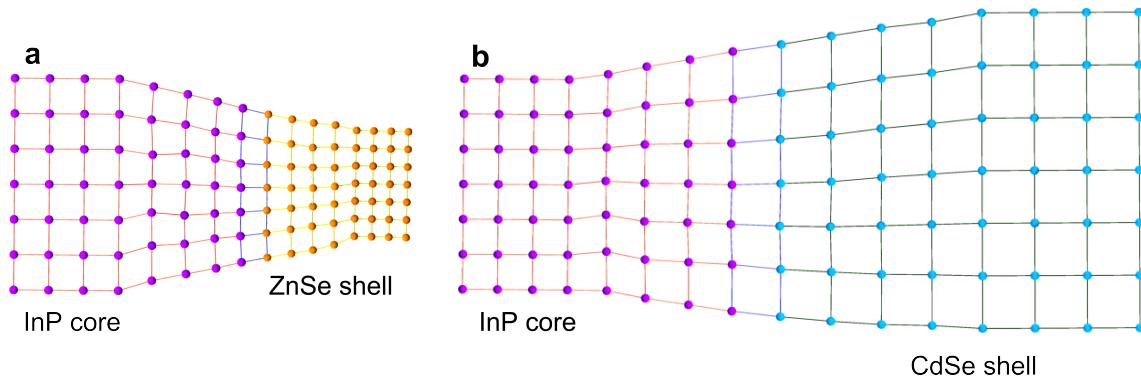


**Figure 2.5:** The lattice reconstruction at the interface leads to strain in both compounds. The crystal with the smaller lattice constant is subject to tensile strain, while the crystal with the larger lattice constant is compressed.

(Reprinted (adapted) with permission from Strain Engineering in InP/(Zn,Cd)Se Core/Shell Quantum Dots, Mona Rafipour, Dorian Dupont, Hans Tornatzky, Mickael D. Tessier, Janina Maultzsch, Zeger Hens and Holger Lange. Copyright (2018) American Chemical Society.)

in 1921.[61, 62] In recent works, Bouamama *et al* showed a weak deviation of Vegard's law for the obtained lattice parameter values of  $\text{Zn}_x\text{Cd}_{1-x}\text{Se}$  against the zinc fraction  $x$ . [63] In Figure 2.6 the calculated lattice parameter shows a quadratic relation with the zinc fraction  $x$ .

$$a_0 = (1 - x)a_0^{\text{CdSe}} + xa_0^{\text{ZnSe}} + bx(1 - x) \quad (2.10)$$

Here  $a_0$  stands for the equilibrium lattice parameter.  $b = 0.0777$  is a bowing parameter. The experimental data for these alloys were investigated by Bouroushian *et al* and agree with the calculated data.[64]

In Figure 2.7 transmission electron microscopy (TEM) images of different compositions of InP/(Zn,Cd)Se are shown. Changing the composition of the shell alloy leads also to a change in the structure of the core/shell QDs. The bulk lattice constants of the components is the main guideline for this optimization through strain engineering. In the next Chapter an experimental realization of strain engineering of these alloys (InP/(Zn,Cd)Se) is demonstrated.[41]

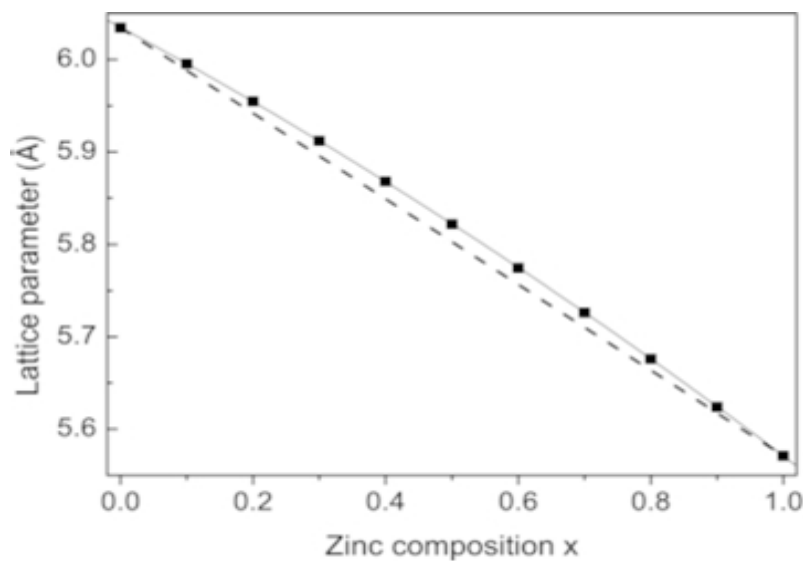


**Figure 2.6:** Relaxed lattice parameter of  $\text{Zn}_x\text{Cd}_{1-x}\text{Se}$  as a function of composition ( $x$ ) fitted with a quadratic relation. The dashed line represent Vegard's law.

(Reprinted (adapted) with permission from Ab initio calculation of the elastic properties and the lattice dynamics of the  $\text{Zn}_x\text{Cd}_{1-x}\text{Se}$  alloy, Khaled Bouamama, P. Djemia, N. Lebga, K. Kassali. Copyright (2009) Semiconductor Science and Technology.)

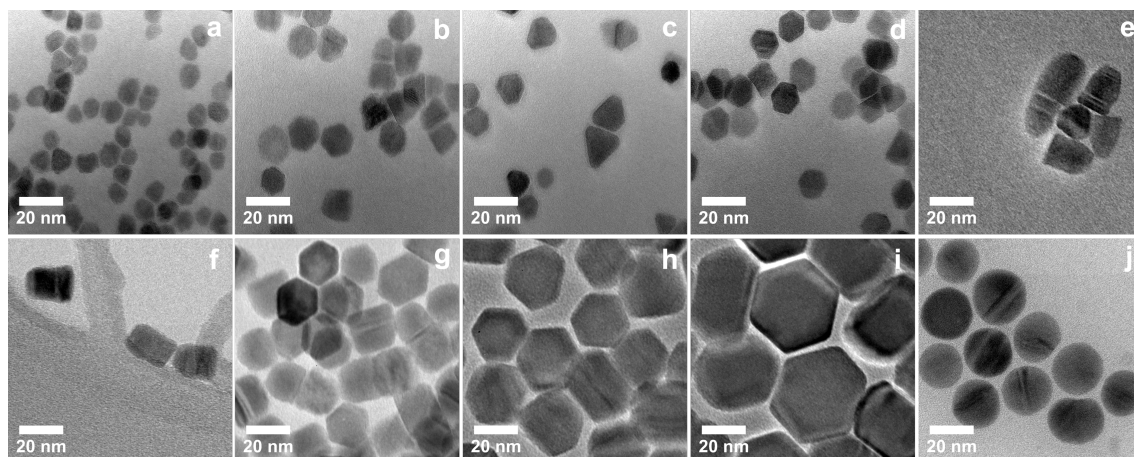


**Figure 2.7:** TEM images of a) InP/ZnSe QDs, b) InP/ $\text{Zn}_{0.975}\text{Cd}_{0.025}\text{Se}$  QDs, c) InP/ $\text{Zn}_{0.95}\text{Cd}_{0.05}\text{Se}$  QDs, d) InP/ $\text{Zn}_{0.87}\text{Cd}_{0.13}\text{Se}$  QDs, e) InP/ $\text{Zn}_{0.79}\text{Cd}_{0.21}\text{Se}$  QDs, f) InP/ $\text{Zn}_{0.58}\text{Cd}_{0.42}\text{Se}$  QDs, g) InP/ $\text{Zn}_{0.30}\text{Cd}_{0.70}\text{Se}$  QDs, h) InP/ $\text{Zn}_{0.13}\text{Cd}_{0.87}\text{Se}$  QDs, i) InP/ $\text{Zn}_{0.02}\text{Cd}_{0.98}\text{Se}$  QDs, j) InP/CdSe QDs.

(Reprinted (adapted) with permission from Strain Engineering in InP/(Zn,Cd)Se Core/Shell Quantum Dots, Mona Rafipoor, Dorian Dupont, Hans Tornatzky, Mickael D. Tessier, Janina Maultzsch, Zeger Hens and Holger Lange. Copyright (2018) American Chemical Society.)

### 2.2.3 Micelles

To make NCs applicable for biological use they have to be water-soluble. As mentioned earlier, one option is to use biocompatible polymers. One kind of polymer can be bound to the NCs via a ligand exchange. Such polymers can be water-soluble. Another kind of polymers are block-copolymers, which can self-assemble into water-soluble micelles and encapsulate hydrophobic NCs. In this case, the hydrophobic block isolates the core of the NCs from the solvent, while the hydrophilic blocks provides the stabilization and forms the corona.[65–67] The polymer container can contain multiple and different NCs in it.[22, 23, 68–70] The morphology of the micelles can be controlled.[71–74] Figure 2.8 illustrates the approach of ligand exchange and the encapsulation. The QDs/QRs are synthesized with Octadecylphosphonic acid (ODPA) and hexylphosphonic acid (HPA) as passivating ligands. The ODPA and HPA are then exchanged with larger hydrophobic polymer ligands of different weights. Amphiphilic diblock-copolymers are then added to the polymer-stabilized QDs/QRs and the mixture is transferred into aqueous solution. The copolymers weight plays the main role for controlling the micelle size. The amount of QDs/QRs encapsulated in the micelles can be controlled by the relative concentration of the used copolymer to the NCs. A high amount of polymer concentration can lead to the saturation of the hydrophobic surface of the NCs. By adjusting the ratio of the amphiphilic polymer to the QDs/QRs the encapsulation of multiple and single NCs can be achieved.[43]

In Chapter 5 the inter-particle distance in the micelles becomes a main issue. This can be changed by varying the size of the exchanged polymer ligand. For this aim 4 different clusters of encapsulated QDs/QRs are introduced in Table 8.2. The native ligands are exchanged with three different weighted polymer ligands are used, a 2,2'-diaminodiethylamine functionalized polyisoprene [PI-DETA] ( $M_n \sim 1.1$  kDa) and two phosphonic acid functionalized polybutadiene [PB-PA] ( $M_n \sim 2.2$  and 4.8 kDa). Amphiphilic diblock copolymers polyisoprene-*block*-poly(ethylene oxide) (PI-*b*-PEO) and polybutadiene-*block*-poly(ethylene oxide) (PB-*b*-PEO) are added to the polymer-stabilized QDs/QRs and the mixture is transferred into aqueous solution (Figure reffgr:fig26). In the last step, the copolymer is cross-linked by radical initiated polymerization to finalize the construct.

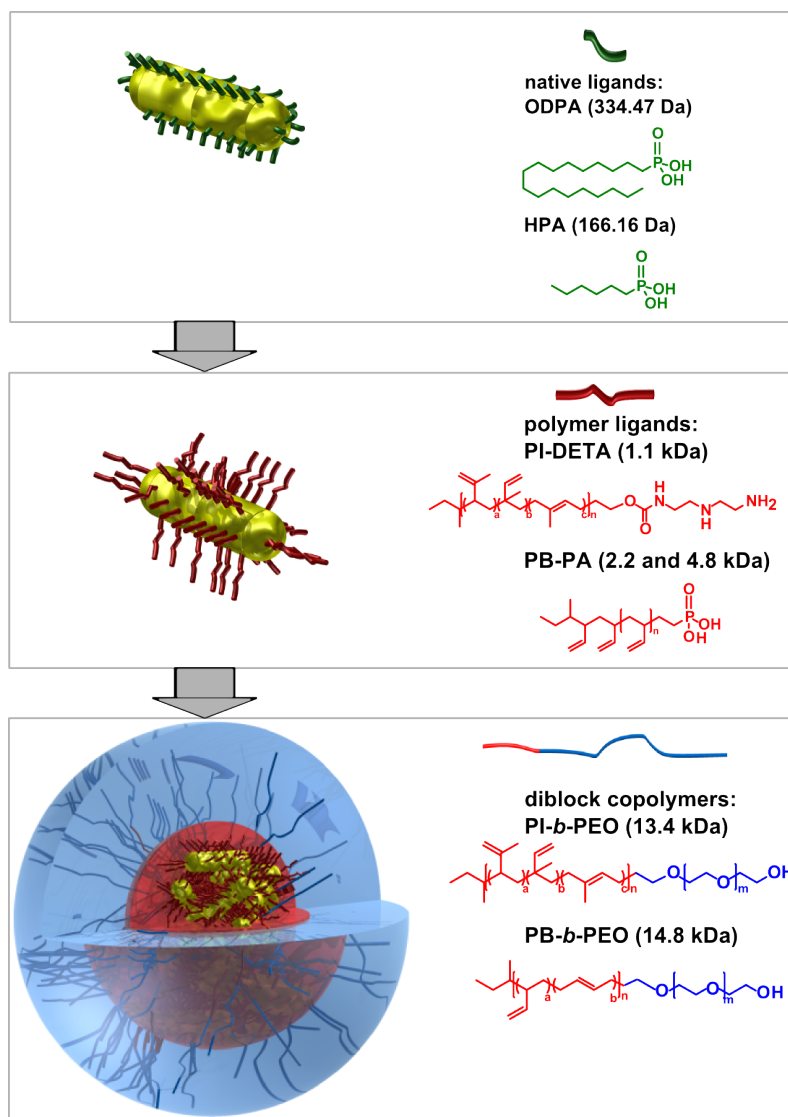


**Figure 2.8:** Schematic illustration of the QD/QR micellar encapsulation. The QD/QR ligand defines the interparticle distance within the micelle. An exchange of the short native ligands to a polymer ensures a larger interparticle distance. The micelles are formed by amphiphilic diblock copolymers, where the hydrophobic QDs/QRs assemble within the hydrophobic core of the micelle and the hydrophilic part of the copolymer stabilizes the construct in the aqueous solution.

**Table 2.1:** The used ligands and copolymers for cluster1-4 in Chapter 5. Increasing the ligand size leads to an increase of the interparticle distance. The copolymers weight plays the main role for controlling the micelle size. The amount of QDs/QRs encapsulated in the micelles can be controlled by the relative concentration of the used copolymer to the NCs. The inter-particle distance in the micelles can be changed by varying the size of the exchanged polymer ligand.

sample	Ligand	$M_{\text{ligand}}$	Dcopolymer	$M_{\text{copolymer}}$	excess
cluster1	PB-Phosphonat	5000 Da	PB- <i>b</i> -PEO	15000 Da	200-fold
cluster2	PB-Phosphonat	2100 Da	PB- <i>b</i> -PEO	15000 Da	200-fold
cluster3	PI-DETA	1300 Da	PI- <i>b</i> -PEO	13700 Da	500-fold
cluster4	ODPA/HPA	334/166 Da	PI- <i>b</i> -PEO	13700 Da	500-fold

In Chapter 4 the optical properties of three different clusters of encapsulated QDs/QRs are investigated. Figure 2.9 e-f shows the QDs/QRs with native ligands. The native ligands are exchanged with the block-copolymers (polyisoprene-*block*-diethylenetriamine [PI-DETA], PI-*b*-PEG), which acts as the seed for micelle formation. Three different weighted PI-*b*-PEG were synthesized. The QDs/QRs with PI-DETA, PI-*b*-PEG diblock polymer and a radical initiator dissolve in tetrahydrofuran and solve in water (Table 2.2).[75]

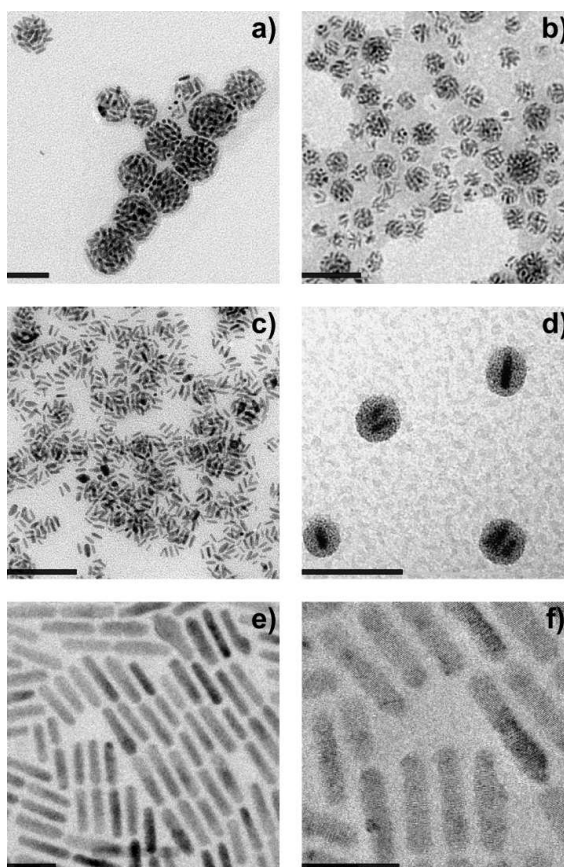


**Figure 2.9:** TEM micrographs of QDQR clusters encapsulated with three different weighted PI-*b*-PEGs: a) 14300 Da (large), b) 8100 Da (medium) and c) 4600 Da (small). The scale bars correspond to 0.1  $\mu\text{m}$ . d) TEM image of single encapsulated QDs/QRs after phase transfer into water. The scale bar corresponds to 50 nm. e) Native QDs/QRs after the synthesis in toluene. f) High resolution TEM image of native QDs/QRs. The scale bars each correspond to 20 nm.

Reprinted (adapted) with permission from Clustering of CdSe/CdS Quantum Dot/Quantum Rods into Micelles Can Form Bright, Non-blinking, Stable, and Biocompatible Probes, Mona Rafipoor, Christian Schmidtke, Christopher Wolter, Christian Strelow, Horst Weller, Holger Lange. Copyright (2015) American Chemical Society.

**Table 2.2:** Hydrodynamic diameter via DLS (volume distribution) of clustered QDs/QRs loaded PI-*b*-PEG diblock-copolymer micelles used in Chapter 4.

PI- <i>b</i> -PEG diblock-copolymer Abbreviation	$M_w$	Diameter by volume of clustered QDs/QRs
small	4600 Da	73 nm
medium	8100 Da	81 nm
large	14300 Da	108 nm

## 2.3 Methods

In this work structural and optical properties of NCs are investigated by applying different spectroscopy methods. In this section the different spectroscopic methods, including Raman spectroscopy, time-resolved photoluminescence spectroscopy (PL) and transient absorption spectroscopy (TA) are introduced.

### 2.3.1 Raman Spectroscopy

Raman spectroscopy is based on inelastic scattering of light by other elementary excitations such as optical phonons.[76, 77] Since the atoms in a crystal are bound to each other, a displacement of the atoms propagates through the crystal as wave. The Hamiltonian for a perfect crystal contains the Hamiltonian of ions in the crystal, the Hamiltonian of the electrons in crystals and the interaction Hamiltonian between them (electron and ions), which is the term responsible for the displacement  $\delta R_j$  of the ions from the equilibrium position  $R_{j0}$ . The simple approximation that is used in textbooks to simplify this equation is to assume that the electron motion in a crystal follows the motion of the ions instantaneously. This is known as the Born-Oppenheimer and adiabatic approximation.[26]

$$H = H_{ions}(R_j) + H_e(r_i, R_{j0}) + H_{e-ion}(r_i, \delta R_j) \quad (2.11)$$

Here the electron Hamiltonian is defined by the kinetic energy of the electron. Assuming that every electron has the same average potential  $V(r)$ , also known as the mean-field approximation. The Schrödinger equation will describe the motion of electrons as:

$$H_e = \frac{P^2}{2m} + V(r). \quad (2.12)$$

The ion Hamiltonian consists of the ion Hamiltonian in equilibrium and the change ion Hamiltonian due to the displacement:

$$H_{ion} = H_{eq} + H_{dis}. \quad (2.13)$$

The Hamiltonian due to the displacement is defined by the harmonic approximation,[26] where the motion of the ions is assumed to follow an harmonic oscillator. Considering the displacement of the  $k$ -th ion from equilibrium in the unit cell  $l$  by  $(u_{kl})$ , within the harmonic approximation, the displacement Hamiltonian term can be written as:

$$H_{dis} = \frac{1}{2}M\left(\frac{du_{kl}}{dt}\right)^2 + \frac{1}{2}\sum_{k'l'} u_{kl}\cdot\Phi(kl, k'l')\cdot u_{k'l'}, \quad (2.14)$$

where  $-\Phi(kl, k'l')$  is the force constant on the ion $_{kl}$  through the displacement of the ion $_{k'l'}$  ( $u_{k'l'}$ ). The quantization of the oscillation energy in the lattice leads to the definition of *phonons* as the quantum of the lattice vibration. Similar to the motion of the electron in the lattice, the displacement of the ion  $kl$  can be described with a Bloch wave. The displacement  $u_{kl}$  is related to the displacement of the ion from origin ( $u_{k0}$ ) and can be specified with the lattice vector ( $R_l$ ):

$$u_{kl}(q, \omega) = u_{k0}e^{i(qR_l - \omega t)}, \quad (2.15)$$

where  $q$  is the wave vector and  $\omega$  is the frequency of the elastic wave that describes the vibration of the lattice through the displacement. One can use this approach to solve the Hamiltonian from equation 2.14. Applying the mass Fourier transformation of the force constant  $\Phi$  leads to a dispersion relation. The dispersion relation can be written in terms of the oscillation frequency  $\omega$ :

$$D_{kk'} - \omega^2\delta_{kk'} = 0 \quad (2.16)$$

The dispersion relation shows the behavior of the frequency versus the wave vector. The dispersion relation can also be obtained from Hooke's law. One can assume the elastic response of the crystal as a function of the force with a linear relation. This is also equivalent to the quadratic relation between elastic energy and the displacement of two points in the crystal. The displacement of one plane of atoms ( $u_s$ ) causes a displacement in the neighboring plane ( $u_{s\pm n}$ ) and is proportional to the displacement difference of them ( $u_{s\pm n} - u_s$ ). Assuming just the first nearest neighbors, the Hooke's law can be written as:

$$F_s = K(u_{s+1} - u_s) + K(u_{s-1} - u_s). \quad (2.17)$$

Here  $K$  stands for the force constant and depends on the direction. In this example  $K$  acts as a scalar.  $F_s$  is defined as the force caused by the displacement on one atom. Solving the equation of motion for an atom leads to the dispersion relation:

$$\begin{aligned} M\frac{d^2}{dt^2}u_s &= K(u_{s+1} - u_s) + K(u_{s-1} - u_s) \\ &= K(u_{s+1} + u_{s-1} - 2u_s), \end{aligned} \quad (2.18)$$

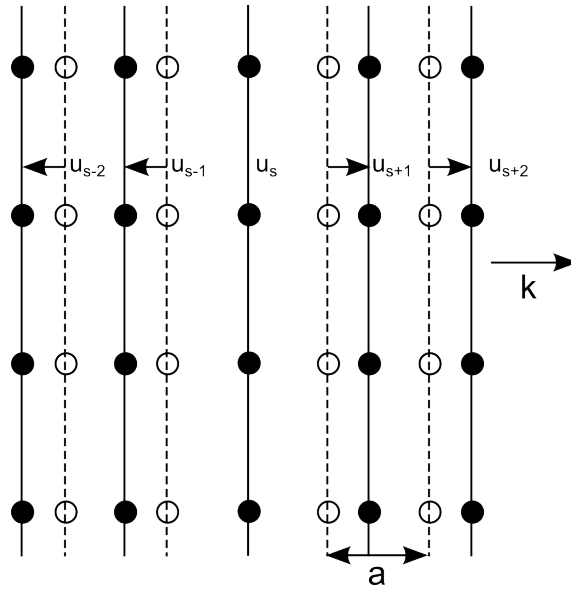


**Figure 2.10:** Planes of atoms in equilibrium (dashed line) and after longitudinal displacement (solid lines).  $a$  is the spacing between different planes and  $K$  stands for the wave vector.

where  $u_s$  is a traveling wave function with  $\frac{d^2}{dt^2}u_s = -\omega^2 u_s$ :

$$u_s = u e^{i(ksa - \omega t)}. \quad (2.19)$$

Substituting equation 2.19 in equation 2.18 leads to:

$$\begin{aligned} -M\omega^2 u \cdot e^{i(ksa - \omega t)} &= K(e^{i(ka)} + e^{-i(ka)} - 2)u \cdot e^{i(ksa - \omega t)} \\ M\omega^2 &= K(2 - e^{i(ka)} - e^{-i(ka)}) \\ &= 4K(\sin^2(ka/2)) \end{aligned}$$

The dispersion relation for one atom in a lattice defines the relation between the oscillation frequency ( $\omega(k)$ ) and the wave vector ( $k$ ) as:

$$\omega(k) = 2\sqrt{\frac{K}{M}} |\sin(ka/2)|. \quad (2.20)$$

Unit cells containing atoms with a smaller mass oscillate with a higher frequency than the ones with larger mass. Depending on the lattice structure the number of atoms in the primitive unit cell and the number of phonons can be different. The phonons are divided in to transverse or longitudinal, depending on the direction of the vibration (perpendicular or parallel to the wave vector  $k$ ). The phonons at the  $\Gamma$  point (zone center phonon mode) can be Raman active and can be resolved by using Raman spectroscopy.[78–81]

This method is used also for determining strain in heteronanocrystals.[82–84] In 1912 and 1918 Eduard Grüneisen described the thermal vibrations of atoms in crystalline solids

as undamped harmonic oscillations. The movement of an atom towards a neighboring atom was calculated by considering the forces attracting or repelling from the atom. He estimated the vibration change by changing the pressure and temperature. A material dependent constant was defined as:[85, 86]

$$\gamma = \frac{\partial \ln \omega}{\partial \ln V} = -\frac{V(\partial V/\partial T)_P}{C_v(\partial V/\partial P)_T}, \quad (2.21)$$

where  $C_v$  is as the energy of a single oscillator.  $\gamma$  is the Grüneisen parameter, which depends on the material.  $\omega$  is the vibration frequency and  $V$  is the crystal volume. The change in the vibration frequency due to strain in a NCs can be estimated by using the Grüneisen parameter of the material. In a spherical NC the relative lattice constant change  $\frac{\Delta a}{a}$  can be obtained from the relative shift of the LO frequency  $\frac{\Delta \omega}{\omega}$ :[87–89]

$$\frac{\Delta \omega}{\omega} = \left(1 + 3\frac{\Delta a}{a}\right)^{-\gamma} - 1. \quad (2.22)$$

In this thesis, different confocal micro-Raman setups in backscattering geometry were used. In order to obtain the core and the shell-related Raman bands, different excitation wavelengths were required.

830 nm, 458 nm (diode lasers), 514 nm (ArKr laser), 532 nm (frequency-doubled Nd:YAG laser) and 633 nm (HeNe laser) was served as excitation sources. For ArKr laser lines a Dilor XY800 triple monochromator setup was used with a liquid N<sub>2</sub> cooled CCD. In all other setups an LabRamHR800 equipped with a peltier-cooled CCD was used.

For the preparation of the samples, dropcasting was used by simply drying the sample solution on silicon in ambient conditions. The measurements were performed quickly to avoid degradation effects. To avoid sample heating or destruction, the laser power on the sample was around a few hundred micro watts on a diffraction limited spot. For calibrating the spectra neon lines were used.

### 2.3.2 Time-resolved Photoluminescence Spectroscopy

Photons with higher energy than the band gap energy can be absorbed in the NCs. The absorption of the photons leads to the creation of excitons. The excitons can radiatively recombine (after thermalization towards thermal equilibrium distribution) and reemit photons at the band gap. This process is photoluminescence (PL).[26, 90–93]

Figure 2.11 shows the steady state absorption and emission of CdSe/CdS QDs/QRs. In this thesis PL spectroscopy is used to investigate encapsulated QDs/QRs in micelles (Chapter 4-5).

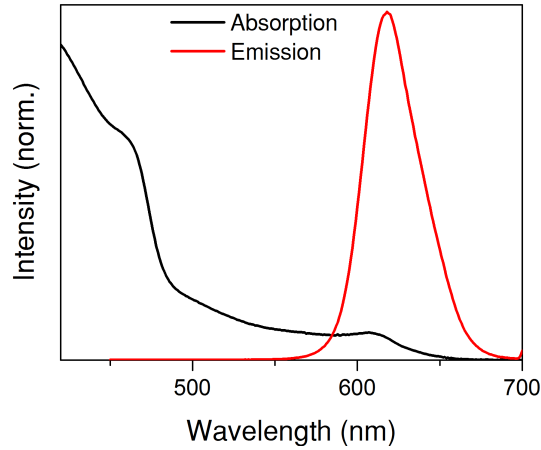


**Figure 2.11:** Steady-state absorption of CdSe/CdS core/shell QDs/QRs. The shell peak appears at 462 nm. The core has a smaller band gap than the shell and appears at 610 nm. The emission of the core in red corresponds to the lower energy transition states (617 nm).

The two main information one can obtain from the PL spectrum are the peak position and the spectral width. The peak position relates to the band gap energy of the QDs/QRs and the width to the recombination mechanisms.[94] The interaction of the exciton with the environment leads to an inhomogeneous broadening of the lifetime-limited "natural" spectrum.[95] The PL spectrum for an ensemble of particles is then a convolution of the emission spectra of the individual particles (Figure 2.12).[96]

Figure 2.13 shows the PL decay curve of the QDs/QRs, which is the PL intensity as a function of time:

$$I(t) = I_0 + \sum_i I_i e^{-t/\tau_i} \quad (2.23)$$

Where  $I_0$  is a measured background intensity and  $i$  corresponds to the order of the recombination mechanism.  $\tau_i$  is expressed as:

$$\frac{1}{\tau_{tot}} = \sum_i \frac{1}{\tau_i} \quad (2.24)$$

The monoexponential PL decay curve indicates a radiative recombination of the excited electron.[97–99] The excited electron needs about 20 ns to recombine radiatively. The radiative recombination rate ( $1/\tau_{rad}$ ) of the excited carrier is defined as  $n / \langle \tau_r \rangle$ , where  $n$  corresponds to the carrier population ( $n = n_e = n_h$ ). As the photogenerated excitons can also nonradiatively recombine, the total decay rate is:

$$\frac{1}{\tau_{tot}} = \frac{1}{\tau_{rad}} + \frac{1}{\tau_{nonrad}}. \quad (2.25)$$

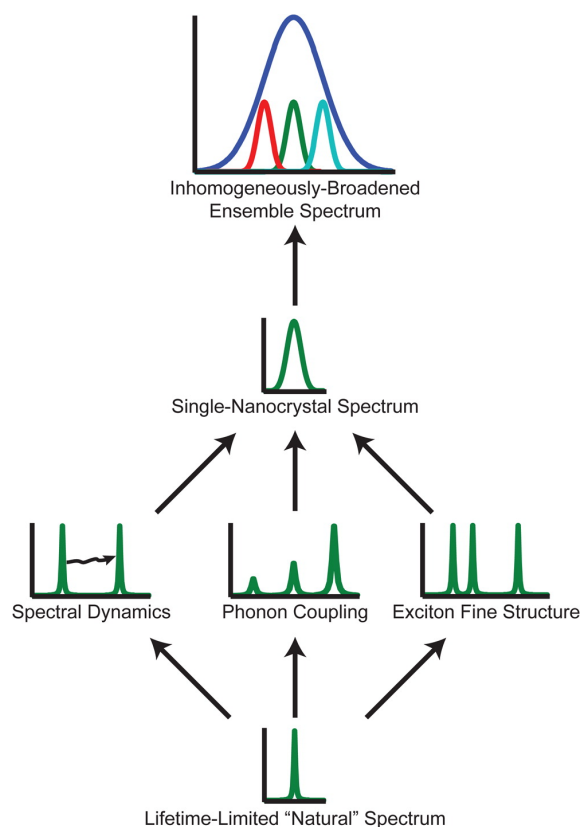


**Figure 2.12:** An ensemble spectrum consists of the intrinsic single-emitter spectrum convolved with the interparticle inhomogeneities. The single-emitter spectrum arises from a combination exciton-phonon coupling of the lifetime-limited 'natural' spectrum, spectral dynamics and emission from fine-structure states.

(Reprinted (adapted) with permission from Evolution of the Single-Nanocrystal Photoluminescence Linewidth with Size and Shell: implications for Exciton-Phonon Coupling and the Optimization of Spectral Linewidths, Jian Cui, Andrew P. Beyler, Igor Coropceanu, Liam Cleary, Thomas R. Avila, Yue Chen, José M. Cordero, S. Leigh Heathcote, Daniel K. Harris, Ou Chen, Jianshu Cao, and Mounqi G. Bawendi. Copyright (2015) American Chemical Society.)

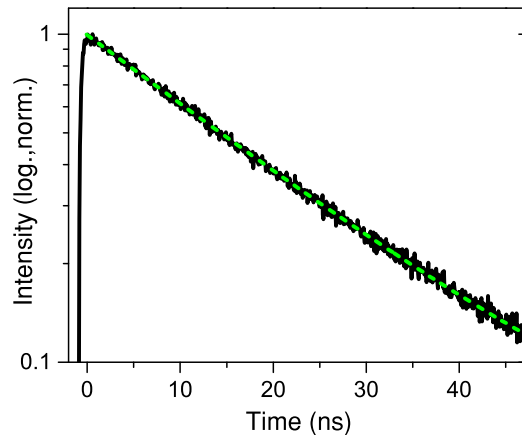


**Figure 2.13:** PL spectroscopy on CdSe/CdS core/shell QDs/QRs. PL decay curve. The lifetime of the excitons at the lower transition state  $1S$  is about 20 ns.

The individual QDs/QRs can show a fluctuation in their PL intensity known as "blinking". The PL intensity of the QDs/QRs switches between two off/on-states. [100–104] The off-state relates to the quenched PL intensity due to the nonradiative recombination.[105, 106] The experimental result for blinking behaviour of CdSe/CdS core/shell QDs encapsulated in micelles are presented in Chapter 4.

In order to perform time-resolved single particles photoluminescence spectroscopy, the sample solutions of the QDs/QRs in micelles were diluted and dropcasted on glass substrates. The glass substrates were first cleaned in a plasma-cleaner. A microscopy setup with a confocal geometry (100x objective lens Zeiss Achroplan, 0.75 NA) was used. A collimated 446 nm laser beam of a pulsed laser diode (PDL800-D, PiL044X, A.L.S. GmbH) was used for the excitation. The laser beam consist of pulse trains with a pulslength of 100 psec and a repetition rate of 10 MHz. To spectrally separate the emitted light (from the sample) from backscattered laser light, a longpass filter with a edge wavelength of 532 nm (Semrock) was pemploeyed. In order to resolve the spectrum of the emitted light a spectrograph (Acton SP2500) combined with a CCD camera (ProEM 512B, Princeton Instruments) was used. For resolving the PL lifetime of the samples, the emitted light was guided to an avalanche photodiode (PDM Series, Micro Photon Devices) with an attached TCSPC (time-correlated single-photon counting) control unit. The blinking (See Chapter 4) time traces were measured by time-tagged time-resolved measurements with PicoHarp 300, PicoQuant GmbH.

The time-resolved PL spectroscopy (streak camera) was performed with the same excitation source as for the TA (next section 2.3.3) and a universal streak camera (C 5680, Hamamatsu photonics) with a M 5675 Synchronscan and Single-Sweep-unit for detection. The estimated

spot diameter within the liquid was  $457\ \mu\text{m}$ .

### 2.3.3 Transient Absorption Spectroscopy

Transient absorption (TA) spectroscopy is a technique that has a direct access to the excited carrier distribution. A femtosecond laser pulse referred to "pump pulse" excites the NCs. The absorption is then monitored by a delayed white light pulse the "probe pulse" (Figure 2.14). [34, 107] This delayed pulse probes the system before and after the excitation by the pump pulse. The change in the absorption is the TA contrast and is measured by this method (Figure 2.15).

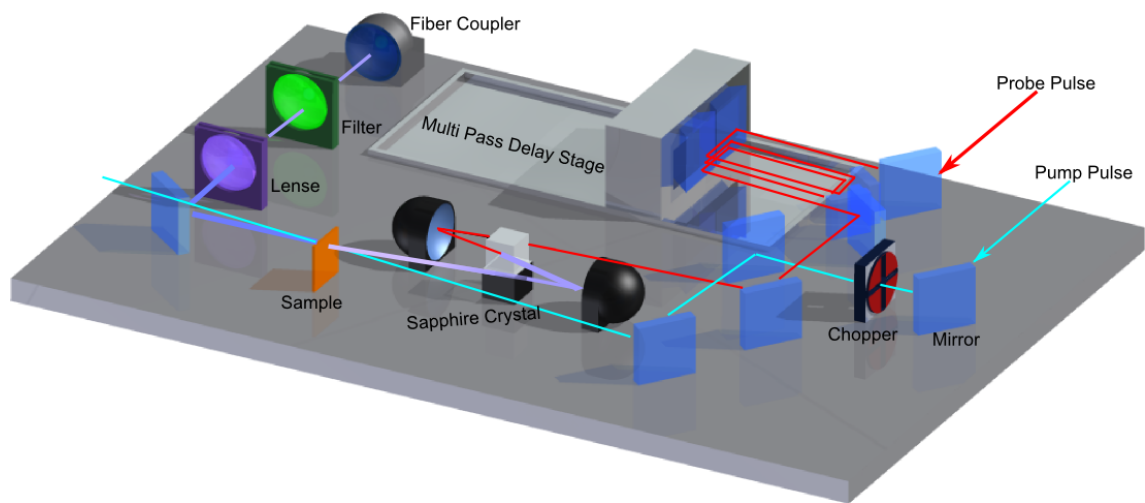


**Figure 2.14:** Schematic illustration of the TA setup. The pump pulse (in blue) excites the sample. The probe pulse (in red) has a temporal delay relative to the pump pulse. With a sapphire crystal it is converted to a white light pulse that hits then the sample. A chopper on the way of the pump pulse blocks every second pulse and leads to the detection of the change in the absorption.

At higher pump fluences the VB is occupied with holes. The incident probe pulse can lead to the excitation of carriers at higher energy bands. This process is known as **photoinduced absorption** and results in a positive bleach in the TA signal.[34, 108, 109] At a low pump fluences ( $\langle N \rangle \ll 1$ ) the probe pulse can either see unexcited NCs or NCs with a single exciton. The created exciton by the pump pulse interacts with the generated exciton by the probe pulse. The interaction between the two excitons (**Biexciton Effect** Figure 8.10) may lead to a transition shift.[110, 111] This transition shift due to the Coulombic interaction of two excitons is called **Stark effect** and can be resolved as a positive bleach in the TA signal with the same dynamic of the excitonic bleach.[112, 113]

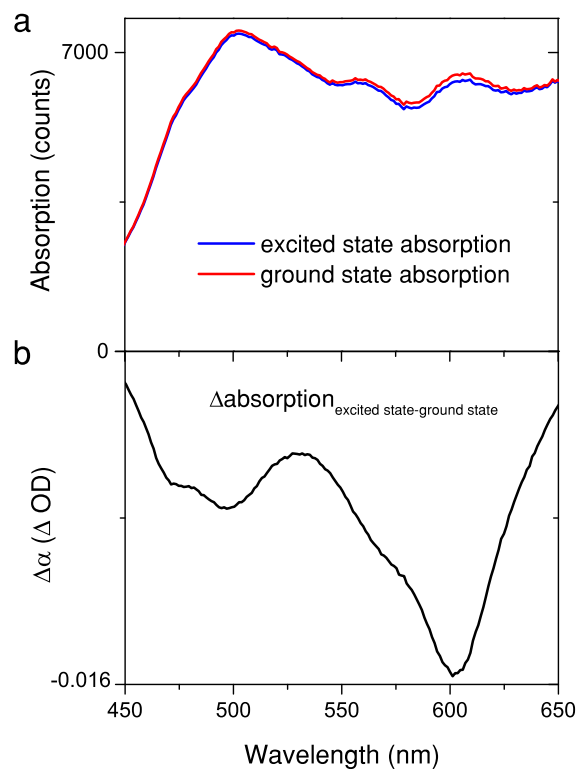
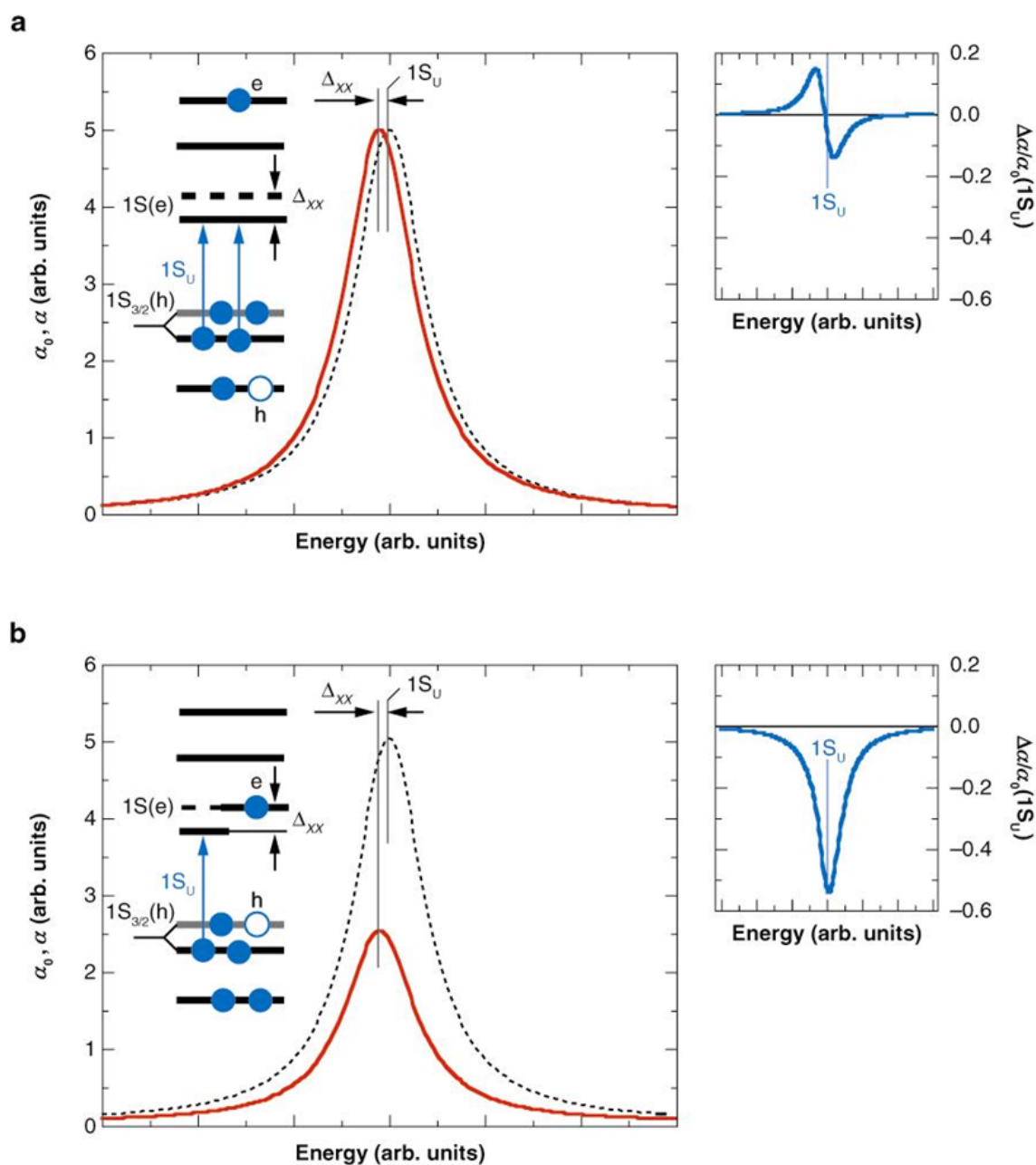


**Figure 2.15:** The origin of the TA spectra of CdSe/CdS QDs/QRs. a) The white light "probe pulse" probes the system before and after the excitation by the pump pulse. b) The change in the absorption ( $\Delta\alpha$ ) is the TA contrast. The excitonic bleach of CdS core is at 600 nm and the excitonic bleach of the CdSe shell is at around 460 nm.

At the early times after the excitation the carriers are at the higher energetic states. The lowest transition state ( $1S$ ) can just be affected by Coulomb interaction. This transition state experiences a shift by  $\Delta_{xx}$  due to the interaction between the exciton at  $1S_U$  and the exciton at higher state (Figure 2.16 a). After thermalization the excitons will reach to the lower transition state ( $1S$ ). Due to the Pauli exclusion principle the states occupied fully by carriers are not able to absorb more photons (Figure 2.16 b). This leads to the bleach and contributes to  $\Delta\alpha$ .

Figure 2.17 a represents a TA map of CdSe/CdS QDs/QRs. The core related absorption bleach is monitored at 550 nm while the shell related absorption bleach is at higher energies (462 nm). The spectra at different times after excitation are in shown in Figure 2.17 b. The incident pump pulse has a photon energy higher than the shell band gap, which leads to more excitons in the larger shell volume.[114] The bleach dynamics of the core and the shell in Figure 2.17 c indicate a faster dynamic for the excitons in the shell. In the earlier time after excitation, the excitons start to thermalize to the  $1S$  excitonic state. When the excitons in the shell started to relax, the  $1S$  excitonic state of the core is still filling up (Figure 2.17 d). The increase in the contrast of the core excitonic bleach indicates a charge transport process from the shell to the core. After 1.5 ps the excitons in the core start to relax.

The Pump-probe TA spectroscopy experiments were performed using a commercial TA setup (Helios; Ultrafast Systems). A commercial amplified Ti-sapphire laser system (Spitfire-Ace, 800 nm, 6 W, 1 kHz, 35 fs; Spectra Physics) was employed to generate pump and probe pulses. The pump pulses were generated in an optical parametric amplifier (TOPAS-Prime; Light Conversion) with frequency mixer (NirUVis; Light Conversion) and chopped at 500 Hz. The probe beam was a broadband continuum white-light with a spectral range of 420-750 nm (Figure 8.8) . The instrument response in this wavelength regime is estimated to be below 200 fs. The excitation wavelength at 418 nm has a spot diameter of 204  $\mu\text{m}$  in solution.



 Klimov VI. 2007.  
Annu. Rev. Phys. Chem. 58:635–73

**Figure 2.16:** Transient of the  $1S_U$  transition shift induced by the biexciton effect is much better pronounced at the early times after the excitation. a) At the early times after the excitation the carriers are at the higher energetic states. The lowest transition state ( $1S$ ) can just be affected by Coulomb interaction. This transition state experiences a shift by  $\Delta_{xx}$  due to the interaction between the exciton at  $1S_U$  and the exciton at higher state. b) Due to the Pauli blocking the states occupied fully by carriers are not able to absorb more photons. The corresponding ground and excited state absorption are shown in black dashed and red solid lines. The side graph on the right corresponds to the resulting  $\Delta\alpha$  spectrum.

(Reprinted (adapted) with permission from Spectral and Dynamical Properties of Multiexcitons in Semiconductor Nanocrystals, Victor I. Klimov. Copyright (2007) Annual Review of Physical Chemistry.)

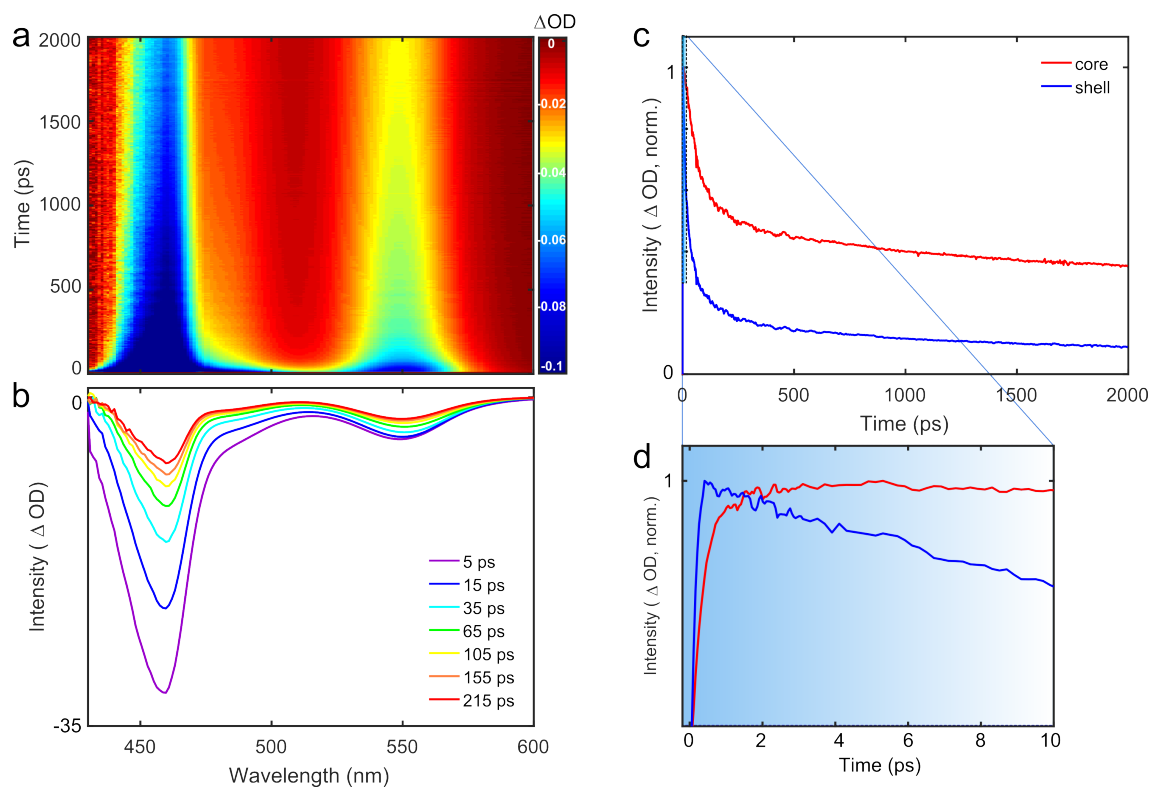


**Figure 2.17:** Transient absorption measurements of CdSe/CdS QDs/QRs. a) Typical TA map, consisting of two main bleaches of core and shell. b) TA spectra at different times after excitation. The TA spectra consist of the absorption bleach of CdSe core at 550 nm and CdS shell at 464 nm. c) TA dynamics of core and shell bleach. d) Zoom in to the first 10 ps of the TA dynamics.



## 3 Structural properties of Core/Shell Quantum Dots

In Chapter 2 three different material combination (core/shell QDs, core/shell QDs alloy and core/shell QDs/QRs encapsulated in micelles) were introduced. Furthermore Raman spectroscopy was introduced as a method for strain analysis. This Chapter includes the experimental Raman results of InP QDs, InP/ZnSe, InP/ZnS core/shell QDs and InP/CdZnSe alloys. The shift of the longitudinal optical (LO) phonons due to change of the material composition is studied in this Chapter.

### 3.1 Optical Phonons of Core/Shell QDs

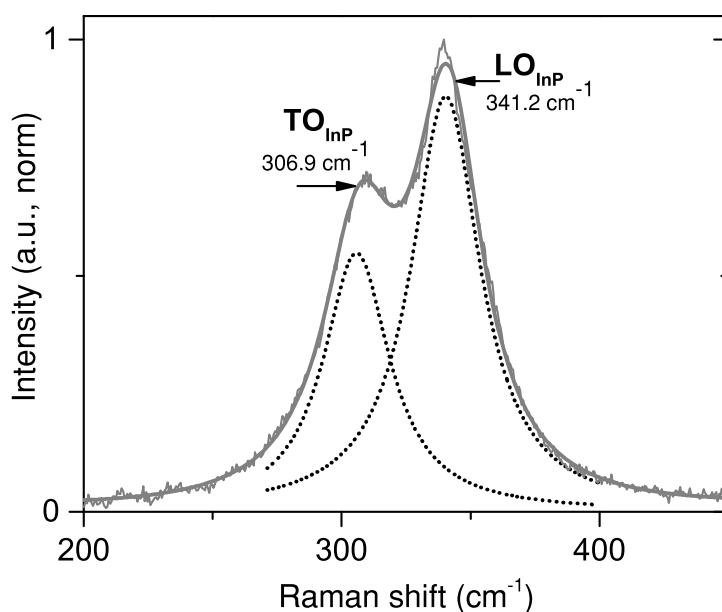


**Figure 3.1:** Representative Raman spectrum of InP QDs with an effective diameter of 3.2 nm.

(Reprinted (adapted) with permission from Strain Engineering in InP/(Zn,Cd)Se Core/Shell Quantum Dots, Mona Rafipoor, Dorian Dupont, Hans Tornatzky, Mickael D. Tessier, Janina Maultzsch, Zeger Hens and Holger Lange. Copyright (2018) American Chemical Society.)

Figure 3.1 represents a Raman spectrum of InP QDs (effective diameter of 3.2 nm), which

consists of two subbands. The bulk LO phonon of InP appears at  $342\text{ cm}^{-1}$  [78], according to other studies.[78, 115–118] The the sub-band at  $306.9\text{ cm}^{-1}$  is assigned to transverse optical (TO) phonons of InP QDs. These Raman bands can be fitted easily with a corresponding Lorentzian function shown as dashed lines in Figure 3.1. In Figure 3.2 the

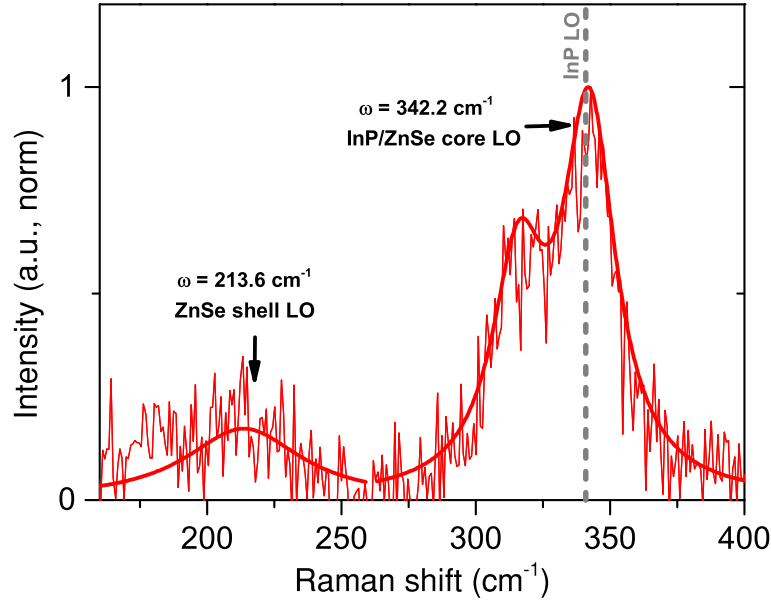


**Figure 3.2:** Raman spectrum of InP/ZnSe core/shell QDs with an effective diameter of 4 nm.

Raman spectra of InP/ZnSe core/shell QDs are illustrated. The LO phonon of the InP core is shifted to higher energies (from  $341.2\text{ cm}^{-1}$  to  $342.2\text{ cm}^{-1}$ ). In contrast to the Raman spectra of plain InP QDs (Figure 3.1), a second band is observed at  $213.6\text{ cm}^{-1}$ . With increasing ZnSe shell thickness, this band shifts to higher energies (Figure 3.3 a and c). For reproducing the shape of this band, two Lorentzians are required. Since the bulk LO phonon of ZnSe is reported to be around  $249\text{ cm}^{-1}$  [117], this band is assigned to the ZnSe shell LO phonon.

### 3.2 Strain in Core/Shell QDs

Increasing the shell thickness of ZnSe influences the core LO phonon frequency, which is interpreted in terms of changed bond lengths and originates from strain between the core and the shell. This issue was introduced earlier in Chapter 2.2.1. A series of InP/ZnSe core/shell Raman spectra are illustrated in Figure 3.3 a. This series includes samples with increasing sizes of ZnSe shells. With increasing the shell thickness, the InP core LO phonon shifts to higher frequencies (Figure 3.3 b). Since the lattice constant of InP ( $5.86\text{ \AA}$ ) is

larger than the lattice constant of ZnSe (5.68 Å), the lattice reconstruction at the interface leads to a shortening of the InP bonds (a compressive strain in the InP core QDs). The opposite effect happens for the ZnSe shell QDs in the core/shell interface in form of a tensile strain. Figure 3.3 d shows the calculated strain in the InP core (in red) evaluated from

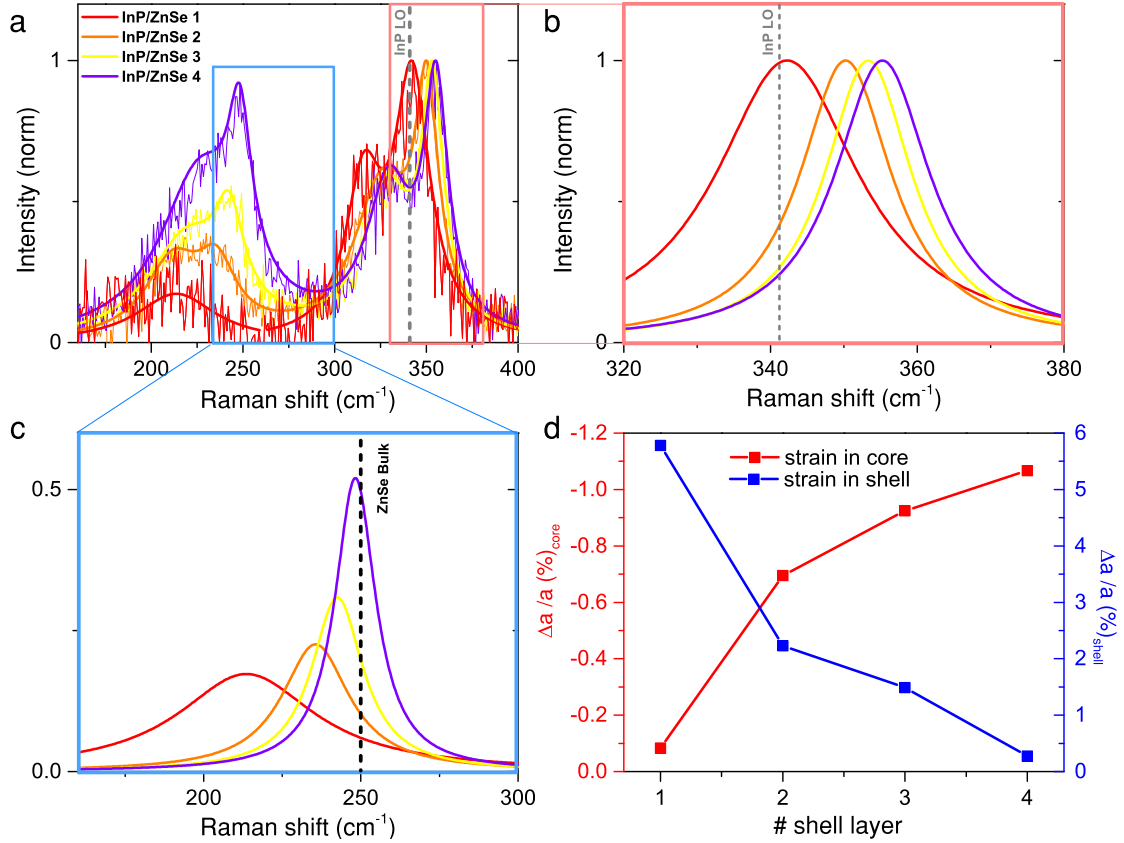


**Figure 3.3:** Increasing the shell size in InP/ZnSe QDs leads to a) a shift of the core related LO band in the direction of lower frequencies. b) Best Lorentzian fit of the core related LO band. c) Shell related LO band with increasing the shell size. d) Calculated strain in the shell and the core of InP/ZnSe QDs.

equation 2.22 with  $\gamma_{\text{InP}} = 1.24$  [119] and the related frequency shift relative to the bare InP QDs LO phonon in Figure 3.1 ( $341.2 \text{ cm}^{-1}$ ). The strain in the ZnSe shell (Figure 3.3 d in blue) was also estimated with equation 2.22 using  $\gamma_{\text{ZnSe}} = 0.85$  [119] instead. In the case of the shell, the frequency change was recorded relative to the bulk value of the ZnSe LO phonon frequency ( $250 \text{ cm}^{-1}$ ). [117]

Figure 3.3 d shows that the core builds up a compressive strain while the strain in the shell is relaxed with increasing the shell size. As mentioned in section 2.2.2, an approach to inhibit the disadvantage of strain in core/shell QDs is the lattice constant tuning by

using alloys of QDs as shell.[60]

The main guideline in this approach are the bulk lattice constants. Because CdSe has a larger lattice constant (6.08 Å) than InP (5.86 Å), the strain would have a inverse behavior to the InP cores than ZnSe shells (5.68 Å). Changing the shell composition by using InP/(Zn,Cd)Se core/shell QDs could change the strain in the InP core from compressive to tensile along changing the shell composition from ZnSe towards CdSe. In this way the lattice mismatch at the core/shell interface could be controlled.[41]

To obtain InP/(Zn,Cd) QDs, Dupont *et al* performed the partial substitution of cadmium acetate for zinc stearate in the shell reaction (Chapter 2.2.2).[120] Changing the shell composition from ZnSe to CdSe, leads to a variation of the shell thickness and a change in the structure from zinc blende (zb) to wurtzite. The growth of the shell in the structure transition regime can be followed by TEM analysis (See Chapter 2.2.2).

Figure 3.4 shows the Raman spectra of InP/ZnSe and InP/CdSe QDs, the two pure benchmark systems of this changing shell composition protocol. Note that the InP/ZnSe shown here is the InP/ZnSe discussed earlier in Figure 3.2. In the case of InP/CdSe QDs, the InP

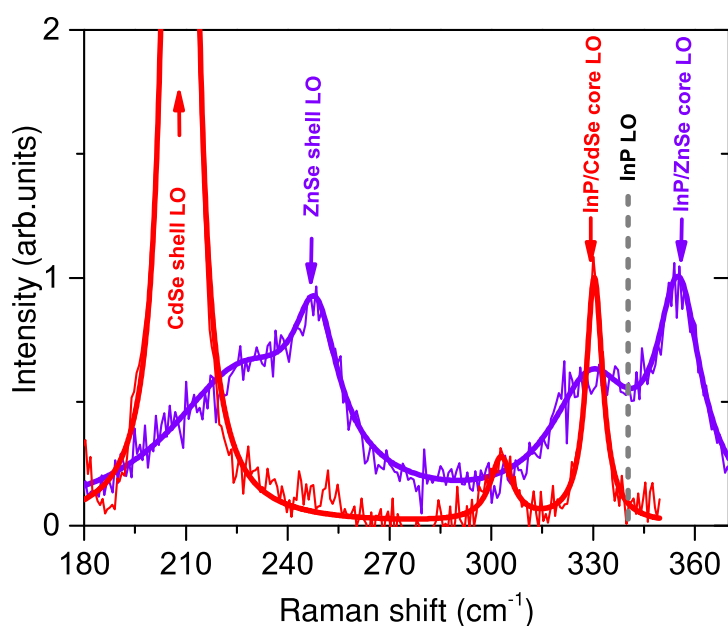


**Figure 3.4:** Raman spectrum of InP/ZnSe and InP/CdSe core/shell QDs showing two Raman modes assigned to the shell (CdSe and ZnSe) and core InP as indicated. The dashed line represents the Raman shift of the LO phonon of plain InP QDs.

(Reprinted (adapted) with permission from Strain Engineering in InP/(Zn,Cd)Se Core/Shell Quantum Dots, Mona Raftpoor, Dorian Dupont, Hans Tornatzky, Mickael D. Tessier, Janina Maultzsch, Zeger Hens and Holger Lange. Copyright (2018) American Chemical Society.)

Raman band is shifted to lower frequencies, opposite to the InP/ZnSe QDs. A new Raman band shows up at the lower energies around  $208.5\text{ cm}^{-1}$ , with a side band at  $206\text{ cm}^{-1}$ ,

which are assigned to the LO phonon and surface optical (SO) phonon of CdSe.[84, 121] Similar to these two benchmarks, the InP/(Zn,Se) core/shell QDs contain two features in their Raman spectra, one correlates to the InP core and the other represents the shell LO phonon. Figure 3.5 zooms into these two regions for two exemplary InP/(Zn,Se) core/shell QDs with either a zinc-rich or cadmium-rich shell composition. Adding a small amount of

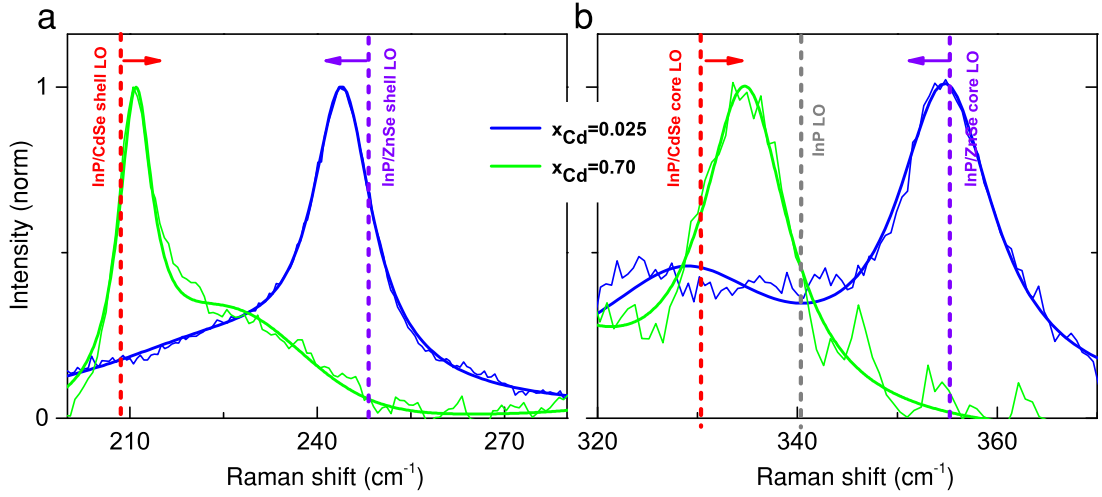


**Figure 3.5:** Exemplary Raman spectra of InP/(Zn,Cd) core/shell QDs with  $x_{\text{Cd}} = 0.025$  in blue and  $x_{\text{Cd}} = 0.70$  in green. Thin lines represent the experimental data, bold lines are best fits of the sum of Lorentzians. a) Shows the frequency region of the shell-related bands and b) the core-related bands. In both a) and b) the spectra have been normalized to the respective LO band intensities. LO frequencies from Figures 3.1 and 3.2 have been included as a reference in dashed lines.

(Reprinted (adapted) with permission from Strain Engineering in InP/(Zn,Cd)Se Core/Shell Quantum Dots, Mona Rafipoor, Dorian Dupont, Hans Tornatzky, Mickael D. Tessier, Janina Maultzsch, Zeger Hens and Holger Lange. Copyright (2018) American Chemical Society.)

Cd to the shell results a shift of the core and shell related LO phonons in contrast to the pure InP/ZnSe. While adding a small amount of Zn to InP/CdSe QDs shifts the core and shell LO phonons in the direction of higher frequencies relative to InP/CdSe benchmark. These opposite shifts are pronounced to be continuous with the shell composition change from ZnSe to CdSe.

In the following the Raman shift of the shell related LO phonon will be discussed.

In general, optical phonons in mixed-ternary alloys exhibit a two or one mode behavior. In a  $A_xB_{1-x}C$  system with a zinc-blende structure, the binary crystals AC and BC have each two Raman frequencies TO and LO. In the one mode phonon behavior one of the LO or TO is dominant energetically and shifts with the composition change from one side ( $x = 1$ ) to the other side ( $x = 0$ ), while the other LO-TO pair vanishes. In other words the frequency position of the LO/TO phonon varies with the composition  $x$ . In the two mode behavior case on the other hand the two LO and TO phonons are energetically well separated, and

their intensity ratio ( $I(AC)/I(BC)$ ) depends on the composition change  $x$ . [122, 123]

According to previous studies, Raman spectra of (Zn,Cd)Se alloys exhibit a one mode behavior. [124] By replacing Zn with Cd, the effective mass of the ions contributing to LO vibration increases. This leads to a reduction of the shell-related LO frequency (equation 2.20). The gradual shift of the Raman bands in a (Zn,Cd)Se has already been reported

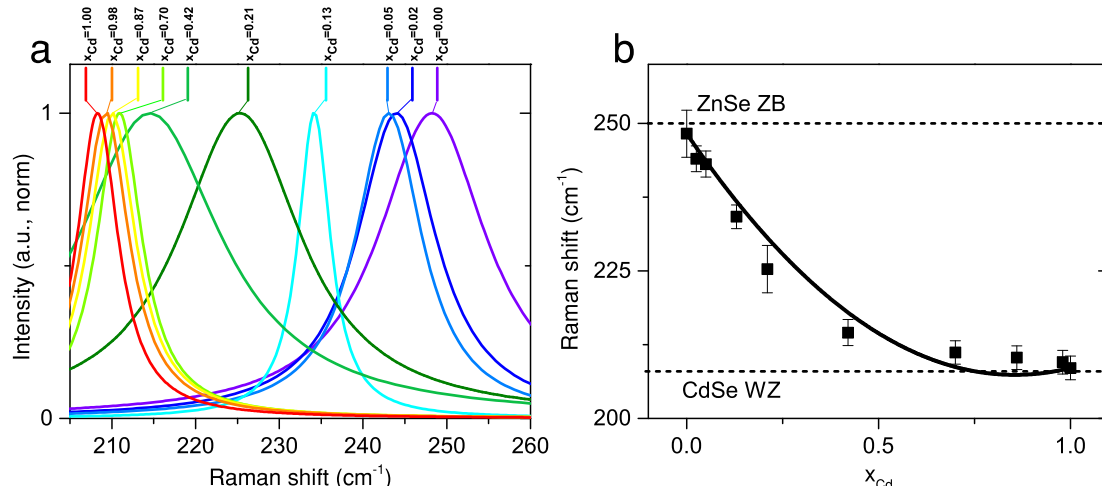


**Figure 3.6:** a) Lorentzian functions used to fit the shell-related LO Raman bands and b) shell-related LO phonon frequencies versus relative cadmium amount in the alloy. The bulk values for zinc blende ZnSe and wurtzite CdSe are displayed as lines. [125, 126] The solid line is a fit according to Bouamama *et al.* [124]

(Reprinted (adapted) with permission from Strain Engineering in InP/(Zn,Cd)Se Core/Shell Quantum Dots, Mona Rafiqpoor, Dorian Dupont, Hans Tornatzky, Mickael D. Tessier, Janina Maultzsch, Zeger Hens and Holger Lange. Copyright (2018) American Chemical Society.)

as indicative for the formation of solid solutions. [121] The gradual shift of the shell-related LO phonon frequencies is demonstrated in Figure 3.6 b. The frequency can be described by Vegard's law (equation 2.10) with a best fit of a second order polynomial:

$$\omega = \omega_{\text{CdSe}}x + \omega_{\text{ZnSe}}(1 - x) - b_{\text{LO}}x(1 - x), \quad (3.1)$$

where the value obtained for the bowing parameter from the fit curve is  $b_{\text{LO}} = 60 \pm 5 \text{ cm}^{-1}$ . This is in good agreement with previous works on bulk alloys. [63, 124] The absence of new Raman bands confirms, that there is no separation of minority domains in the synthesis approach of (Zn,Cd)Se solid solution shells. The transition from a zinc-blende to a wurtzite lattice in bulk alloys has no impact here. This confirms that changing the lattice geometry does not strongly influence the dynamic properties of the lattice. The information concluded from the study of the shell composition helps to compare the lattice mismatch between the core and the shell and to obtain the strain in the InP core. Similar to the previous discussion in Figure 3.3 b, the InP LO phonon shift collected from the Raman spectra leads to the strain estimation in the core. In Figure 3.4 the shift of both

core and shell-related LO phonons towards the plain InP peak from the initial benchmark sides (InP/ZnSe and InP/CdSe) was introduced. In Figure 3.7 a the Raman shift for the

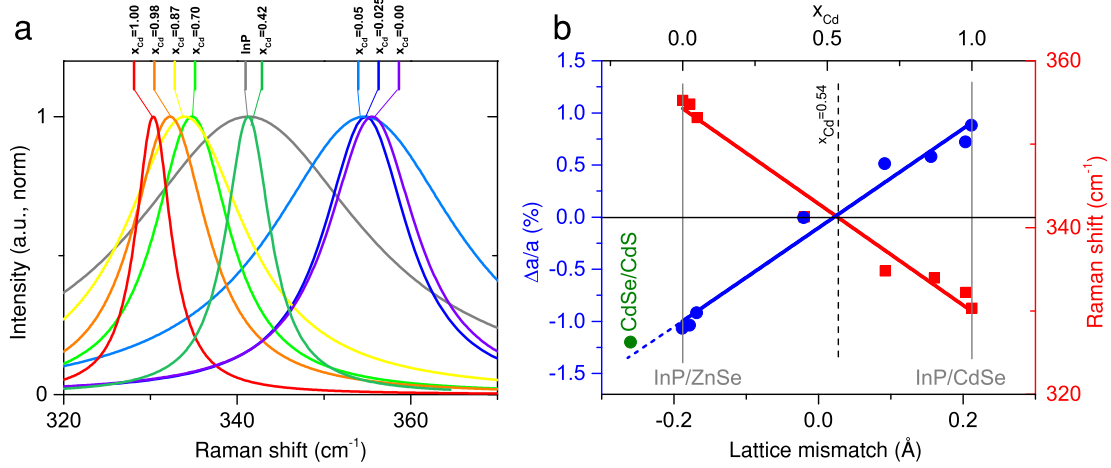


**Figure 3.7:** a) Lorentzian functions used to fit to the InP core LO frequency, b) LO frequencies in red and strain estimated by evaluating equation 2.22 in blue versus relative cadmium amount. The corresponding lattice mismatch ( $a_{\text{shell}} - a_{\text{core}}$ ) was estimated assuming Vegard's law[62]:  $a_{\text{shell}}(x) = a_{\text{CdSe}}x + a_{\text{ZnSe}}(1 - x)$ . [63, 124] The solid lines are linear fits. The dashed line corresponds to zero strain with the measured pure InP QD LO frequency of  $341.2 \text{ cm}^{-1}$ . The spectrum of the 42% Cd samples was excited in the infrared spectral region and subject to a specific analysis (Figure 8.3). (The green square corresponds to CdSe/CdS core/shell QDs.[84])

(Reprinted (adapted) with permission from Strain Engineering in InP/(Zn,Cd)Se Core/Shell Quantum Dots, Mona Rafipoor, Dorian Dupont, Hans Tornatzky, Mickael D. Tessier, Janina Maultzsch, Zeger Hens and Holger Lange. Copyright (2018) American Chemical Society.)

core-related LO is represented. The shifts of the InP core-related LO phonons towards the plain InP peak from each InP/CdSe and InP/ZnSe benchmark is clearly recognizable. In the case of the ZnSe shell, the shorter lattice constant of ZnSe relative to InP leads to a shortening of the InP bonds of the core/shell interface, while in the case of the CdSe shell the opposite effect occurs.

To obtain the strain in the core equation 2.22 is used, where the Grüneisen parameter is  $\gamma_{\text{InP}} = 1.24$  for InP.[119]  $\Delta\omega$  is calculated relative to the LO phonon of the pure InP QDs, which are assumed to be free of strain. The relative change of the lattice constant shown in Figure 3.7 b as a function of lattice mismatch based on Vegard's law. The strain in terms of the shell composition is modeled as a linear function and the best fit yields  $\frac{\Delta a}{a} x_{\text{Cd}} = 1.9x_{\text{Cd}} - 1$ . Again no deviation due to the lattice structure is observable, accordingly the core behavior is not related to the lattice configuration. According to these data,  $x_{\text{Cd}} = 0.53 \pm 0.05$  is the "strain free" composition, where the strain in the core changes from compressive to tensile, which is close to  $x_{\text{Cd}} = 0.48$  lattice matched composition for thin films of InP/(Zn,Cd)Se in other works.[63, 127, 128]

Comparing the linear behavior of lattice mismatch and strain with other works with a similar particle size,[84] suggests that the mismatch-strain relation derived here can be applied to a wider range of III–V and II–VI semiconductors. In Figure 3.3 b The data point for CdSe/CdS core/shell QDs with a comparable size is included.

The strain-mismatch dependency is used (in other works) for optimizing the material composition to optimize lasing threshold by reducing Auger recombination.[16]

In this Chapter the quantitative investigation of tuning lattice strain in InP/(Zn,Cd)Se QDs alloys by tuning the shell lattice constant was discussed. The lattice constant was tuned by modifying the alloy composition. A systematic shift of the shell-related Raman band, which is a sign of homogeneous formation of (Zn,Cd)Se shell alloys has been observed. The strain behaves linearly relative to the lattice mismatch between the core and the shell material. The strain was changed from compressive in case of a pure ZnSe shell to tensile for a pure CdSe shell. In between for the composition of  $\text{Zn}_{0.58}\text{Cd}_{0.42}$ , seems to be a successful implementation of strain-free core/shell QDs.

# 4 Optical properties of Core/Shell Quantum Dots/Quantum Rods in Micelles

In Chapter 2.2.3 the clustered CdSe/CdS QDs/QRs encapsulated in amphiphilic diblock-copolymer micelles were introduced as a water-soluble material. In this Chapter, the optical properties of these materials are studied by performing time-resolved photoluminescence spectroscopy. The effect of the clustering and the cluster size on the fundamental optical properties will be discussed. The stability and blinking behavior of these materials are studied by single particle investigations.

## 4.1 Blinking

Individual micelles were spin-coated on glass cover slides and investigated by time-resolved confocal photoluminescence (PL) spectroscopy. One of the most striking differences between the clustered and single encapsulated QDs/QRs is the abundance of any blinking behavior for the clustered NPs (Figure 4.1). While the PL intensity of the clustered QDs/QRs remains constant during the experiment time, the PL intensity of the single encapsulated QDs/QRs fluctuates between two on/off-states (Chapter 2.3.2). The excitation condition are not changed, thus a direct comparison is available. Because all clusters contain enough bright QDs/QRs, under continuous excitation they can constantly be luminescent. If one of the QDs/QRs in one micelle is in its off-state, it is probable that one or more QDs/QRs in the same micelle are in their on-state. This will result in an intensity fluctuation during the excitation, but a clear off-state does not appear. On the other hand, the on/off-state of the single encapsulated QDs/QRs are very distinct, which could also be confirmed by a spatial imaging of an enlarged region of the sample.[43] These results are also valid for the other clusters, an exemplary time trace for PI-*b*-PEG (small) cluster and single QDs/QRs is illustrated in Figure 4.2.

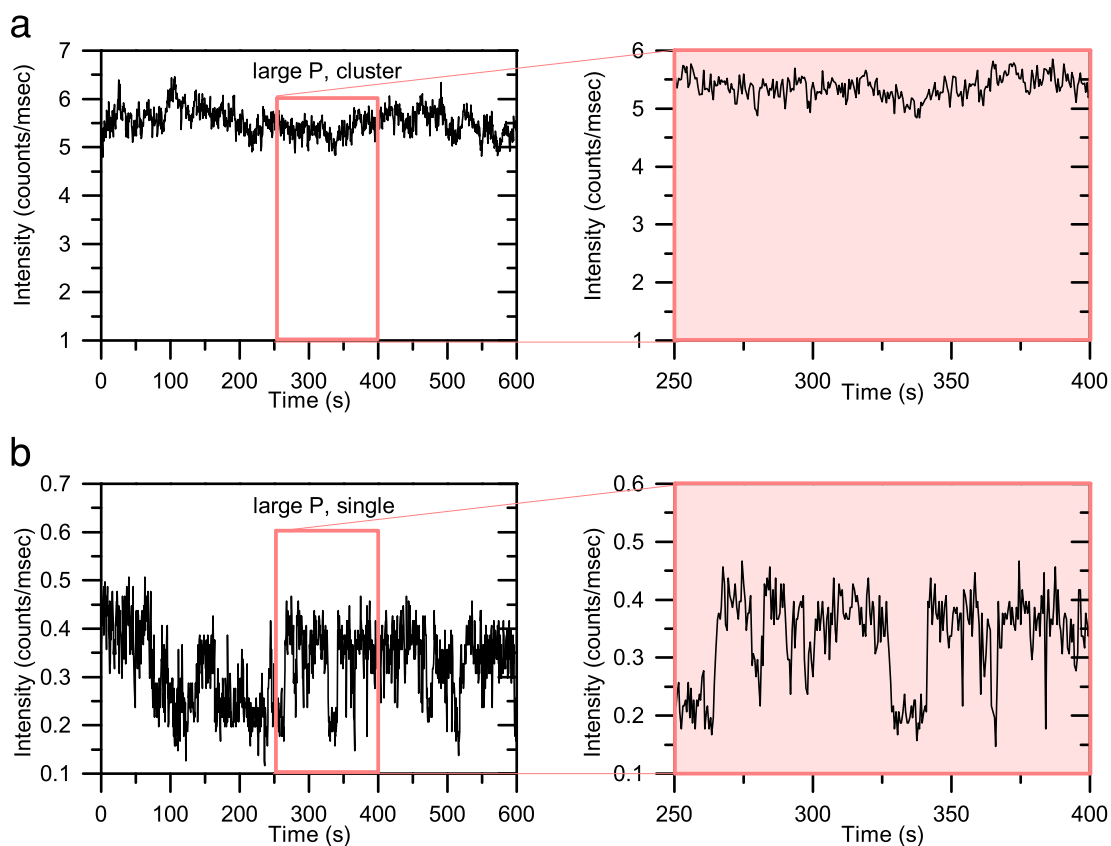


**Figure 4.1:** Time evolution of PL Intensity for a) clustered and b) single encapsulated QDs/QRs with medium polymer.

Reprinted (adapted) with permission from Clustering of CdSe/CdS Quantum Dot/Quantum Rods into Micelles Can Form Bright, Non-blinking, Stable, and Biocompatible Probes, Mona Rafiqpoor, Christian Schmidtke, Christopher Wolter, Christian Strelow, Horst Weller, Holger Lange. Copyright (2015) American Chemical Society.

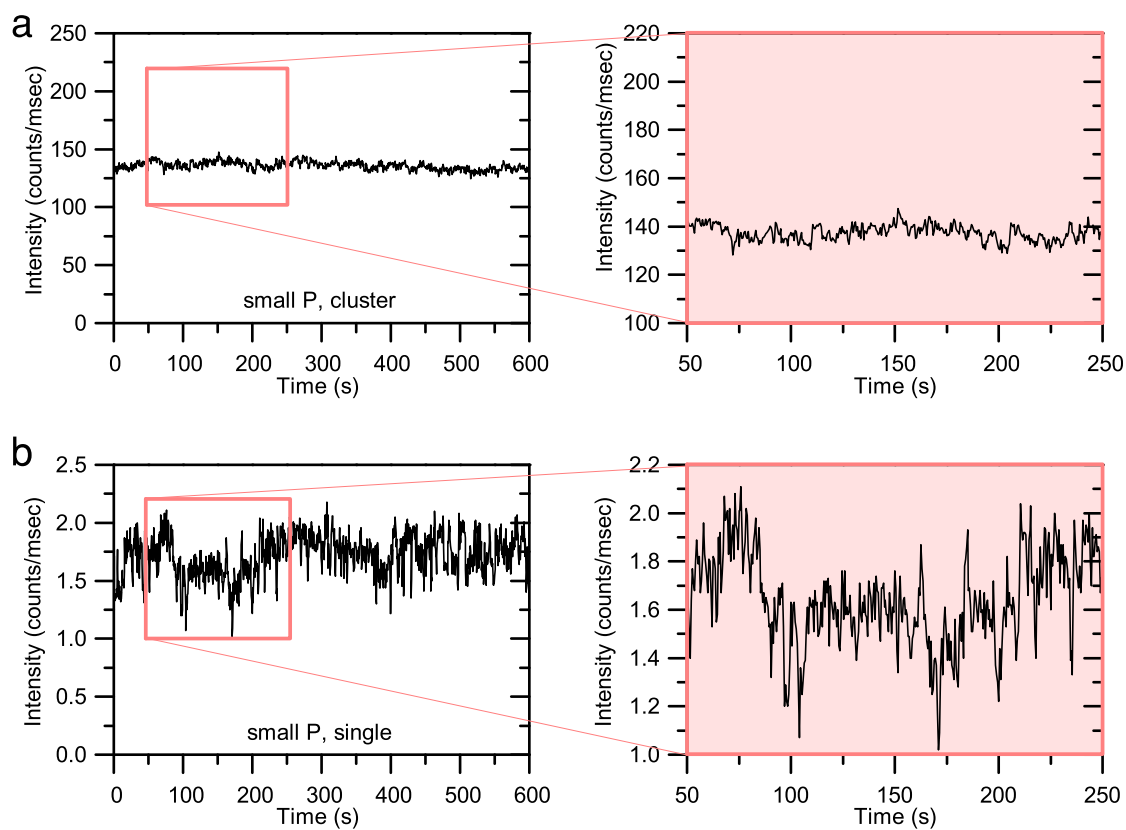


**Figure 4.2:** Time evolution of the PL Intensity of a) clustered and b) single encapsulated QDs/QRs with small polymer.

Reprinted (adapted) with permission from Clustering of CdSe/CdS Quantum Dot/Quantum Rods into Micelles Can Form Bright, N Non-blinking, Stable, and Biocompatible Probes, Mona Rafipoor, Christian Schmidtke, Christopher Wolter, Christian Strelow, Horst Weller, Holger Lange. Copyright (2015) American Chemical Society.

## 4.2 Photoluminescence Spectra and Decays

Figure 4.3 a shows the scan area for three different clusters and the corresponding single encapsulated QDs/QRs. For each sample a statistically relevant amount of micelles (bright spots in confocal scan microscopy) with different PL intensities are studied. The PL spectrum and PL decay for each spot on the sample are recorded and can directly be compared. The excitation conditions and illumination duration of each spot is not changed. The diffraction-limited resolution of the utilized set up is about 300 nm (FWHM of the

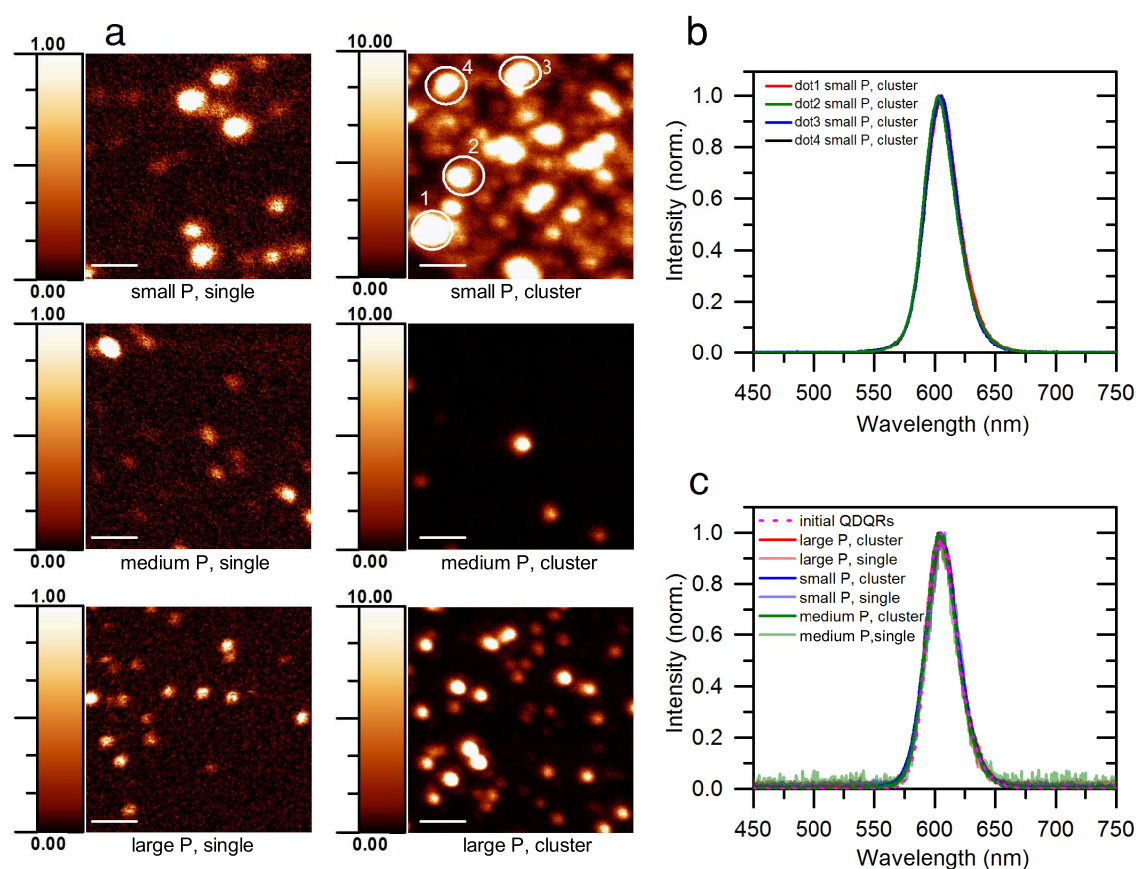


**Figure 4.3:** (a) PL scans of the investigated clustered QDs/QRs. The scale bars correspond to  $2.0 \mu\text{m}$ . The brightness scale bars conform to (counts/msec). (b) Exemplary PL spectra of different clusters of the same batch, corresponding to the structures highlighted in (a) by white circles. (c) Comparison of the PL spectra of the initial, the single encapsulated and the clustered QDs/QRs with different polymer weights.

Reprinted (adapted) with permission from Clustering of CdSe/CdS Quantum Dot/Quantum Rods into Micelles Can Form Bright, N Non-blinking, Stable, and Biocompatible Probes, Mona Rafipoor, Christian Schmidtke, Christopher Wolter, Christian Strelow, Horst Weller, Holger Lange. Copyright (2015) American Chemical Society.

laser spot), at which the clustered QDs/QRs emit more light than the single encapsulated QDs/QRs. The PL of the clusters is 10 times brighter than the singles (Figure 4.3 a). By

comparing the three different clusters across the sample surface no noticeable difference in the PL spectra can be observed. The shape of the PL spectra and the central wavelength are almost the same. The normalized spectra of the clustered and single encapsulated QDs/QRs do not differ from the initial synthesized QDs/QRs as seen in figure 4.3 c.

Figure 4.4 represent the PL decay curves of all samples including the initial QDs/QRs

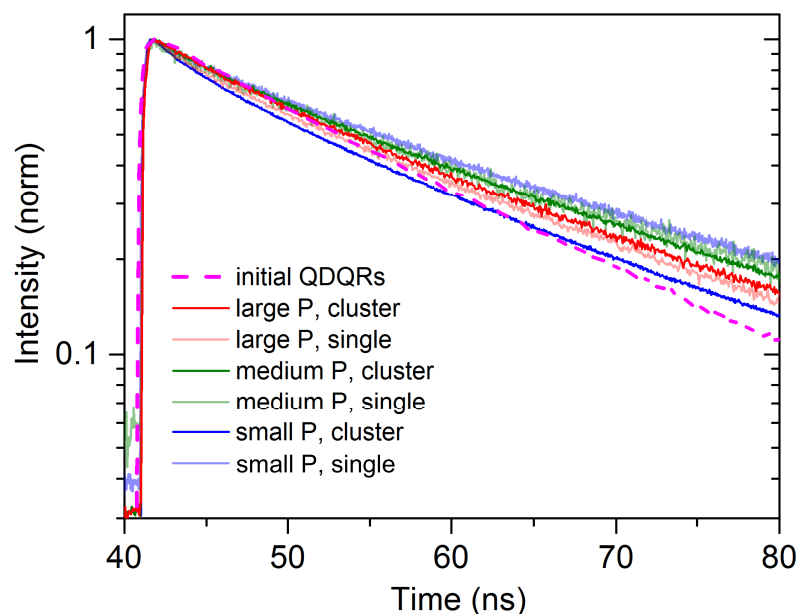


**Figure 4.4:** Photoluminescence decay curves of all QDs/QRs.

Reprinted (adapted) with permission from Clustering of CdSe/CdS Quantum Dot/Quantum Rods into Micelles Can Form Bright, N Non-blinking, Stable, and Biocompatible Probes, Mona Rafipoor, Christian Schmidtke, Christopher Wolter, Christian Strelow, Horst Weller, Holger Lange. Copyright (2015) American Chemical Society.

before encapsulation. The excitation fluence is the same for every measurement. The lifetime of the excitons in the lowest transition state are almost the same for each sample with a value of 19.8 ns. Exchanging the native ligands of QDs/QRs and varying the polymer and even encapsulating the QDs/QRs, seems to have negligible influence on the fundamental optical properties of the QDs/QRs.

### 4.3 Stability and Possible Interparticle Interactions

Tracking the luminescence intensity on longer time scales (10 s) by varying the pump fluence is a way to proof the optical stability of these materials. Figure 4.5 a-b shows the time traces of PI-*b*-PEG (large) clustered and single QDs/QRs for different excitation power during a continuous measurement. The PL decay was tracked for each excitation

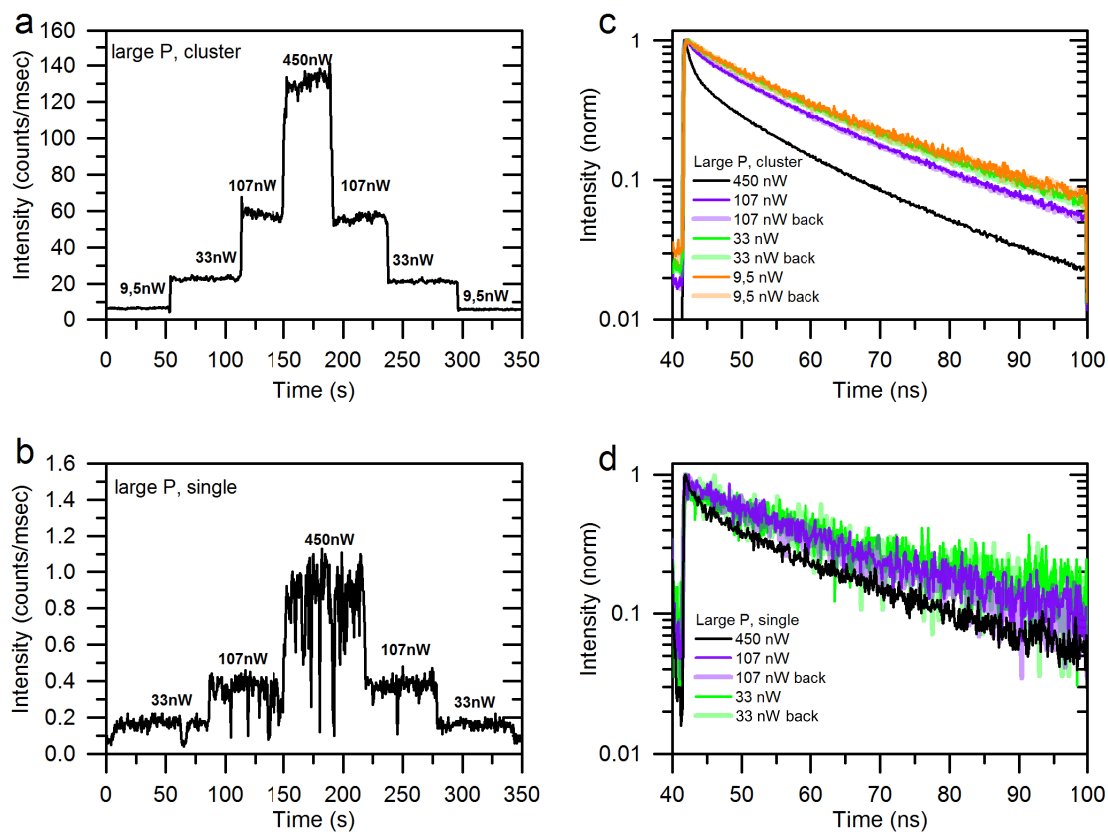


**Figure 4.5:** PL intensity traces for different excitation powers of a) large polymer clustered QDs/QRs and c) large polymer single QDQR and b) and d) the corresponding PL decays.

Reprinted (adapted) with permission from Clustering of CdSe/CdS Quantum Dot/Quantum Rods into Micelles Can Form Bright, N Non-blinking, Stable, and Biocompatible Probes, Mona Rafipoor, Christian Schmidtke, Christopher Wolter, Christian Strelow, Horst Weller, Holger Lange. Copyright (2015) American Chemical Society.

power. Figure 4.5 c-d shows the comparison of the decay curves at different excitation powers for clustered and single encapsulated QDs/QRs. The clusters remain bright without any blinking behavior, while the luminescence intensity of the single QDs/QRs fluctuates during the measurement. In both samples the obtained PL intensity remains unchanged for the same excitation power, which indicates that no physical damage or changes have happened after high power excitation. The possible generation of defects in the particle would reveal itself by fastening the PL decay (See Figure 8.6 d).

Increasing the excitation power leads to an increase of the average exciton population in the NCs. The increase of the exciton population can result in exciton-exciton interaction or even multiexciton Auger recombination and will influence the PL decay by shortening the lifetime. The biexponential behavior of the PL decay curve for the highest measured power ( $450 \text{ nW} \cong \langle N \rangle \leq 1$ ) in figure 4.5 d, indicates a biexcitonic effect for the single encapsulated QDs/QRs. In the case of clustered QDs/QRs the PL decay curve for the highest excitation power has a more prominent behavior. It could originate from either interactions between excitons or charges across the QDs/QRs. To understand further which interactions in the clustered QDs/QRs can cause this behavior, different inter-particle interactions are introduced and investigated in the next Chapter.



# 5 Inter-Particle Interactions between Core/Shell Quantum Dots/Quantum Rods

## 5.1 Nonradiative Recombination Channels in QDs/QRs

From an application point of view core/shell quantum dot/quantum rods are often used in scenarios as ensembles. One of the possible interactions that can occur in these ensembles is resonant energy transfer. As shown in the previous Chapter, in a highly excited situation the energy relaxation of the QDs/QRs may happen via multiexcitonic decay.[129] The multiexciton recombination can often compete against the energy transfer.[130] Depending on the spatial position of the QDs/QRs, these two processes can be convolved. The introduced material in the previous Chapter is a convenient platform for studying the interplay of energy transfer and multiexciton Auger recombination. The inter-particle distance plays a main role for studying these kind of processes. In this Chapter, spacer ligands are used for controlling the distance between the QDs/QRs in the micelles (Chapter 2.2.3).

For tracking these processes time-resolved photoluminescence and transient absorption experiments are performed. In this Chapter, it is shown that energy transfer between the QDs/QRs is extremely efficient. It can result in a collective excited state dynamic. This Chapter starts with an introduction of the two main nonradiative processes: Förster resonance energy transfer and multiexciton Auger recombination. Later on, a coupling of these two interactions is discussed.

### 5.1.1 Förster Resonance Energy Transfer

Förster resonance energy transfer[131, 132] and Dexter[133] electron transfer are the main nonradiative interactions, that can take place between two individual particles in a non-conductive environment. In both cases the overlap of the emission spectrum of the donor and absorption spectrum of the acceptor is required.[134–137] Besides Dexter electron transfer requires an overlap of the electronic wavefunctions and is effective on sub-nanometer

scales. The energy transfer rate in this case varies with the distance between the particles. The shell dimensions of the QDs/QRs used in this work and also the space occupied by the passivating ligands allow neglecting this kind of energy transfer in core-shell NC ensembles.

Förster resonance energy transfer (FRET) on the other hand is associated with a charge-neutral coulombic dipole-dipole interaction between an excited donor and a ground-state acceptor pair. Here only the overlap between the emission and absorption spectra is required. The energy transfer rate  $k_{ET}$  depends on the distance between the particles in a scale of  $r^{-6}$  and requires a maximum distance of 10 nm.[138, 139] The FRET quantum yield or in other words FRET quantum efficiency ( $E$ ) is defined as the fraction of energy transfers per donor excitation and is given by

$$E = \frac{k_{ET}}{k_r + k_{ET} + \sum k_{nr}}, \quad (5.1)$$

where  $k_{ET}$  stands for the energy transfer rate from donor to acceptor,  $k_r$  is the radiative recombination rate and  $k_{nr}$  corresponds to the nonradiative recombination (nr) rate. The energy transfer rate also depends on the excited donor state population relaxation, but this relaxation is dominated by the donor fluorescence rate. Thus, the energy transfer rate is commonly described by the fluorescence lifetime of the donor  $\tau_D$  and the effective distance or Förster distance ( $R_0$ ) and is given by:[131, 132, 140–142]

$$k_{ET} = \frac{1}{\tau_D} \left( \frac{R_0}{r} \right)^6 \quad (5.2)$$

This approximation is also known as point-dipole approximation.[143, 144] Here  $r$  stands for the donor-acceptor distance. The Förster distance ( $R_0$ ) depends on several components, one of the main component is the relative orientation of the donor and acceptor ( $\kappa^2$ ):[140]

$$R_0^6 = 8.785 \times 10^{-5} \frac{\kappa^2 \Phi_D J}{n^4} \quad (5.3)$$

Here  $\Phi$  corresponds to the quantum yield of the donor in absence of the acceptor and  $J$  represent the overlap integral between the emission spectrum of the donor and the absorption spectrum of the acceptor.  $n$  is the refractive index.[140, 145] Furthermore,

$$J = \int \lambda^4 F_D(\lambda) \sigma_A(\lambda) d\lambda, \quad (5.4)$$

where  $\sigma_A$  represents the molar absorption coefficient of the acceptor.[146] Equation 5.1, 5.2 and 5.3 show that the FRET quantum yield  $E$  depends on  $\kappa$ . If the distance between the donor and acceptor is smaller than their size,[133, 147, 148] which is usually the case in NCs, the point approximation can not be used any more and  $E$  will be strongly depend on the dimension and shape of the NCs. This fact can also be used to modify FRET systems with specific desires. Hadar *et al.* showed that small NCs can provide better

sensing properties [149–151] for low analyte concentration while larger NCs can be used in the detection of multiple acceptors.[152–155]

The  $r^6$  dependence for the FRET rate (Equation 5.2) will then change. For multipolar interaction the FRET rate will extended to:[143, 156]

$$k_{ET} = \frac{1}{\tau_D} \left( \frac{R_0}{r} \right)^S \quad S \geq 6, \quad (5.5)$$

where  $S$  corresponds to the multipolar exponent, for example for dipole-quadrupole interaction  $S$  would be equal to 8.[143] Size variations in NCs are associated with a band gap distribution. FRET is then the main interaction that can happen between NCs, where the excited large-bandgap (blue) NCs transfer nonradiatively energy to the small-bandgap (red) NCs. In this way the blue NCs act as donor and the red NCs as acceptor. In other words, within the blue NCs, energy is relaxed by radiative and nonradiative recombination. Note, that blue NCs are associated with smaller size NCs and red NCs with larger size NCs.

### 5.1.2 Auger Recombination

As mentioned in Chapter 4.3, in highly excited NCs, multiexcitons are generated. In such a case Auger recombination is the dominant nonradiative recombination channel.[34, 157, 158] In this process the energy of one exciton is transferred to a third charge (electron or hole) and leads to a further excitation of this charge. The re-excitation of the third charge to higher energy states can either occur in the NCs or outside of the NCs. In the second case one can speak of Auger ionization. In Bulk semiconductors the Auger rate ( $r_A$ ) is defined as a function of carrier density ( $n_{eh}$ ), in which they have a cubic relation[34, 159]

$$r_A = \frac{dn_{eh}}{dt} = -C_A n_{eh}^3, \quad (5.6)$$

where  $C_A$  stands for the Auger constant and will be defined in the following. From equation 5.6 the Auger time constant  $\tau_A$  can be defined as

$$\frac{1}{\tau_A} = C_A n_{eh}^2. \quad (5.7)$$

Consequently, the Auger time constant changes continuously with the reduction of carrier density. In NCs the Auger time constant is quantized, because of the quantization of the NC population, which also may change the cubic relation between Auger rate and the carrier density in equation 5.6. Considering the cubic relationship and an effective carrier density (carrier density per NCs volume  $N/V_0$ ), the Auger constant  $C_A$  is defined by

$$C_A = V_0^2 (8\tau_2)^{-1}. \quad (5.8)$$

Equation 5.8 shows that Auger recombination depends on the volume and the size of the NCs.

## 5.2 Coupled Auger Recombination and Energy Transfer

Exciting an ensemble of NCs with a size distribution (which leads to statistically distributed bandgaps), can lead to an interplay between Auger recombination in one NC and FRET with a neighboring NCs. For investigating the interplay between these two processes, the QDs/QRs in micelles are a stable and convenient platform.

An approach to control the distance between QDs/QRs within the micelles is to functionalize the NCs with polymer ligands of defined weight before the encapsulation which was explained in Chapter 2.2.3.

### 5.2.1 Characterization of the Encapsulated QDs/QRs

Four clusters with different inter-particle distances were provided (Table 8.2). Cluster 1 constitutes large micelles with a long average inter-particle distance. Cluster 2-4 have mainly the same size and a decreasing inter-particle distance (Figure 5.1 a). The basic characterization of these set of ensemble NCs is illustrated in Figure 5.1. TEM, steady-state absorption and photoluminescence (PL) spectroscopy, small angle x-ray scattering (SAXS) and dynamic light scattering measurements (DLS) were performed for the characterization. As shown in Figures 5.1 a and e (TEM and DLS measurements), the clusters with native ligands (cluster 4) and those with smaller polymer ligands (clusters 2 and 3) all have similar sizes, but the cluster prepared with the 14.8 kDa polymer ligand (cluster 1) are larger (Table 8.2).

The CdSe core-related absorption appears at 605 nm. The broad shell-related CdS absorption is located at shorter wavelengths (460 nm) (Figure 5.1 b). The PL spectra of the clusters are broader and red shifted in comparison to the single encapsulated QDs/QRs. The shorter the inter-particle distance, the higher is the probability for resonance energy transfer from blue NCs to the red NCs. This leads to the red shift of the spectrum (due to the smaller band gaps of the red NCs) (Figure 5.1 c).

TEM images in Figure 2.8 a confirms the fact, that the distance between the NCs in the micelles are smaller than the actual size of the NCs. A distance estimation according to the TEM analysis shows an average surface to surface distance (surface of the QDs/QRs) of 2.1 nm for cluster 4, which is smaller than the size of the QDs/QRs (CdS core QDs have a diameter of 5.3 nm and CdSe shell QRs have a length of 25.2 nm ). This changes the point-dipole approximation of equation 5.2 for the Förster rate to a  $r^{-4}$  surface dependency of the NCs.[143, 160–162]

It is important to notice, that SAX measurements present the center to center inter-particle distances (between the QDs/QRs). The scattering vector ( $Q$ ), which is the difference be-

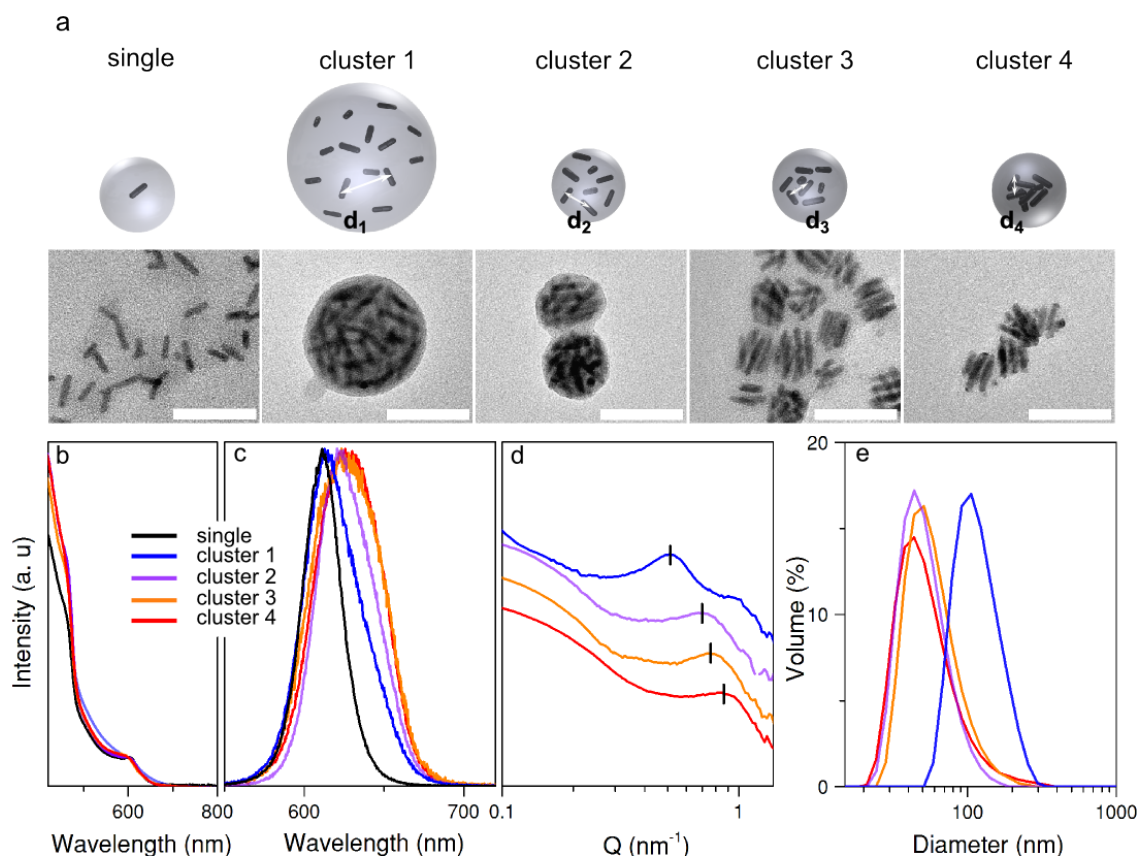


**Figure 5.1:** a) TEM images of the investigated samples. The scale bars correspond to 50 nm. The clustered NCs are labeled by the most dense cluster having the largest number. b) absorption and c) Photoluminescence spectra of the samples. d) SAXS spectra and e) DLS statistics of the samples.

tween the incoming and out going beam wavevector ( $k - k'$ ) is related to the scattering angle ( $\theta$ ). From the measured angle in SAX analyzes, the  $Q$  values of each sample (Figure 2.8 d) can be estimated (Equation 8.4).[25] The observed shift in Figure 2.8 d of the scattering vector  $Q$  toward larger  $Q$ -values confirms a decrease of the inter-particle distance between the NCs in the micelles of cluster 1 to cluster 4.

### 5.2.2 Biexciton Generation

In order to increase the exciton population  $\langle N \rangle$  in the NCs, the excitation power was increased. Time and wavelength resolved spectroscopy was performed to record the PL decays (Figure 5.2). An approach established by Klimov *et al.*[163], was used to calibrate the excited carrier population density. One can also estimate the excited carrier population by knowing the focal conditions in the ensemble solution and the absorption cross section[164–167] of the NCs at the exciting wavelength. By increasing the exciton population (increasing the excitation power) in both, the dense cluster 4 and single encapsulated QDs/QRs, the shape of the PL decay curve changes from mono-exponential to a biexponential function (Figure 5.2 a and c). For an exciton population below the biexcitonic threshold ( $\langle N \rangle < 1$ ), the excitons decay monoexponentially. In a regime for generating multiple excitons ( $\langle N \rangle \geq 1$ ), Auger recombination is the dominant nonradiative recombination, resulting the multiexponential decay of the excitons (Figure 5.2 a and c).[34, 164, 168, 169] To distinguish the two regimes in the experiment data, one can normalize the PL decay curves to the long mono-exponential tail of the single-exciton decay curve (Figure 5.2 b and d). A faster decay component at the early time after the excitation is observable. This fast component belongs to the multiexciton decay.[34, 130, 164]

The calibration approach of the exciton population can be achieved by removing the long-time mono-exponential term of the PL decays. Figure 5.2 b inset indicates that the build up of the biexciton threshold occurs at  $10 \mu W$ . One can normalize further the PL decays to the biexciton contribution and find out the threshold of three excitons, which appears at  $20 \mu W$  (Figure 8.7). Assuming the photon density seen by each QD/QR in the micelle is the same, the  $10 \mu W$  can be associated with one exciton per QD/QR. Switching to the dense cluster 4, one can recognize the general fastening of the PL decays. The biexciton behavior is much more prominent even for lower excitation powers. Because the excitation conditions for single encapsulated QDs/QRs and cluster 4 are the same, the initial excited carrier population remains the same. Earlier in this Chapter Auger recombination was introduced as a non-distance-depended process, which makes the scenario of cluster 4 in Figure 5.2 c and d interesting.

The difference between cluster 4 and single encapsulated QDs/QRs at lower excitation

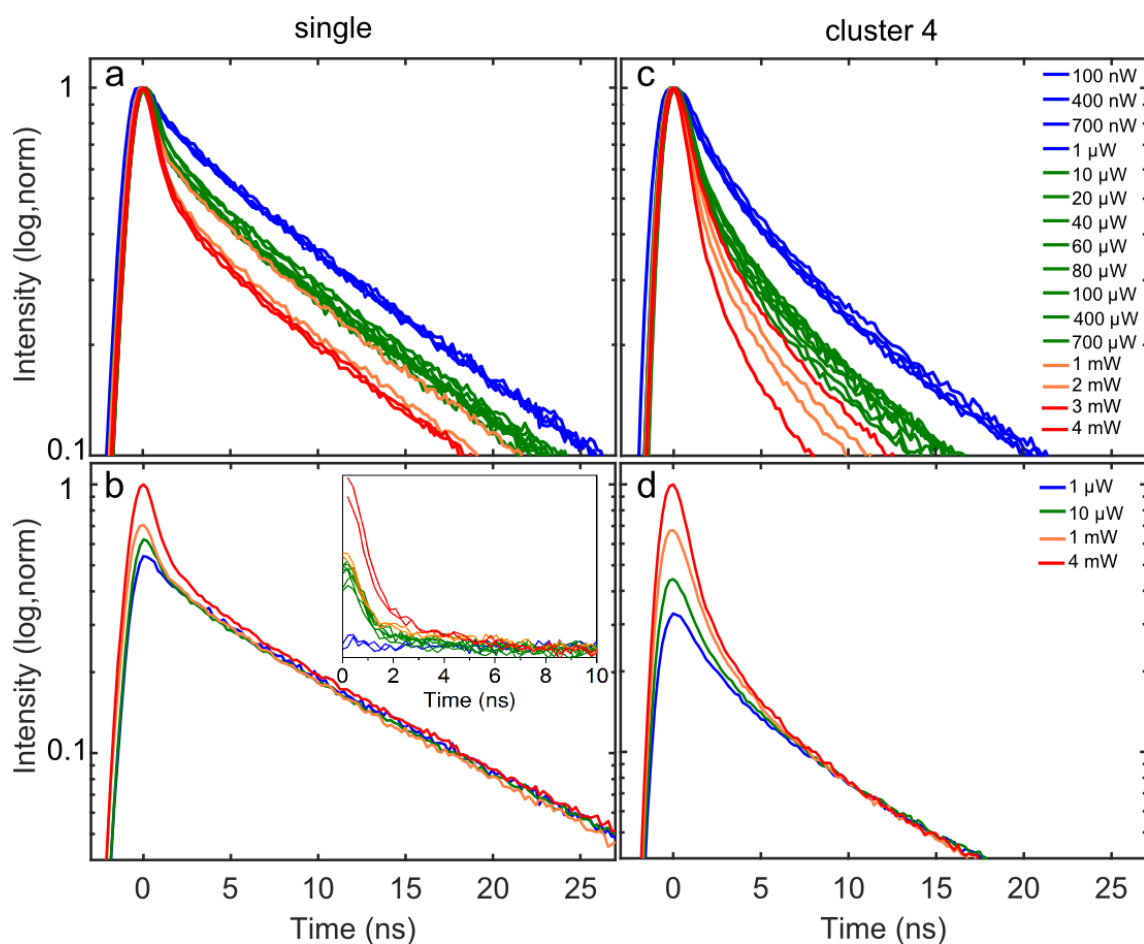


**Figure 5.2:** Spectral integrated PL decay of a) single NCs and c) cluster 4 for different excitation powers. The spectra were normalized to the PL maximum. b-d) Same spectra as in (a-c), but normalized to the tail of the PL decay. For the inset in part (b), the slow decay component was removed in order to show the onset of biexciton recombination.

power in Figure 5.2, where no multiexciton recombination contributes to the relaxation dynamic, can only stem from the inter-particle interaction. This effect can be observed by comparing the different clusters (1-4). Figure 5.3 confirms that the change in the faster component of the multiexponential decay curves is related to the distance between the QDs/QRs in the micelles. Cluster 2 has the same behavior as single encapsulated QDs/QRs. The smaller the distance between the QDs/QRs in the micelle, the faster the first component (the component at the earlier time after excitation) of the multiexponential decay.

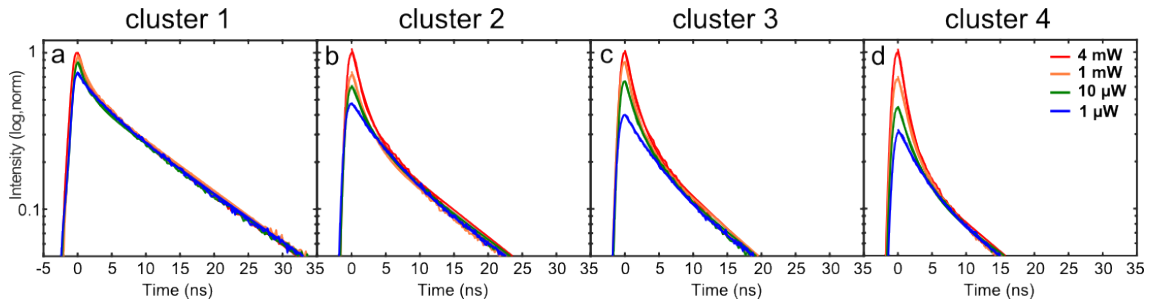


**Figure 5.3:** Spectral-integrated PL decays of cluster 1-4 normalized to the single-exciton (long-duration) PL decay tail.

### 5.2.3 Förster Resonance Energy Transfer Analysis

In a regime of  $\langle N \rangle < 1$  no multiexciton can be generated. FRET can be considered as the main inter-particle interaction in this excitation regime. Spectral and time resolved PL measurements are an appropriate way to analyze this effect. Figure 5.4 a shows a streak camera map for single encapsulated QDs/QRs. The time-integrated PL spectrum for this sample is shown in Figure 5.4 b. The marked areas in the spectrum represent the different spectral components used for analyzing the impact of energy transfer in Figure 5.4 c-g.

The single encapsulated QDs/QRs decays mono-exponentially over the whole spectrum with an estimated lifetime of 11 ns (Figure 5.4 c). Cluster 1 with a larger amount of QDs/QRs and a larger average inter-particle distance follows the single encapsulated QDs/QRs and decays mostly in the same way (Figure 5.4 d). With decreasing inter-particle distance in clusters 2-4, the splits of the different spectral components appear to be more pronounced (Figure 5.4 e-g). The red components in all clusters behave almost like the single encapsulated QDs/QRs. The blue components decay much faster, which is an indication of a Förster resonance transfer. The blue component corresponds to the particles with larger band gaps (blue NCs), while the red one corresponds to the NCs with smaller bandgap (red NCs). The blue NCs can transfer energy nonradiatively to the red NCs (and

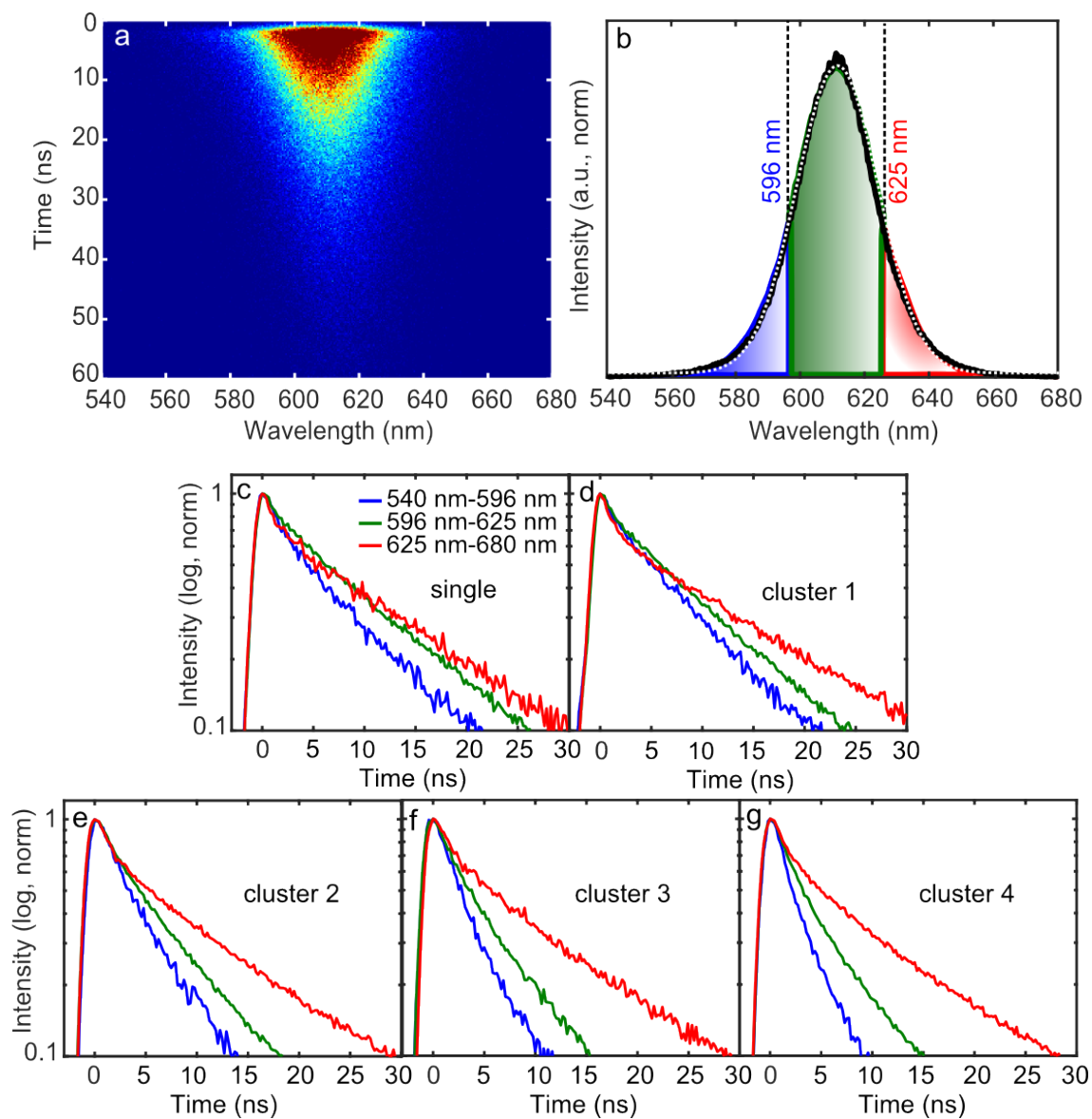


**Figure 5.4:** a) Streak camera map of single NCs excited with  $1 \mu\text{W}$  at  $418 \text{ nm}$ . b) Time-integrated PL spectrum from the data set presented in (a). The three spectral regions are used for the wavelength-resolved analysis. Spectral-resolved PL decays of c) single NCs, d) cluster 1, e) cluster 2, f) cluster 3 and g) cluster 4. All samples were excited with the same conditions.

green), which make them the donor in FRET. Assuming the blue NCs as donor, one can estimate the average inter-particle distances from the decay constants of the different spectral components.

$$\frac{1}{\tau_{tot}} = \frac{1}{\tau_r} + \frac{1}{\tau_{ET}} \quad (5.9)$$

The inter-particle interaction does not take place for the single encapsulated QDs/QRs, thus the measured time constant for the single encapsulated QDs/QRs can be taken as the radiative time constant.

$$\frac{1}{\tau_{tot}} = \frac{1}{\tau_r}. \quad (5.10)$$

According to equation 5.2 and including the  $r^{-4}$  relation for the QDs/QRs ensemble, one can estimate the relative inter-particle distance of the clusters, by normalizing these extracted values to the SAXS values for the dense cluster 4 (Table 5.1).

**Table 5.1:** Comparison of the obtained inter-particle distances in the micelles from SAXS and FRET analysis.

Experiment	$d_{cluster1}$ (nm)	$d_{cluster2}$ (nm)	$d_{cluster3}$ (nm)	$d_{cluster4}$ (nm)
SAXS	12.3	9.1	8.3	7.3
FRET	-	9.8	7.9	7.3

#### 5.2.4 Coupled Förster Resonance Transfer and Auger Recombination

More information can be gained by extending these investigation and increasing the excitation power. Figure 5.5 shows the same spectral components as in Figure 5.4. The excitation power increases from left to right. From top to bottom the inter-particle distance decreases. The first column in Figure 5.5 represent the same data set as in Figure 5.4. The lifetime of the excitons shortens in the case of single encapsulated QDs/QRs in the first row. This indicates multiexciton generation.

The split in the spectral component is less strong for increasing excitation power, which is mostly a result of a strong change in the red part of the spectrum. Comparing the different columns confirms the distance-dependence of this effect. The change in the blue part of the spectrum can be explained by the contributions of FRET and an additional part of Auger recombination with increasing the excitation power by:

$$\frac{1}{\tau_{tot}} = \frac{1}{\tau_r} + \frac{1}{\tau_{nr}} \quad (5.11)$$

$$= \frac{1}{\tau_r} + \frac{1}{\tau_{ET}} + \frac{1}{\tau_{Aug}}. \quad (5.12)$$

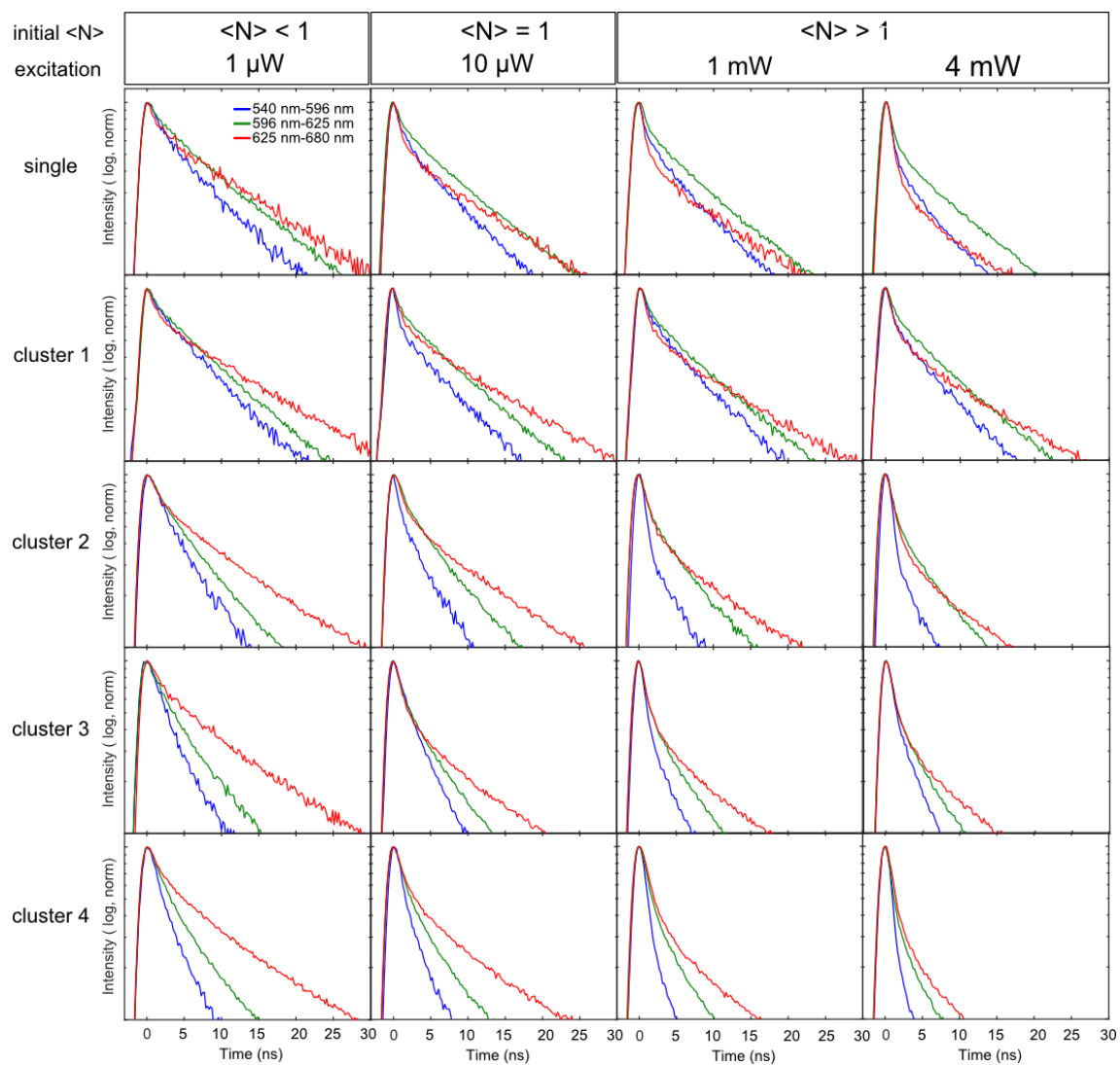


**Figure 5.5:** Spectral-resolved PL decays (wavelength regimes selected the same way as for Figure 2.4b) of each sample in different initial exciton population regimes.

Let's focus on the second column to understand the behavior of the blue and red part of the spectrum. The second column presents the data, where the exciton population reaches the value of  $\langle N \rangle = 1$ . To understand the fast component at the early times after excitation for the different spectral component in this power regime, one can follow again the procedure of calibrating the exciton population and removing the long tail of the single exponential component.

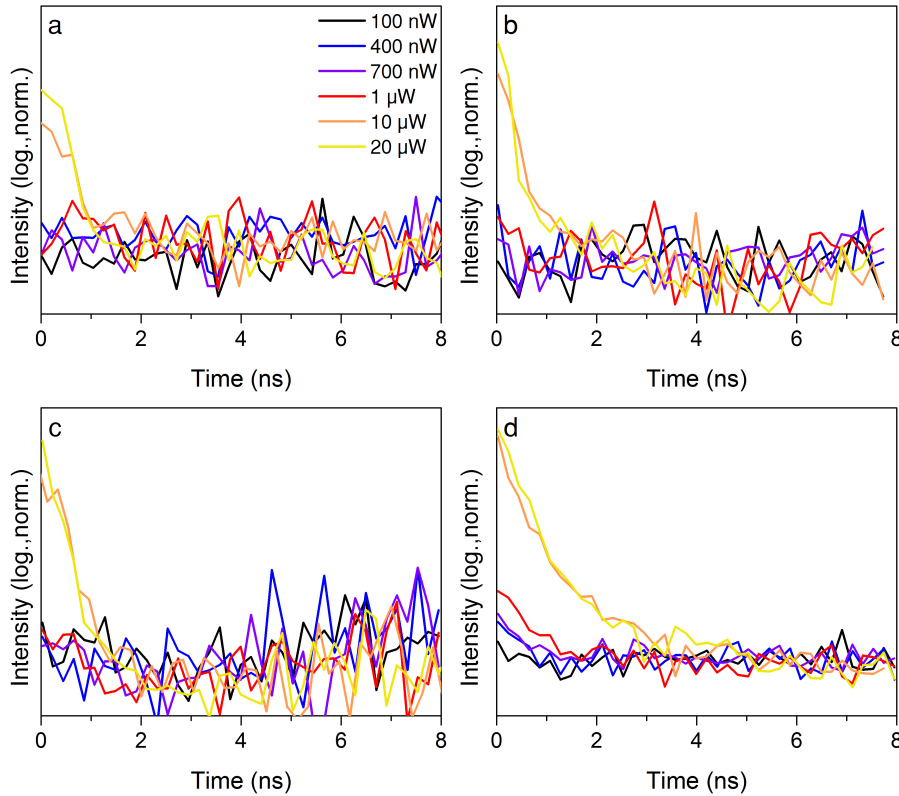


**Figure 5.6:** To differentiate between  $\langle N \rangle \leq 1$  and  $\langle N \rangle > 1$ , the spectral resolved PL decays (blue part and red part) were normalized to the lowest power PL decay (at 100 nW), the long time component was removed. (wavelengths selected the same way as in Figure 5.4) a) Blue part and b) red part of single encapsulated QDs/QRs spectrum. c) Blue part and d) red part of the cluster 4 spectrum. The obvious difference between (c) and (d) at lower power confirms the FRET from blue to red NCs, which leads to an increase of  $\langle N \rangle$  at lower power regime.

To understand the interaction between the QDs/QRs in the clusters, one can compare the biexciton onset for different spectral component between single QDs/QRs and clustered QDs/QRs. Figure 5.6 presents a comparison of the PL decays of the blue and red NCs as single NCs and in the dense cluster 4. The single blue (Figure 5.6 a) and red (Figure 5.6 b)

NCs behave as the spectral integrated ensemble of single NCs (Figure 5.2). The threshold for observing multiexciton recombination is at  $10 \mu\text{W}$ . The same is valid for the blue NCs (Figure 5.6 c) in the dense cluster 4. For the red NCs (Figure 5.6 d) in cluster 4, a biexponential behavior can already be observed at  $1 \mu\text{W}$ , while an excitation power of  $10 \mu\text{W}$  results in higher-order multiexciton recombinations. To track the timescales of energy transfer, pump-probe TA spectroscopy was performed. These studies disuses only the core-related absorption bleach. The different spectral components were compared after the thermalization into the lower transition state ( $1S$ ).

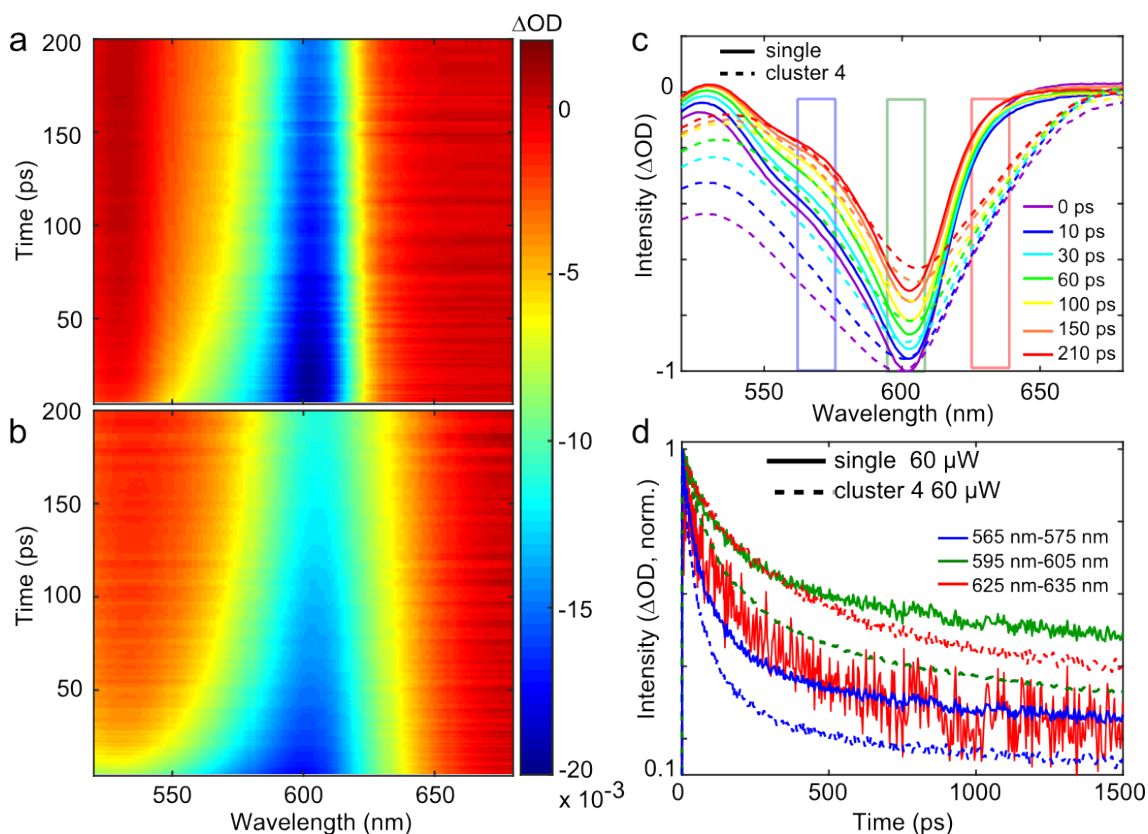


**Figure 5.7:** TA maps of the core QDs a) single NCs and b) cluster 4. c) Spectral cuts of the QD core spectral region of single NCs (solid lines) and cluster 4 (dashed lines). The spectra were normalized relative to the bleach maximum, set to  $t=0$ . d) TA dynamics for three representative spectral regimes,  $t=0$  was set to the moment of photoexcitation.

Figure 5.7 shows the data measured with an excitation power correlating to an exciton population of  $\langle N \rangle = 1$ . The spectra of single encapsulated QDs/QRs and cluster 4 both narrow during the first  $100 \text{ ps}$  (Figure 5.7 c). The spectra behave differently for the blue part and red part of the spectrum, which is more distinct in the cluster 4 spectra. For the single encapsulated QDs/QRs the dynamic of the blue and red part of the spectrum in the

selected areas are almost similar. The green part of the spectrum represents the  $1S$  central bleach (excitonic bleach), which is occupied with excitons and has a longer lifetime. In the case of clustered encapsulated QDs/QRs (cluster 4), the dynamic of the blue part of the spectrum is faster than the other parts of the spectrum, which is also the main reason of the asymmetric spectra in Figure 5.7 c. This evidences the energy transfer from the blue NCs to the red NCs.

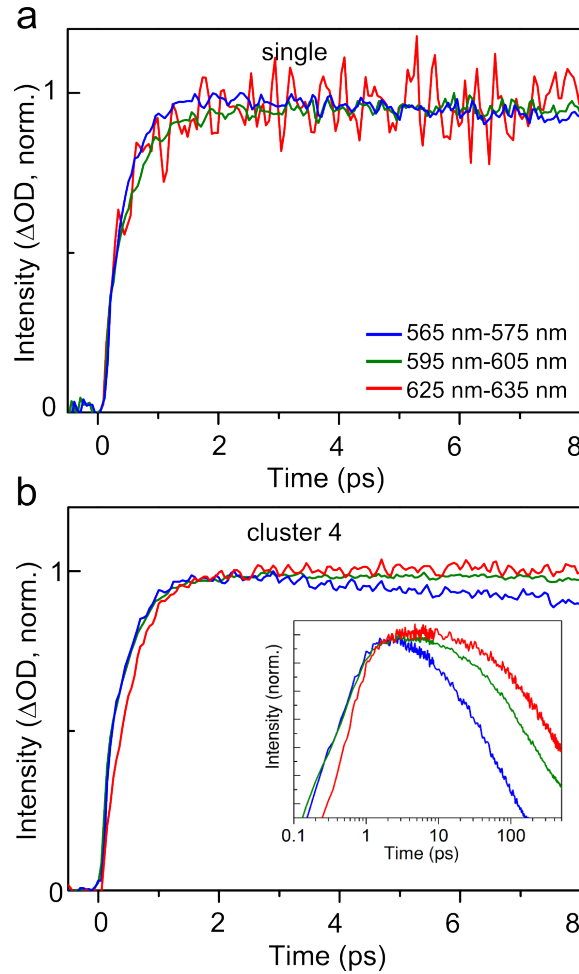


**Figure 5.8:** The same dataset as in Figure 5.7 d, TA dynamic traces for three representative spectral regimes of (b) single NCs and (c) cluster 4.  $t = 0$  was set to the moment of photoexcitation.

A zoom in to the first 8 ps of the TA dynamic in Figure 5.8 highlights this effect better. At the first 8 ps no spectral sensitivity can be observed for the single encapsulated QDs/QRs. The energy transfer from the blue NCs donor in cluster 4 begins in the early 2 ps after excitation. The transferred energy to the red NCs in cluster 4 can be confirmed by the decrease of the blue NCs dynamic at 2 ps while the red NCs bleach increases (Figure 5.8 b). The energy transfer from the blue NCs to the red NCs leads to a further excitation of the

red NCs. This effect is described in Figure 5.9. For the case of a low exciton population,

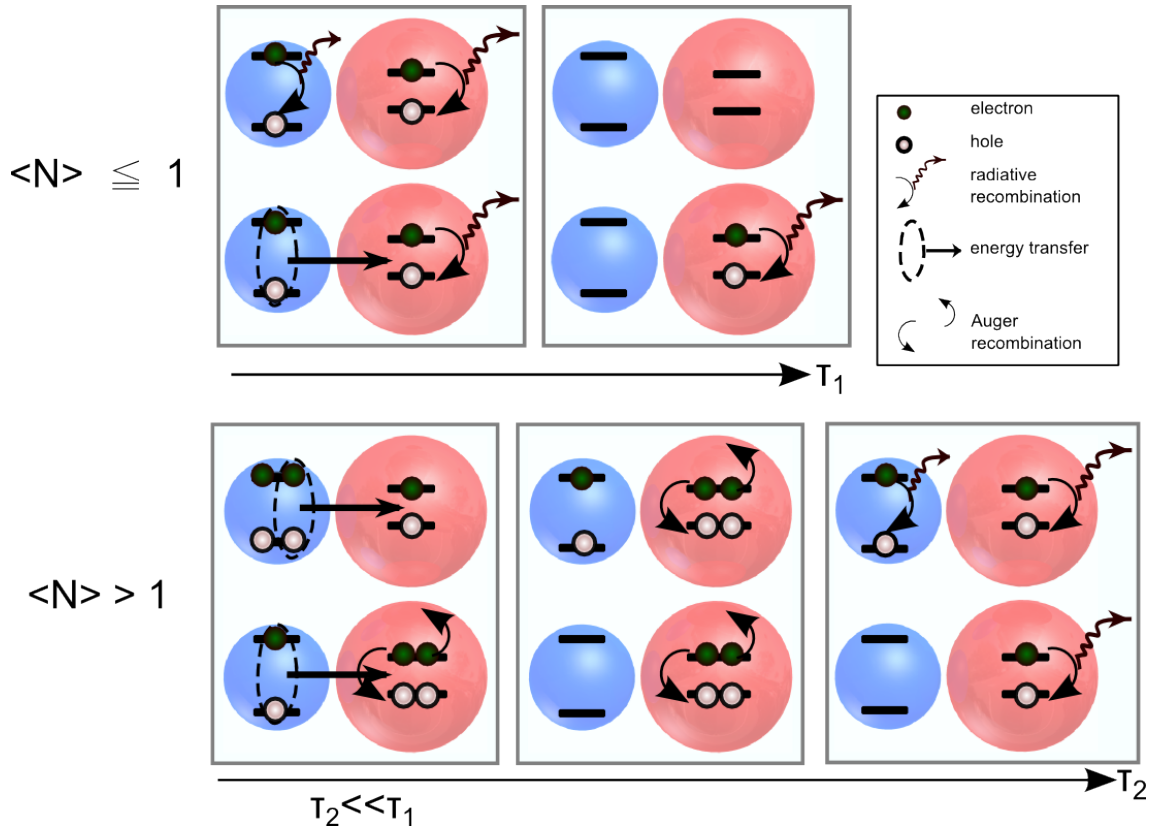


**Figure 5.9:** Schematic illustration of the processes contributing to the energy relaxation of clustered NCs.

an efficient energy transfer was observed in the PL measurements (Figure 5.9 top). This leads to a decreasing lifetime of the blue NCs and increase of the red NCs radiative recombinations. If the initial exciton population increases, a combination of energy transfer and multiexciton generation will happen. An already excited red NC accepts energy from the neighboring blue NC, which leads to the generation of a multiexciton in the red NC. The multiexciton recombination is very fast and depends on the transfer rate of the blue NCs. The relative amount of the multiexciton recombination generated by these collective processes scales with the excitation power and the energy transfer probability (distance between the NCs). This effect happens for an exciton population of  $\langle N \rangle < 1$  and an average inter-particle distances below 10 nm.

This effect can have a significant impact for compact light source devices, where the distances between the NCs become smaller. The decrease of the radiative recombination of the NCs by the generation of the triggered multiexcitons is a disadvantage for these application fields. The triggered multiexciton may lead to the annihilation of the photogenerated carrier before the charge can be separated from the NCs. Next Chapter is followed by the

importance of the charge separation for specific applications.

## 6 Charge Separation in Quantum Dots

One important application of QDs is their usage in solar cells or in devices, where photoexcitation (light energy) and electricity (electrical energy) are coupled with each other. Charge separation is a main procedure for applications containing converting light to electrical energy. This process can also be controlled by multiexciton generation, hot electron extraction or even plasmonic effects.[170–175]

### 6.1 Coupling of CdSe QDs to Methyl Viologen

One common way for charge separation is to attach NCs to a molecular acceptor, in the way that an excited electron in the NCs can be extracted by the molecule.

In this Chapter, very small CdSe QDs (diameter of 1.7 nm) were attached to methyl viologen ( $MV^{2+}$ ).[176–180] An illustration of this process is shown in Figure 6.1. The absorption spectrum of bare CdSe QDs features the CdSe 1S absorption at 465 nm.<sup>1</sup>

#### 6.1.1 Transient Absorption Dynamics of Charge Transport

Transient absorption (TA) is an appropriate way to study the fast dynamics of charge separation. For a detailed investigation bare CdSe QDs and CdSe QDs attached to  $MV^{2+}$  were used. An excitation wavelength of 400 nm was utilized. Figures 6.2 a and b represent the TA map for bare CdSe QDs and CdSe QDs attached to  $MV^{2+}$ . At 220 fs after excitation the two samples have the same spectral shape. However, the 1S excitonic bleach of the QD attached to  $MV^{2+}$  is red shifted relative to the bare CdSe (465 nm). After 220 fs the excitonic bleach of CdSe attached to  $MV^{2+}$  reduces and a broad positive absorption bleach at longer wavelengths (550-700 nm) appears (Figure 6.2 d). To track this bleach a zoom in of the first 2 ps is illustrated in Figure 6.2 b. Since the bare  $MV^{2+}$  does not show any TA dynamic signatures in the visible region (Figure 6.3), the broad absorption bleach at longer wavelengths (550-700 nm) can be related to the transport of the excited electron of CdSe QDs to  $MV^{2+}$ , generating  $MV^+$ .

---

<sup>1</sup>All TA measurements were performed with a wavelength of 400 nm and an excitation power of 100  $\mu W$ .

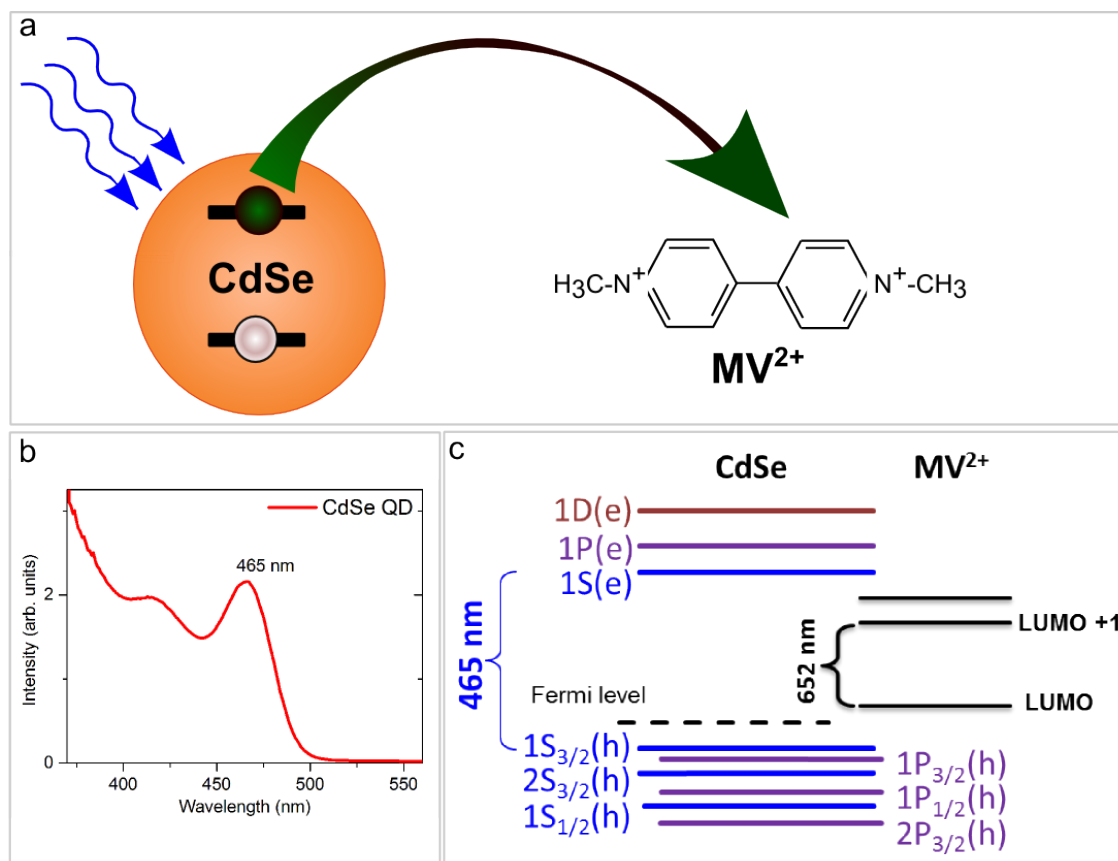


**Figure 6.1:** a) Schematic illustration of electron transport from CdSe QDs to methyl viologen ( $MV^{2+}$ ) molecule acceptor. b) Steady-state absorption of CdSe QDs with an effective diameter of 1.7 nm. c) Calculated band alignment of CdSe QDs attached to  $MV^{2+}$ .

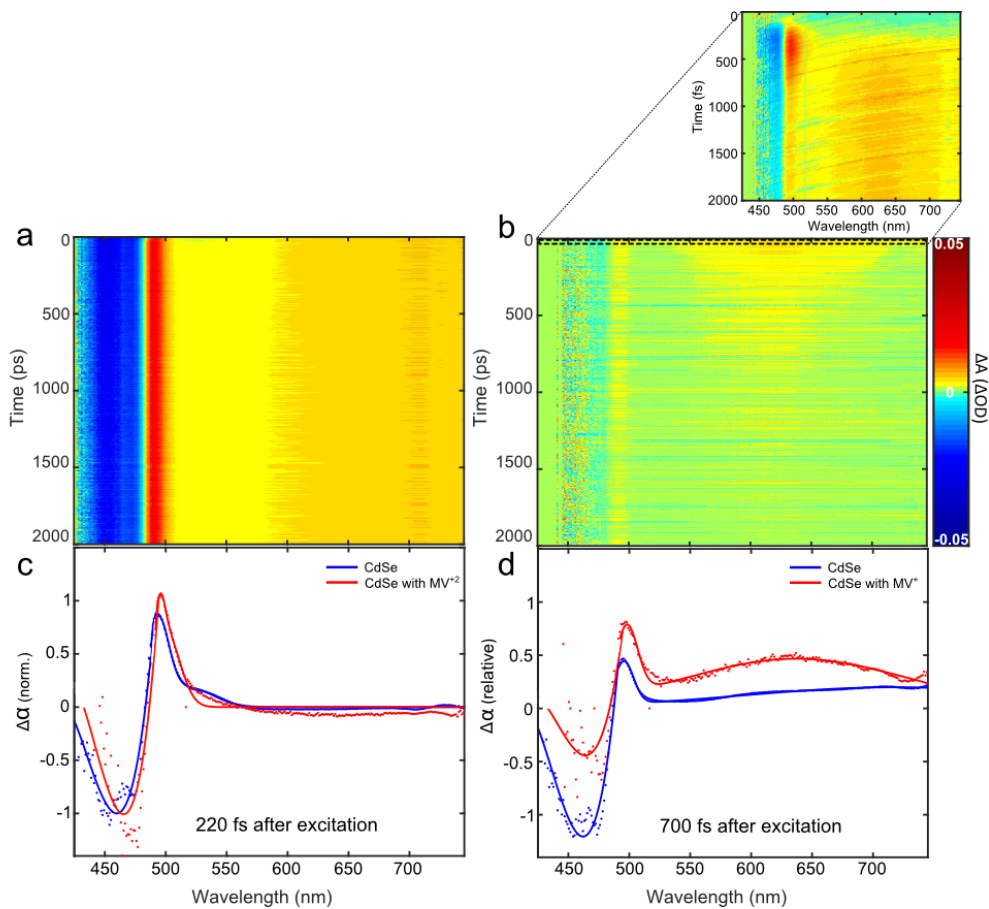


**Figure 6.2:** TA maps of (a) CdSe QDs and (b) CdSe QDs with  $MV^{2+}$ . Extracted TA spectra of CdSe QDs in blue and CdSe QDs with  $MV^{2+}$  in red at (c) 220 fs after excitation and (d) 700 fs after excitation. The spectra were normalized to the QD absorption bleach intensity at 220 fs.

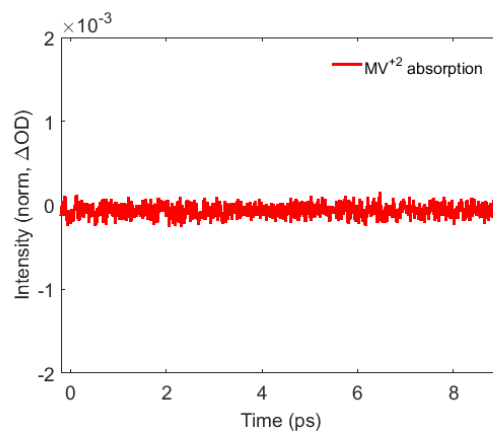


**Figure 6.3:** The bare  $MV^{2+}$  does not show any TA dynamic signatures in the visible region.

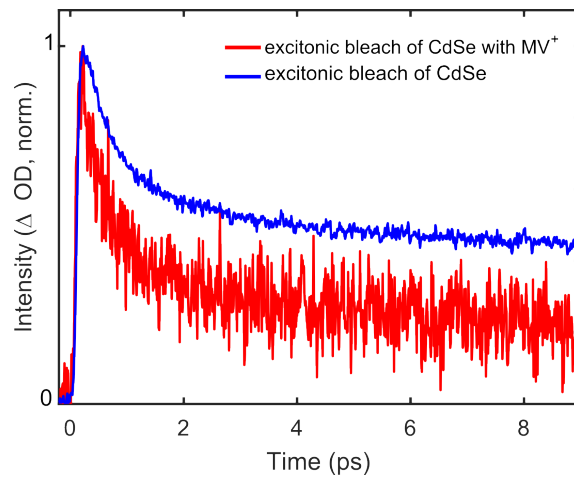


**Figure 6.4:** TA dynamics of the CdSe  $1S$  excitonic bleach for bare CdSe QDs (in blue) and CdSe QDs attached to  $MV^{2+}$  (in red).

The fastened decay dynamic of the CdSe  $1S$  excitonic bleach in CdSe QDs attached to  $MV^{2+}$  relative to the bare CdSe QDs (Figure 6.4), confirms a new nonradiative relaxation channel in CdSe QDs. This nonradiative process is associated with the electron transport from CdSe QDs to  $MV^{2+}$ . This allows a discussion of the dynamic of the charge transfer by comparing the QDs coupled to  $MV^{2+}$   $1S$  excitonic bleach dynamic and  $MV^{2+}$  dynamic.

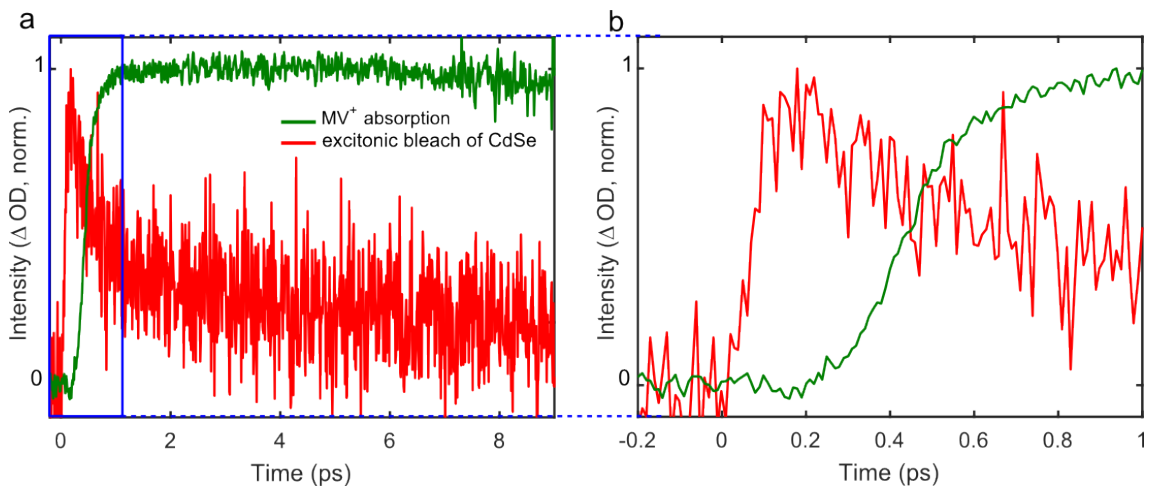


**Figure 6.5:** a) TA dynamics of the CdSe  $1S$  excitonic bleach and the  $MV^{2+}$  bleach extracted from CdSe QDs attached to  $MV^{2+}$ . b) A zoom into the the first 1 ps after excitation.

Figure 6.5 represent the traces of the TA dynamics of the CdSe QDs  $1S$  excitonic bleach attached to  $MV^{2+}$  and the TA bleach dynamic of the broad  $MV^{2+}$ . [176] The carrier relaxation in CdSe happens very fast. After about 400 fs the  $MV^{2+}$  bleach is still rising while the CdSe  $1S$  excitonic bleach is relaxing. These data indicate a duration of charge transport

about 400 fs from CdSe QDs to  $MV^{2+}$ .

### 6.1.2 Photoluminescence of CdSe QDs coupled to Methyl Viologen

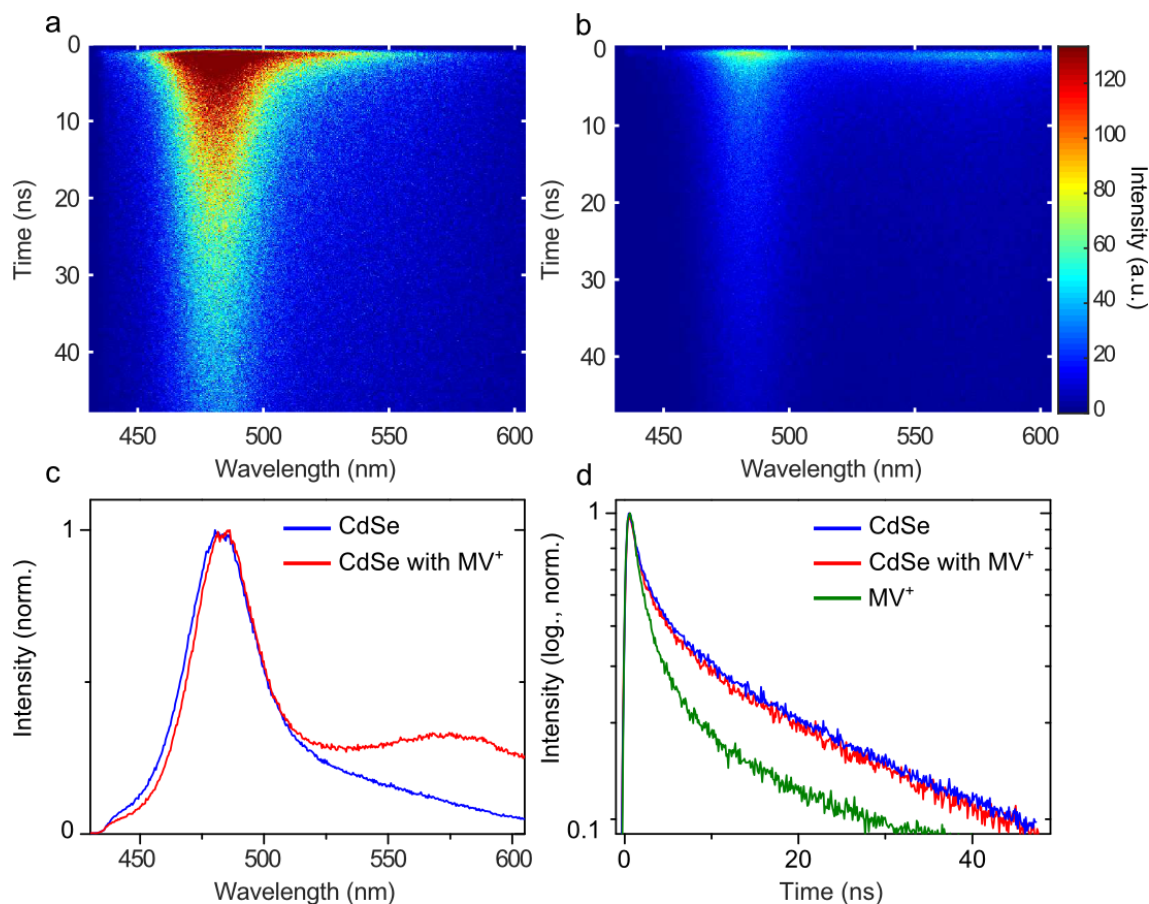


**Figure 6.6:** PL streak camera map for a) bare CdSe QDs and b) CdSe QDs attached to  $MV^{2+}$ . c) The extracted PL spectra of both samples are normalized to the maximum intensity. d) Extracted PL decay of the  $1S$  excitonic state for bare CdSe QDs and CdSe QDs attached to  $MV^{2+}$  compared to the  $MV^{+}$  PL.

In the ns regime, more information can be collected through the PL behavior of this system. Figure 6.6 a and b represent time and spectral resolved PL streak camera maps of CdSe QDs and CdSe QDs attached to  $MV^{2+}$ . The PL intensity of the  $1S$  excitonic state decreases by attaching the QDs to  $MV^{2+}$  and a broad PL at longer wavelengths (550-600 nm) appears. This broad feature has a faster PL decay than the CdSe QDs decay of both systems (at 465 nm)(Figure 6.6 d). Since this broad PL does not appear for the bare CdSe QDs, one can relate it to the  $MV^{+}$ . Though  $MV^{+}$  does not show any fluorescence behavior. The energy difference between the LUMO band of  $MV^{2+}$  and the VB (ground

state) of CdSe QDs in the calculated band alignment in Figure 6.1 is appropriate to the broad PL in Figure 6.6 b. The electron in  $MV^{2+}$  can be relaxed into the LUMO band and transported to the VB (ground state) of CdSe QDs.

## 7 Summary

The strain at the interface between the core and shell remains an issue and can still be a source for trap states. Using Raman spectroscopy, the strain in core/shell QDs was investigated by studying the LO phonon frequency behavior of core/shell QDs. As model material, InP/ZnSe core/shell QDs with different shell thickness were used. By increasing the thickness of the shell layer, a frequency shift of the core-related LO phonons towards higher frequencies was observed. The reason for this is due to the different lattice constants of InP (5.86 Å) and ZnSe (5.68 Å): InP QDs are compressed by the lattice reconstruction with the ZnSe shell.

To overcome any compressive or tensile strain, the shell was synthesized as an alloy from different compositions of ZnSe and CdSe. Since bulk CdSe was a larger lattice constant than InP (6.08 Å), a strain-free shell alloy could be achieved with a composition of  $\text{Zn}_{0.58}\text{Cd}_{0.42}$ . A systematic shift of the shell-related LO phonons was demonstrated and the strain in the interface could be tuned from compressive to tensile. A linear dependence of the strain and the lattice mismatch between the core and the shell material was observed. Thus, an engineering of the alloys' composition while tracking the LO phonon frequency allows an optimization of the emission properties of the NCs.

In order to achieve water-soluble semiconductor NCs, the NCs were encapsulated using block-copolymers. Clusters of encapsulated QDs/QRs were shown to be stable optically, which could be confirmed by power-dependent measurements (without any blinking behavior). The distances between the QDs/QRs in micelles were tuned by exchanging their ligands. The size of the micelles could be controlled by the copolymers' weight, while the distance between the QDs/QRs was controlled by the weight of the ligand. It could be shown, that in these systems Förster Energy transfer along with Auger processes are two important non-radiative recombination channels. Using SAXS data and comparing the PL decay-time constants of single particles with clusters, the effective distance between the particles could be estimated.

At higher excitation conditions (corresponding to an exciton population of 1 per particle), a coupling between FRET and Auger recombination could be observed. The FRET from blue to red NCs induces multiexcitons in the red NCs, which is followed by a nonradiative Auger recombination process. This effect leads to a fast recombination of the triggered

multiexcitons in the red NCs, which also led to a reduction in the radiative efficiency of the NCs. This effect depends on the distance between the QDs/QRs in the micelles and the excitation power. In order to increase the efficiency of compact light source devices, one should be aware of this effect and avoid the generation of triggered multiexcitons. As a model system to investigate the dynamics of charge separation for applications such as solar cells, QDs coupled to electron accepting molecules have been used. Using time-resolved transient absorption spectroscopy, the electron transfer from a photo-excited QD to Methyl Viologen was studied. The duration of the electron transfer was estimated to be around 400 fs. Other processes such as biexcitons with a dynamic of  $\sim 730$  fs could be observed. The discussed issues in this thesis will help with the optimization of the structural and optical properties of the NCs in order to use them for bioimaging, light source devices and solar cells.

## 8 Bibliography

- [1] Sandeep Kumar and Thomas Nann. Shape control of II–VI semiconductor nanomaterials. *Small*, 2(3):316–329, 2006.
- [2] N. Tessler. Efficient near-infrared polymer nanocrystal light-emitting diodes. *Science*, 295(5559):1506–1508, 2002.
- [3] Hao Huang, August Dorn, Vladimir Bulovic, and Mounqi G. Bawendi. Electrically driven light emission from single colloidal quantum dots at room temperature. *Applied Physics Letters*, 90(2):023110(1–3), 2007.
- [4] Benjamin S. Mashford, Matthew Stevenson, Zoran Popovic, Charles Hamilton, Zhaoqun Zhou, Craig Breen, Jonathan Steckel, Vladimir Bulovic, Mounqi Bawendi, Seth Coe-Sullivan, and Peter T. Kazlas. High-efficiency quantum-dot light-emitting devices with enhanced charge injection. *Nature Photonics*, 7(5):407–412, 2013.
- [5] K. Roy Choudhury, Y. Sahoo, T. Y. Ohulchanskyy, and P. N. Prasad. Efficient photoconductive devices at infrared wavelengths using quantum dot-polymer nanocomposites. *Applied Physics Letters*, 87(7):073110(1–3), 2005.
- [6] Nir Yaacobi-Gross, Michal Soreni-Harari, Marina Zimin, Shifi Kababya, Asher Schmidt, and Nir Tessler. Molecular control of quantum-dot internal electric field and its application to CdSe-based solar cells. *Nature Materials*, 10(12):974–979, 2011.
- [7] M. C. Schlamp, Xiaogang Peng, and A. P. Alivisatos. Improved efficiencies in light emitting diodes made with CdSe(CdS) core/shell type nanocrystals and a semiconducting polymer. *Journal of Applied Physics*, 82(11):5837–5842, 1997.
- [8] Mingjian Yuan, Li Na Quan, Riccardo Comin, Grant Walters, Randy Sabatini, Oleksandr Voznyy, Sjoerd Hoogland, Yongbiao Zhao, Eric M. Beaugard, Pongsakorn Kanjanaboos, Zhenghong Lu, Dong Ha Kim, and Edward H. Sargent. Perovskite energy funnels for efficient light-emitting diodes. *Nature Nanotechnology*, 11(10):872–877, 2016.
- [9] Zhengguo Xiao, Ross A. Kerner, Lianfeng Zhao, Nhu L. Tran, Kyung Min Lee, Tae-Wook Koh, Gregory D. Scholes, and Barry P. Rand. Efficient perovskite light-

- emitting diodes featuring nanometre-sized crystallites. *Nature Photonics*, 11(2):108–115, 2017.
- [10] A.F.E. Hezinger, J. Teßmar, and A. Göpferich. Polymer coating of quantum dots a powerful tool toward diagnostics and sensorics. *European Journal of Pharmaceutics and Biopharmaceutics*, 68(1):138–152, 2008.
- [11] Jinho Park, Mi Kyung Yu, Yong Yeon Jeong, Jin Woong Kim, Kwangyeol Lee, Vu Ngoc Phan, and Sangyong Jon. Antibiofouling amphiphilic polymer-coated superparamagnetic iron oxide nanoparticles: synthesis, characterization, and use in cancer imaging in vivo. *Journal of Materials Chemistry*, 19(35):6412–6417, 2009.
- [12] Giovanni Morello, Marco Anni, Pantaleo Davide Cozzoli, Liberato Manna, Roberto Cingolani, and Milena De Giorgi. Picosecond photoluminescence decay time in colloidal nanocrystals: the role of intrinsic and surface states. *The Journal of Physical Chemistry C*, 111(28):10541–10545, 2007.
- [13] M. G. Bawendi, P. J. Carroll, William L. Wilson, and L. E. Brus. Luminescence properties of CdSe quantum crystallites: Resonance between interior and surface localized states. *The Journal of Chemical Physics*, 96(2):946–954, 1992.
- [14] Alicia W. Cohn, Alina M. Schimpf, Carolyn E. Gunthardt, and Daniel R. Gamelin. Size-dependent trap-assisted auger recombination in semiconductor nanocrystals. *Nano Letters*, 13(4):1810–1815, 2013.
- [15] Marco Califano. Photoinduced surface trapping and the observed carrier multiplication yields in static CdSe nanocrystal samples. *ACS Nano*, 5(5):3614–3621, 2011.
- [16] Kaifeng Wu, Young-Shin Park, Jaehoon Lim, and Victor I. Klimov. Towards zero-threshold optical gain using charged semiconductor quantum dots. *Nature Nanotechnology*, 12(12):1140–1147, 2017.
- [17] Andrew M. Smith and Shuming Nie. Semiconductor nanocrystals: Structure, properties, and band gap engineering. *Accounts of Chemical Research*, 43(2):190–200, 2010.
- [18] Claudia Pigliacelli, Daniele Maiolo, Nonappa, Johannes S. Haataja, Heinz Amenitsch, Claire Michelet, Paola Sánchez Moreno, Ilaria Tirota, Pierangelo Mertrangolo, and Francesca Baldelli Bombelli. Efficient encapsulation of fluorinated drugs in the confined space of water-dispersible fluorinated supraparticles. *Angewandte Chemie International Edition*, 56(51):16186–16190, 2017.

- 
- [19] Hongwei Chen, Julie Yeh, Liya Wang, Hafsa Khurshid, Nan Peng, Andrew Y. Wang, and Hui Mao. Preparation and control of the formation of single core and clustered nanoparticles for biomedical applications using a versatile amphiphilic diblock copolymer. *Nano Research*, 3(12):852–862, 2010.
- [20] H. Ai, C. Flask, B. Weinberg, X.-T. Shuai, M. D. Pagel, D. Farrell, J. Duerk, and J. Gao. Magnetite-loaded polymeric micelles as ultrasensitive magnetic-resonance probes. *Advanced Materials*, 17(16):1949–1952, 2005.
- [21] Norased Nasongkla, Erik Bey, Jimin Ren, Hua Ai, Chalermchai Khemtong, Jagadeesh Setti Guthi, Shook-Fong Chin, A. Dean Sherry, David A. Boothman, and Jinming Gao. Multifunctional polymeric micelles as cancer-targeted, MRI-ultrasensitive drug delivery systems. *Nano Letters*, 6(11):2427–2430, 2006.
- [22] Byeong-Su Kim and T. Andrew Taton. Multicomponent nanoparticles via self-assembly with cross-linked block copolymer surfactants. *Langmuir*, 23(4):2198–2202, 2007.
- [23] Byeong-Su Kim, Jiao-Ming Qiu, Jian-Ping Wang, and T. Andrew Taton. Magnetomicelles: Composite nanostructures from magnetic nanoparticles and cross-linked amphiphilic block copolymers. *Nano Letters*, 5(10):1987–1991, 2005.
- [24] Larken E. Euliss, Stephanie G. Grancharov, Stephen O'Brien, Timothy J. Deming, Galen D. Stucky, C. B. Murray, and G. A. Held. Cooperative assembly of magnetic nanoparticles and block copolypeptides in aqueous media. *Nano Letters*, 3(11):1489–1493, 2003.
- [25] Charles Kittel. *Introduction to Solid State Physics*. John Wiley and Sons Ltd, 2004.
- [26] Peter Y. Yu and Manuel Cardona. *Fundamentals of Semiconductors*. Springer Berlin Heidelberg, 2010.
- [27] Claus F. Klingshirn. *Semiconductor Optics*. Springer Berlin Heidelberg, 2012.
- [28] Carlo Jacoboni. *Theory of Electron Transport in Semiconductors*. Springer Berlin Heidelberg, 2010.
- [29] Alexandra Szemjonov, Thierry Pauporté, Ilaria Ciofini, and Frédéric Labat. Investigation of the bulk and surface properties of cdse: insights from theory. *Physical Chemistry Chemical Physics*, 16(42):23251–23259, 2014.
- [30] D. J. Norris, Al. L. Efros, M. Rosen, and M. G. Bawendi. Size dependence of exciton fine structure in CdSe quantum dots. *Physical Review B*, 53(24):16347–16354, 1996.

- [31] A.I. Ekimov, Al.L. Efros, and A.A. Onushchenko. Quantum size effect in semiconductor microcrystals. *Solid State Communications*, 56(11):921–924, 1985.
- [32] A. D. Yoffe. Low-dimensional systems: Quantum size effects and electronic properties of semiconductor microcrystallites (zero-dimensional systems) and some quasi-two-dimensional systems. *Advances in Physics*, 51(2):799–890, 2002.
- [33] L. E. Brus. Electron–electron and electron-hole interactions in small semiconductor crystallites: The size dependence of the lowest excited electronic state. *The Journal of Chemical Physics*, 80(9):4403–4409, 1984.
- [34] Victor I. Klimov. Spectral and dynamical properties of multiexcitons in semiconductor nanocrystals. *Annual Review of Physical Chemistry*, 58(1):635–673, 2007.
- [35] R. Rossetti, J. L. Ellison, J. M. Gibson, and L. E. Brus. Size effects in the excited electronic states of small colloidal CdS crystallites. *The Journal of Chemical Physics*, 80(9):4464–4469, 1984.
- [36] Louis Brus. Electronic wave functions in semiconductor clusters: experiment and theory. *The Journal of Physical Chemistry*, 90(12):2555–2560, 1986.
- [37] Victor K LaMer and Robert H Dinegar. Theory, production and mechanism of formation of monodispersed hydrosols. *Journal of the American Chemical Society*, 72(11):4847–4854, 1950.
- [38] Ranjani Viswanatha and Dipankar Das Sarma. Growth of nanocrystals in solution. *Nanomaterials chemistry: recent developments and new directions*, pages 139–170, 2007.
- [39] Neus G. Bastus, Joan Comenge, and Victor Puntes. Kinetically controlled seeded growth synthesis of citrate-stabilized gold nanoparticles of up to 200 nm: Size focusing versus ostwald ripening. *Langmuir*, 27(17):11098–11105, 2011.
- [40] C. B. Murray, D. J. Norris, and M. G. Bawendi. Synthesis and characterization of nearly monodisperse CdE (e = sulfur, selenium, tellurium) semiconductor nanocrystallites. *Journal of the American Chemical Society*, 115(19):8706–8715, 1993.
- [41] Mona Rafipoor, Dorian Dupont, Hans Tornatzky, Mickael D. Tessier, Janina Maultzsch, Zeger Hens, and Holger Lange. Strain engineering in InP/(Zn,Cd)Se core/shell quantum dots. *Chemistry of Materials*, 30(3):4393–4400, 2018.
- [42] Jelena Dimitrijevic, Lisa Krapf, Christopher Wolter, Christian Schmidtke, Jan-Philip Merkl, Tobias Jochum, Andreas Kornowski, Anna Schüth, Andreas Gebert,

- Gereon Hüttmann, Tobias Vossmeier, and Horst Weller. CdSe/CdS-quantum rods: fluorescent probes for in vivo two-photon laser scanning microscopy. *Nanoscale*, 6(17):10413–10422, 2014.
- [43] Mona Rafipoor, Christian Schmidtke, Christopher Wolter, Christian Strelow, Horst Weller, and Holger Lange. Clustering of CdSe/CdS quantum dot/quantum rods into micelles can form bright, non-blinking, stable, and biocompatible probes. *Langmuir*, 31(34):9441–9447, 2015.
- [44] Christian Würth, Daniel Geißler, and Ute Resch-Genger. Quantification of anisotropy-related uncertainties in relative photoluminescence quantum yield measurements of nanomaterials – semiconductor quantum dots and rods. *Zeitschrift für Physikalische Chemie*, 229(1-2), 2015.
- [45] D. Geißler, C. Würth, C. Wolter, H. Weller, and U. Resch-Genger. Excitation wavelength dependence of the photoluminescence quantum yield and decay behavior of CdSe/CdS quantum dot/quantum rods with different aspect ratios. *Physical Chemistry Chemical Physics*, 19(19):12509–12516, 2017.
- [46] Peter Reiss, Myriam Protiere, and Liang Li. Core/shell semiconductor nanocrystals. *small*, 5(2):154–168, 2009.
- [47] Marco Cirillo, Tangi Aubert, Raquel Gomes, Rik Van Deun, Philippe Emplit, Amelie Biermann, Holger Lange, Christian Thomsen, Edouard Brainin, and Zeger Hens. “flash” synthesis of CdSe/CdS core-shell quantum dots. *Chemistry of Materials*, 26(2):1154–1160, 2014.
- [48] Xiaogang Peng, Michael C. Schlamp, Andreas V. Kadavanich, and A. P. Alivisatos. Epitaxial growth of highly luminescent CdSe/CdS core/shell nanocrystals with photostability and electronic accessibility. *Journal of the American Chemical Society*, 119(30):7019–7029, 1997.
- [49] J. Jack Li, Y. Andrew Wang, Wenzhuo Guo, Joel C. Keay, Tetsuya D. Mishima, Matthew B. Johnson, and Xiaogang Peng. Large-scale synthesis of nearly monodisperse CdSe/CdS core/shell nanocrystals using air-stable reagents via successive ion layer adsorption and reaction. *Journal of the American Chemical Society*, 125(41):12567–12575, 2003.
- [50] Sergei A. Ivanov, Andrei Piryatinski, Jagjit Nanda, Sergei Tretiak, Kevin R. Zavadil, William O. Wallace, Don Werder, and Victor I. Klimov. Type-II core/shell CdS/ZnSe nanocrystals: Synthesis, electronic structures, and spectroscopic properties. *Journal of the American Chemical Society*, 129(38):11708–11719, 2007.

- [51] Luigi Carbone, Concetta Nobile, Milena De Giorgi, Fabio Della Sala, Giovanni Morello, Pierpaolo Pompa, Martin Hytch, Etienne Snoeck, Angela Fiore, Isabella R. Franchini, Monica Nadasan, Albert F. Silvestre, Letizia Chiodo, Stefan Kudera, Roberto Cingolani, Roman Krahne, and Liberato Manna. Synthesis and micrometer-scale assembly of colloidal CdSe/CdS nanorods prepared by a seeded growth approach. *Nano Letters*, 7(10):2942–2950, 2007.
- [52] Ke Gong and David F Kelley. A predictive model of shell morphology in CdSe/CdS core/shell quantum dots. *The Journal of chemical physics*, 141(19):053106(1–4), 2014.
- [53] Xiaobo Chen, Yongbing Lou, Anna C Samia, and Clemens Burda. Coherency strain effects on the optical response of core/shell heteronanostructures. *Nano Letters*, 3(6):799–803, 2003.
- [54] Ke Gong and David F Kelley. Lattice strain limit for uniform shell deposition in zincblende CdSe/CdS quantum dots. *The journal of physical chemistry letters*, 6(9):1559–1562, 2015.
- [55] Dmitri V. Talapin, Ivo Mekis, Stephan Götzinger, Andreas Kornowski, Oliver Benson, and Horst Weller. CdSe/CdS/ZnS and CdSe/ZnSe/ZnS core-shell-shell nanocrystals. *The Journal of Physical Chemistry B*, 108(49):18826–18831, 2004.
- [56] Sasanka Deka, Alessandra Quarta, Maria Grazia Lupo, Andrea Falqui, Simona Boninelli, Cinzia Giannini, Giovanni Morello, Milena De Giorgi, Guglielmo Lanzani, Corrado Spinella, Roberto Cingolani, Teresa Pellegrino, and Liberato Manna. CdSe/CdS/ZnS double shell nanorods with high photoluminescence efficiency and their exploitation as biolabeling probes. *Journal of the American Chemical Society*, 131(8):2948–2958, 2009.
- [57] Benard Omogo, Feng Gao, Pooja Bajwa, Mizuho Kaneko, and Colin D. Heyes. Reducing blinking in small core–multishell quantum dots by carefully balancing confinement potential and induced lattice strain: The "goldilocks" effect. *ACS Nano*, 10(4):4072–4082, 2016.
- [58] Tangi Aubert, Marco Cirillo, Stijn Flamee, Rik Van Deun, Holger Lange, Christian Thomsen, and Zeger Hens. Homogeneously alloyed CdSe<sub>1-x</sub>S<sub>x</sub> quantum dots ( $0 \leq x \leq 1$ ): An efficient synthesis for full optical tunability. *Chemistry of Materials*, 25(12):2388–2390, 2013.
- [59] Taehoon Kim, Sung Woo Kim, Meejae Kang, and Sang-Wook Kim. Large-scale synthesis of InPZnS alloy quantum dots with dodecanethiol as a composition controller. *The Journal of Physical Chemistry Letters*, 3(2):214–218, 2012.

- 
- [60] Francesca Pietra, Luca De Trizio, Anne W. Hoekstra, Nicolas Renaud, Mirko Prato, Ferdinand C. Grozema, Patrick J. Baesjou, Rolf Koole, Liberato Manna, and Arjan J. Houtepen. Tuning the lattice parameter of  $\text{In}_x\text{Zn}_y\text{P}$  for highly luminescent lattice-matched core/shell quantum dots. *ACS Nano*, 10(4):4754–4762, 2016.
- [61] A. R. Denton and N. W. Ashcroft. Vegard’s law. *Physical Review A*, 43(6):3161–3164, 1991.
- [62] L. Vegard. Die konstitution der mischkristalle und die raumfüllung der atome. *Zeitschrift für Physik*, 5(1):17–26, 1921.
- [63] K Bouamama, P Djemia, N Lebga, and K Kassali. Ab initio calculation of the elastic properties and the lattice dynamics of the  $\text{Zn}_x\text{Cd}_{1-x}\text{Se}$  alloy. *Semiconductor Science and Technology*, 24(4):045005(1–5), 2009.
- [64] M Bouroushian, T Kosanovic, H Y Xu, and D Papadimitriou. Structural and optical investigation of electrosynthesized  $\text{Zn}_x\text{Cd}_{1-x}\text{Se}$  thin films. *Journal of Physics D: Applied Physics*, 38(10):1540–1545, 2005.
- [65] B. Dubertret. In vivo imaging of quantum dots encapsulated in phospholipid micelles. *Science*, 298(5599):1759–1762, 2002.
- [66] Teresa Pellegrino, Liberato Manna, Stefan Kudera, Tim Liedl, Dmitry Koktysh, Andrey L. Rogach, Simon Keller, Joachim Rädler, Giovanni Natile, and Wolfgang J. Parak. Hydrophobic nanocrystals coated with an amphiphilic polymer shell: a general route to water soluble nanocrystals. *Nano Letters*, 4(4):703–707, 2004.
- [67] Youngjong Kang and T. Andrew Taton. Core/shell gold nanoparticles by self-assembly and crosslinking of micellar, block-copolymer shells. *Angewandte Chemie International Edition*, 44(3):409–412, 2005.
- [68] Yuji Shibasaki, Byeong-Su Kim, Alexi J. Young, Anna L. McLoon, Stephen C. Ekker, and T. Andrew Taton. Crosslinked, glassy styrenic surfactants stabilize quantum dots against environmental extremes. *Journal of Materials Chemistry*, 19(35), 2009.
- [69] Chih-Wei Wang, Ali Oskoei, David Sinton, and Matthew G. Moffitt. Controlled self-assembly of quantum dot-block copolymer colloids in multiphase microfluidic reactors. *Langmuir*, 26(2):716–723, 2010.
- [70] Brenda L. Sanchez-Gaytan, Weihong Cui, YooJin Kim, Miguel A. Mendez-Polanco, Timothy V. Duncan, Michael Fryd, Bradford B. Wayland, and So-Jung Park. Interfacial assembly of nanoparticles in discrete block-copolymer aggregates. *Angewandte Chemie*, 119(48):9395–9398, 2007.

- [71] Robert J. Hickey, Alyssa S. Haynes, James M. Kikkawa, and So-Jung Park. Controlling the self-assembly structure of magnetic nanoparticles and amphiphilic block-copolymers: From micelles to vesicles. *Journal of the American Chemical Society*, 133(5):1517–1525, 2011.
- [72] Nicolas Duxin, Futian Liu, Hojatollah Vali, and Adi Eisenberg. Cadmium sulphide quantum dots in morphologically tunable triblock copolymer aggregates. *Journal of the American Chemical Society*, 127(28):10063–10069, 2005.
- [73] Weikun Li, Shanqin Liu, Renhua Deng, Jianying Wang, Zhihong Nie, and Jintao Zhu. A simple route to improve inorganic nanoparticles loading efficiency in block copolymer micelles. *Macromolecules*, 46(6):2282–2291, 2013.
- [74] Christian Schmidtke, Robin Eggers, Robert Zierold, Artur Feld, Hauke Kloust, Christopher Wolter, Johannes Ostermann, Jan-Philip Merkl, Theo Schotten, Cornelius Nielsch, and Horst Weller. Polymer-assisted self-assembly of superparamagnetic iron oxide nanoparticles into well-defined clusters: Controlling the collective magnetic properties. *Langmuir*, 30(37):11190–11196, 2014.
- [75] Christian Schmidtke, Elmar Pösel, Johannes Ostermann, Andrea Pietsch, Hauke Kloust, Huong Tran, Theo Schotten, Neus G Bastús, Robin Eggers, and Horst Weller. Amphiphilic, cross-linkable diblock copolymers for multifunctionalized nanoparticles as biological probes. *Nanoscale*, 5(16):7433–7444, 2013.
- [76] Dustin W. Shipp, Faris Sinjab, and Ioan Notingher. Raman spectroscopy: techniques and applications in the life sciences. *Advances in Optics and Photonics*, 9(2):315, 2017.
- [77] A. G. Rolo and M. I. Vasilevskiy. Raman spectroscopy of optical phonons confined in semiconductor quantum dots and nanocrystals. *Journal of Raman Spectroscopy*, 38(6):618–633, 2007.
- [78] M. J. Seong, Olga I. Mičić, A. J. Nozik, A. Mascarenhas, and Hyeonsik M. Cheong. Size-dependent raman study of InP quantum dots. *Applied Physics Letters*, 82(2):185–187, 2003.
- [79] D. L. Peterson, A. Petrou, W. Girit, A. K. Ramdas, and S. Rodriguez. Raman scattering from the vibrational modes in zn1-xmxte. *Physical Review B*, 33(2):1160–1165, 1986.
- [80] C X Shan, Z Liu, X T Zhang, C C Wong, and S K Hark. Wurtzite ZnSe nanowires: growth, photoluminescence, and single-wire raman properties. *Nanotechnology*, 17(22):5561–5564, 2006.

- 
- [81] V. Zannier, T. Cremel, A. Artioli, D. Ferrand, K. Kheng, V. Grillo, and S. Rubini. Optical properties of single wurtzite/zinc-blende ZnSe nanowires grown at low temperature. *Journal of Applied Physics*, 118(9):095702(1–6), 2015.
- [82] Jiaming Zhang, Xuke Zhang, and J. Y. Zhang. Dependence of microstructure and luminescence on shell layers in colloidal CdSe/CdS core/shell nanocrystals. *The Journal of Physical Chemistry C*, 114(9):3904–3908, 2010.
- [83] V M Dzhagan, M Ya Valakh, O E Raevska, O L Stroyuk, S Ya Kuchmiy, and D R T Zahn. The influence of shell parameters on phonons in core–shell nanoparticles: a resonant raman study. *Nanotechnology*, 20(36):365704(1–6), 2009.
- [84] Norman Tschirner, Holger Lange, Andrei Schliwa, Amelie Biermann, Christian Thomsen, Karel Lambert, Raquel Gomes, and Zeger Hens. Interfacial alloying in CdSe/CdS heteronanocrystals: A raman spectroscopy analysis. *Chemistry of Materials*, 24(2):311–318, 2012.
- [85] K. Försterling. Spezifische wärme und zustandsgleichung von kristallen. *Annalen der Physik*, 366(6):549–576, 1920.
- [86] F. Drucker, E. Grüneisen, F. Henning, Ph. Kohnstamm, and F. Körber. *Thermische Eigenschaften der Stoffe*. Springer Berlin Heidelberg, 1926.
- [87] Manuel Cardona, editor. *Light Scattering in Solids*. Springer Berlin Heidelberg, 1975.
- [88] A. P. Alivisatos, T. D. Harris, L. E. Brus, and A. Jayaraman. Resonance raman scattering and optical absorption studies of CdSe microclusters at high pressure. *The Journal of Chemical Physics*, 89(10):5979–5982, 1988.
- [89] Gaetano Scamarcio, Mario Lugará, and Daniela Manno. Size-dependent lattice contraction in CdS<sub>1-x</sub>Se<sub>x</sub> nanocrystals embedded in glass observed by raman scattering. *Physical Review B*, 45(23):13792–13795, 1992.
- [90] M. Manceau, S. Vezzoli, Q. Glorieux, F. Pisanello, E. Giacobino, L. Carbone, M. De Vittorio, and A. Bramati. Effect of charging on CdSe/CdS dot-in-rods single-photon emission. *Physical Review B*, 90(3), 2014.
- [91] Benoit Mahler, Piernicola Spinicelli, Stéphanie Buil, Xavier Quelin, Jean-Pierre Hermier, and Benoit Dubertret. Towards non-blinking colloidal quantum dots. *Nature Materials*, 7(8):659–664, 2008.
- [92] Siying Wang, Claudia Querner, Tali Dadosh, Catherine H. Crouch, Dmitry S. Novikov, and Marija Drndic. Collective fluorescence enhancement in nanoparticle clusters. *Nature Communications*, 2(1), 2011.

- [93] Yongfen Chen, Javier Vela, Han Htoon, Joanna L. Casson, Donald J. Werder, David A. Bussian, Victor I. Klimov, and Jennifer A. Hollingsworth. “giant” multishell CdSe nanocrystal quantum dots with suppressed blinking. *Journal of the American Chemical Society*, 130(15):5026–5027, 2008.
- [94] Wolfgang Demtröder. *Laserspektroskopie 1*. Springer Berlin Heidelberg, 2011.
- [95] D.T. Nguyen, C. Voisin, Ph. Roussignol, C. Roquelet, J.S. Lauret, and G. Cassabois. Excitonic homogeneous broadening in single-wall carbon nanotubes. *Chemical Physics*, 413:102–111, 2013.
- [96] Jian Cui, Andrew P. Beyler, Igor Coropceanu, Liam Cleary, Thomas R. Avila, Yue Chen, José M. Cordero, S. Leigh Heathcote, Daniel K. Harris, Ou Chen, Jianshu Cao, and Mounqi G. Bawendi. Evolution of the single-nanocrystal photoluminescence linewidth with size and shell: Implications for exciton–phonon coupling and the optimization of spectral linewidths. *Nano Letters*, 16(1):289–296, 2015.
- [97] S. A. Empedocles, D. J. Norris, and M. G. Bawendi. Photoluminescence spectroscopy of single CdSe nanocrystallite quantum dots. *Physical Review Letters*, 77(18):3873–3876, 1996.
- [98] Inhee Chung and Mounqi G. Bawendi. Relationship between single quantum-dot intermittency and fluorescence intensity decays from collections of dots. *Physical Review B*, 70(16), 2004.
- [99] Germar Schlegel, Jolanta Bohnenberger, Inga Potapova, and Alf Mews. Fluorescence decay time of single semiconductor nanocrystals. *Physical Review Letters*, 88(13), 2002.
- [100] Ou Chen, Jing Zhao, Vikash P. Chauhan, Jian Cui, Cliff Wong, Daniel K. Harris, He Wei, Hee-Sun Han, Dai Fukumura, Rakesh K. Jain, and Mounqi G. Bawendi. Compact high-quality CdSe–CdS core–shell nanocrystals with narrow emission linewidths and suppressed blinking. *Nature Materials*, 12(5):445–451, 2013.
- [101] Marco Califano. Off-state quantum yields in the presence of surface trap states in cdse nanocrystals: The inadequacy of the charging model to explain blinking. *The Journal of Physical Chemistry C*, 115(37):18051–18054, 2011.
- [102] Marco Califano and Francisco M Gómez-Campos. Universal trapping mechanism in semiconductor nanocrystals. *Nano letters*, 13(5):2047–2052, 2013.
- [103] Simon C Boehme, Jon Mikel Azpiroz, Yaroslav V Aulin, Ferdinand C Grozema, Daniel Vanmaekelbergh, Laurens DA Siebbeles, Ivan Infante, and Arjan J Houtepen.

- Density of trap states and auger-mediated electron trapping in CdTe quantum-dot solids. *Nano letters*, 15(5):3056–3066, 2015.
- [104] Arjan J Houtepen, Zeger Hens, Jonathan S Owen, and Ivan Infante. On the origin of surface traps in colloidal ii–vi semiconductor nanocrystals. *Chemistry of Materials*, 29(2):752–761, 2017.
- [105] M. Kuno, D. P. Fromm, H. F. Hamann, A. Gallagher, and D. J. Nesbitt. Nonexponential "blinking" kinetics of single CdSe quantum dots: A universal power law behavior. *The Journal of Chemical Physics*, 112(7):3117–3120, 2000.
- [106] M. Kuno, D. P. Fromm, H. F. Hamann, A. Gallagher, and D. J. Nesbitt. "on"/"off" fluorescence intermittency of single semiconductor quantum dots. *The Journal of Chemical Physics*, 115(2):1028–1040, 2001.
- [107] Mauro Lomascolo, Arianna Creti, Gabriella Leo, Lorenzo Vasanelli, and Liberato Manna. Exciton relaxation processes in colloidal core/shell ZnSe/ZnS nanocrystals. *Applied Physics Letters*, 82(3):418–420, 2003.
- [108] A. V. Malko, A. A. Mikhailovsky, M. A. Petruska, J. A. Hollingsworth, and V. I. Klimov. Interplay between optical gain and photoinduced absorption in CdSe nanocrystals. *The Journal of Physical Chemistry B*, 108(17):5250–5255, 2004.
- [109] V. I. Klimov, A. A. Mikhailovsky, D. W. McBranch, C. A. Leatherdale, and M. G. Bawendi. Mechanisms for intraband energy relaxation in semiconductor quantum dots: The role of electron-hole interactions. *Physical Review B*, 61(20):R13349–R13352, 2000.
- [110] Victor I. Klimov and Duncan W. McBranch. Femtosecond 1p-to-1s electron relaxation in strongly confined semiconductor nanocrystals. *Physical Review Letters*, 80(18):4028–4031, 1998.
- [111] V. Klimov, S. Hunsche, and H. Kurz. Biexciton effects in femtosecond nonlinear transmission of semiconductor quantum dots. *Physical Review B*, 50(11):8110–8113, 1994.
- [112] Matthew Pelton, Sandrine Ithurria, Richard D. Schaller, Dmitriy S. Dolzhenkov, and Dmitri V. Talapin. Carrier cooling in colloidal quantum wells. *Nano Letters*, 12(12):6158–6163, 2012.
- [113] D. A. B. Miller, D. S. Chemla, T. C. Damen, A. C. Gossard, W. Wiegmann, T. H. Wood, and C. A. Burrus. Band-edge electroabsorption in quantum well structures: The quantum-confined stark effect. *Physical Review Letters*, 53(22):2173–2176, 1984.

- [114] Maria Grazia Lupo, Francesco Scotognella, Margherita Zavelani-Rossi, Guglielmo Lanzani, Liberato Manna, and Francesco Tassone. Band-edge ultrafast pump–probe spectroscopy of core/shell CdSe/CdS rods: assessing electron delocalization by effective mass calculations. *Physical Chemistry Chemical Physics*, 14(20):7420, 2012.
- [115] F.S. Manciù, R.E. Tallman, B.D. McCombe, B.A. Weinstein, D.W. Lucey, Y. Sahoo, and P.N. Prasad. Infrared and raman spectroscopies of InP/ii–vi core-shell nanoparticles. *Physica E: Low-dimensional Systems and Nanostructures*, 26(1-4):14–18, 2005.
- [116] E. G. Gadret, M. M. de Lima, J. R. Madureira, T. Chiaramonte, M. A. Cotta, F. Iikawa, and A. Cantarero. Optical phonon modes of wurtzite inp. *Applied Physics Letters*, 102(12):122101(1–4), 2013.
- [117] Ryan Gresback, Ryan Hue, Wayne L Gladfelter, and Uwe Kortshagen. Combined plasma gas-phase synthesis and colloidal processing of InP/ZnS core/shell nanocrystals. *Nanoscale Research Letters*, 6(1):68(1–6), 2011.
- [118] Liang Li and Peter Reiss. One-pot synthesis of highly luminescent InP/ZnS nanocrystals without precursor injection. *Journal of the American Chemical Society*, 130(35):11588–11589, 2008.
- [119] G. Chiarotti and P. Chiaradia, editors. *Physics of Solid Surfaces*. Springer Berlin Heidelberg, 2015.
- [120] Dorian Dupont, Mickael D. Tessier, Philippe F. Smet, and Zeger Hens. Indium phosphide-based quantum dots with shell-enhanced absorption for luminescent down-conversion. *Advanced Materials*, 29(29):170068(1–6), 2017.
- [121] L. A. Thi, N. D. Cong, N. T. Dang, N. X. Nghia, and V. X. Quang. Optical and phonon characterization of ternary CdSe<sub>x</sub>S<sub>1-x</sub> alloy quantum dots. *Journal of Electronic Materials*, 45(5):2621–2626, 2016.
- [122] Eunsoon Oh and A. K. Ramdas. Multi-mode behavior of optical phonons in II-VI ternary and quaternary alloys. *Journal of Electronic Materials*, 23(3):307–312, 1994.
- [123] H. Grille, Ch. Schnittler, and F. Bechstedt. Phonons in ternary group-III nitride alloys. *Physical Review B*, 61(9):6091–6105, 2000.
- [124] R. G. Alonso, E.-K. Suh, A. K. Ramdas, N. Samarth, H. Luo, and J. K. Furdyna. Raman spectroscopy of two novel semiconductors and related superlattices: Cubic Cd<sub>1-x</sub>Mn<sub>x</sub>Se and Cd<sub>1-x</sub>Zn<sub>x</sub>Se. *Physical Review B*, 40(6):3720–3728, 1989.

- 
- [125] Lalhriatzuala and Pratima Agarwal. Studies on spin orbit splitting and dual mode phonon vibrations in  $\text{ZnS}_x\text{Se}_{1-x}$  ternary alloys films with varying Se concentration. *Journal of Electronic Materials*, 44(10):3341–3353, 2015.
- [126] Bo Feng, Jian Cao, Donglai Han, Shuo Yang, and Jinghai Yang. Study on growth mechanism and optical properties of ZnSe nanoparticles. *Journal of Materials Science: Materials in Electronics*, 26(5):3206–3214, 2015.
- [127] Mohammed Ameri, Meriem Fodil, Fatma Z. Aoumeur-Benkabou, Zoubir Mahdjoub, Fatima Boufadi, and Ali Bentouaf. Physical properties of the  $\text{Zn}_x\text{Cd}_{1-x}\text{Se}$  alloys: Ab-initio method. *Materials Sciences and Applications*, 03(11):768–778, 2012.
- [128] A. Cavus, L. Zeng, B.X. Yang, N. Dai, M.C. Tamargo, N. Bambha, and F. Semendy. Optimized growth of lattice-matched ZnCdSe epilayers on InP substrates. *Journal of Crystal Growth*, 175-176:558–563, 1997.
- [129] Volkhard May. Kinetic theory of exciton–exciton annihilation. *The Journal of Chemical Physics*, 140(5):054103, 2014.
- [130] Clare E. Rowland, Igor Fedin, Hui Zhang, Stephen K. Gray, Alexander O. Govorov, Dmitri V. Talapin, and Richard D. Schaller. Picosecond energy transfer and multiexciton transfer outpaces auger recombination in binary CdSe nanoplatelet solids. *Nature Materials*, 14(5):484–489, 2015.
- [131] Th. Förster. Zwischenmolekulare Energiewanderung und Fluoreszenz. *Annalen der Physik*, 437(1-2), 1948.
- [132] Th. Förster. 10th Spiers Memorial Lecture. Transfer mechanisms of electronic excitation. *Discuss. Faraday Soc.*, 27(0), 1959.
- [133] Jacob B. Hoffman, Hyunbong Choi, and Prashant V. Kamat. Size-dependent energy transfer pathways in CdSe quantum dot–squaraine light-harvesting assemblies: Förster versus dexter. *The Journal of Physical Chemistry C*, 118(32):18453–18461, 2014.
- [134] Robert S. Knox. Förster’s resonance excitation transfer theory: not just a formula. *Journal of Biomedical Optics*, 17(1):011003, 2012.
- [135] S. A. Crooker, J. A. Hollingsworth, S. Tretiak, and V. I. Klimov. Spectrally resolved dynamics of energy transfer in quantum-dot assemblies: Towards engineered energy flows in artificial materials. *Physical Review Letters*, 89(18), 2002.

- [136] Marc Achermann, Melissa A. Petruska, Scott A. Crooker, and Victor I. Klimov. Picosecond energy transfer in quantum dot langmuir-blodgett nanoassemblies. *The Journal of Physical Chemistry B*, 107(50):13782–13787, 2003.
- [137] Franziska Fennel and Stefan Lochbrunner. Exciton-exciton annihilation in a disordered molecular system by direct and multistep förster transfer. *Physical Review B*, 92(14), 2015.
- [138] Shan Huang, Hangna Qiu, Qi Xiao, Chusheng Huang, Wei Su, and Baoqing Hu. A simple QD–FRET bioprobe for sensitive and specific detection of hepatitis b virus DNA. *Journal of Fluorescence*, 23(5):1089–1098, 2013.
- [139] Igor L. Medintz and Hedi Mattoussi. Quantum dot-based resonance energy transfer and its growing application in biology. *Phys. Chem. Chem. Phys.*, 11(1):17–45, 2009.
- [140] P.G. Wu and L. Brand. Resonance energy transfer: Methods and applications. *Analytical Biochemistry*, 218(1):1–13, 1994.
- [141] Š. Kos, M. Achermann, V. I. Klimov, and D. L. Smith. Different regimes of förster-type energy transfer between an epitaxial quantum well and a proximal monolayer of semiconductor nanocrystals. *Physical Review B*, 71(20), 2005.
- [142] Michael H. Stewart, Alan L. Huston, Amy M. Scott, Eunkeu Oh, W. Russ Algar, Jeffrey R. Deschamps, Kimihiro Susumu, Vaibhav Jain, Duane E. Prasuhn, Juan Blanco-Canosa, Philip E. Dawson, and Igor L. Medintz. Competition between förster resonance energy transfer and electron transfer in stoichiometrically assembled semiconductor quantum dot–fullerene conjugates. *ACS Nano*, 7(10):9489–9505, 2013.
- [143] Amit Sitt, Na’ama Even-Dar, Shira Halivni, Adam Faust, Lior Yedidya, and Uri Banin. Analysis of shape and dimensionality effects on fluorescence resonance energy transfer from nanocrystals to multiple acceptors. *The Journal of Physical Chemistry C*, 117(43):22186–22197, 2013.
- [144] Kaibo Zheng, Karel Žídek, Mohamed Abdellah, Nan Zhu, Pavel Chábera, Nils Lenngren, Qijin Chi, and Tõnu Pullerits. Directed energy transfer in films of CdSe quantum dots: Beyond the point dipole approximation. *Journal of the American Chemical Society*, 136(17):6259–6268, 2014.
- [145] Christopher J. Breshike, Ryan A. Riskowski, and Geoffrey F. Strouse. Leaving förster resonance energy transfer behind: Nanometal surface energy transfer predicts the size-enhanced energy coupling between a metal nanoparticle and an emitting dipole. *The Journal of Physical Chemistry C*, 117(45):23942–23949, 2013.

- 
- [146] Lars Dworak, Victor V. Matylitsky, Ting Ren, Thomas Basché, and Josef Wachtveitl. Acceptor concentration dependence of Förster resonance energy transfer dynamics in dye–quantum dot complexes. *The Journal of Physical Chemistry C*, 118(8):4396–4402, 2014.
- [147] Jelani Griffin, Anant Kumar Singh, Dulal Senapati, Patsy Rhodes, Kanieshia Mitchell, Brianica Robinson, Eugene Yu, and Paresh Chandra Ray. Size- and distance-dependent nanoparticle surface-energy transfer (NSET) method for selective sensing of hepatitis c virus RNA. *Chemistry - A European Journal*, 15(2):342–351, 2008.
- [148] Margaret Chern, Thuy T. Nguyen, Andrew H. Mahler, and Allison M. Dennis. Shell thickness effects on quantum dot brightness and energy transfer. *Nanoscale*, 9(42):16446–16458, 2017.
- [149] A. Paul Alivisatos, Weiwei Gu, and Carolyn Larabell. Quantum Dots as Cellular Probes. *Annual Review of Biomedical Engineering*, 7(1):55–76, 2005.
- [150] Kim Sapsford, Thomas Pons, Igor Medintz, and Hedi Mattoussi. Biosensing with luminescent semiconductor quantum dots. *Sensors*, 6(8):925–953, 2006.
- [151] Ron Gill, Itamar Willner, Itzhak Shweky, and Uri Banin. Fluorescence resonance energy transfer in CdSe/ZnS-DNA conjugates: probing hybridization and DNA cleavage. *The Journal of Physical Chemistry B*, 109(49):23715–23719, 2005.
- [152] I. L. Medintz, J. H. Koenig, A. R. Clapp, I. Stanish, M. E. Twigg, H. Mattoussi, J. M. Mauro, and J. R. Deschamps. A fluorescence resonance energy transfer-derived structure of a quantum dot-protein bioconjugate nanoassembly. *Proceedings of the National Academy of Sciences*, 101(26):9612–9617, 2004.
- [153] Aaron R. Clapp, Igor L. Medintz, J. Matthew Mauro, Brent R. Fisher, Mounji G. Bawendi, and Hedi Mattoussi. Fluorescence resonance energy transfer between quantum dot donors and dye-labeled protein acceptors. *Journal of the American Chemical Society*, 126(1):301–310, 2004.
- [154] Aaron R. Clapp, Igor L. Medintz, Brent R. Fisher, George P. Anderson, and Hedi Mattoussi. Can luminescent quantum dots be efficient energy acceptors with organic dye donors? *Journal of the American Chemical Society*, 127(4):1242–1250, 2005.
- [155] Ido Hadar, Shira Halivni, Na’ama Even-Dar, Adam Faust, and Uri Banin. Dimensionality effects on fluorescence resonance energy transfer between single semiconductor nanocrystals and multiple dye acceptors. *The Journal of Physical Chemistry C*, 119(7):3849–3856, 2015.

- [156] Pedro Ludwig Hernández-Martínez, Alexander O. Govorov, and Hilmi Volkan Demir. Generalized theory of förster-type nonradiative energy transfer in nanostructures with mixed dimensionality. *The Journal of Physical Chemistry C*, 117(19):10203–10212, 2013.
- [157] Young-Shin Park, Wan Ki Bae, Lazaro A. Padilha, Jeffrey M. Pietryga, and Victor I. Klimov. Effect of the core/shell interface on auger recombination evaluated by single-quantum-dot spectroscopy. *Nano Letters*, 14(2):396–402, 2014.
- [158] Haiming Zhu, Nianhui Song, William Rodríguez-Córdoba, and Tianquan Lian. Wave function engineering for efficient extraction of up to nineteen electrons from one CdSe/CdS quasi-type II quantum dot. *Journal of the American Chemical Society*, 134(9):4250–4257, 2012.
- [159] István Robel, Ryan Gresback, Uwe Kortshagen, Richard D. Schaller, and Victor I. Klimov. Universal size-dependent trend in auger recombination in direct-gap and indirect-gap semiconductor nanocrystals. *Physical Review Letters*, 102(17), 2009.
- [160] Sebastian Jander, Andreas Kornowski, and Horst Weller. Energy transfer from CdSe/CdS nanorods to amorphous carbon. *Nano Letters*, 11(12):5179–5183, 2011.
- [161] Shira Halivni, Amit Sitt, Ido Hadar, and Uri Banin. Effect of nanoparticle dimensionality on fluorescence resonance energy transfer in nanoparticle–dye conjugated systems. *ACS Nano*, 6(3):2758–2765, 2012.
- [162] R. R. Chance, A. Prock, and R. Silbey. Molecular fluorescence and energy transfer near interfaces. In *Advances in Chemical Physics*, pages 1–65. John Wiley & Sons, Inc., 2007.
- [163] V. I. Klimov. Quantization of multiparticle auger rates in semiconductor quantum dots. *Science*, 287(5455):1011–1013, 2000.
- [164] Victor I. Klimov. Optical nonlinearities and ultrafast carrier dynamics in semiconductor nanocrystals. *The Journal of Physical Chemistry B*, 104(26):6112–6123, 2000.
- [165] V. I. Klimov, D. W. McBranch, C. A. Leatherdale, and M. G. Bawendi. Electron and hole relaxation pathways in semiconductor quantum dots. *Physical Review B*, 60(19):13740–13749, 1999.
- [166] Alexander W. Schill, Christopher S. Gaddis, Wei Qian, Mostafa A. El-Sayed, Ye Cai, Valeria T. Milam, and Kenneth Sandhage. Ultrafast electronic relaxation and charge-carrier localization in CdS/CdSe/CdS quantum-dot quantum-well heterostructures. *Nano Letters*, 6(9):1940–1949, 2006.

- 
- [167] Iwan Moreels, Karel Lambert, David De Muynck, Frank Vanhaecke, Dirk Poelman, José C. Martins, Guy Allan, and Zeger Hens. Composition and size-dependent extinction coefficient of colloidal PbSe quantum dots. *Chemistry of Materials*, 19(25):6101–6106, 2007.
- [168] Michiel Aerts, Frank C. M. Spoor, Ferdinand C. Grozema, Arjan J. Houtepen, Juleon M. Schins, and Laurens D. A. Siebbeles. Cooling and auger recombination of charges in PbSe nanorods: Crossover from cubic to bimolecular decay. *Nano Letters*, 13(9):4380–4386, 2013.
- [169] Yunan Gao, C. S. Suchand Sandeep, Juleon M. Schins, Arjan J. Houtepen, and Laurens D. A. Siebbeles. Disorder strongly enhances auger recombination in conductive quantum-dot solids. *Nature Communications*, 4(1), 2013.
- [170] Haiming Zhu, Nianhui Song, and Tianquan Lian. Wave function engineering for ultrafast charge separation and slow charge recombination in type II core/shell quantum dots. *Journal of the American Chemical Society*, 133(22):8762–8771, 2011.
- [171] Jier Huang, Zhuangqun Huang, Ye Yang, Haiming Zhu, and Tianquan Lian. Multiple exciton dissociation in CdSe quantum dots by ultrafast electron transfer to adsorbed methylene blue. *Journal of the American Chemical Society*, 132(13):4858–4864, 2010.
- [172] Ya-Feng Wang, Hai-Yu Wang, Zheng-Shun Li, Jia Zhao, Lei Wang, Qi-Dai Chen, Wen-Quan Wang, and Hong-Bo Sun. Electron extraction dynamics in CdSe and CdSe/CdS/ZnS quantum dots adsorbed with methyl viologen. *The Journal of Physical Chemistry C*, 118(31):17240–17246, 2014.
- [173] Victor V. Matylitsky, Lars Dworak, Vladimir V. Breus, Thomas Basché, and Josef Wachtveitl. Ultrafast charge separation in multiexcited CdSe quantum dots mediated by adsorbed electron acceptors. *Journal of the American Chemical Society*, 131(7):2424–2425, 2009.
- [174] Byung-Ryool Hyun, A. C. Bartnik, Liangfeng Sun, Tobias Hanrath, and F. W. Wise. Control of electron transfer from lead-salt nanocrystals to tio<sub>2</sub>. *Nano Letters*, 11(5):2126–2132, 2011.
- [175] M. Chandra Sekhar and Anunay Samanta. Ultrafast transient absorption study of the nature of interaction between oppositely charged photoexcited CdTe quantum dots and cresyl violet. *The Journal of Physical Chemistry C*, 119(27):15661–15668, 2015.
- [176] Jorge Peon, Xin Tan, J. David Hoerner, Chungeng Xia, Yin Fei Luk, and Bern Kohler. Excited state dynamics of methyl viologen. ultrafast photoreduction in

- methanol and fluorescence in acetonitrile. *The Journal of Physical Chemistry A*, 105(24):5768–5777, 2001.
- [177] Tadashi Watanabe and Kenichi Honda. Measurement of the extinction coefficient of the methyl viologen cation radical and the efficiency of its formation by semiconductor photocatalysis. *The Journal of Physical Chemistry*, 86(14):2617–2619, 1982.
- [178] Hirotugu Shiraishi, George V. Buxton, and Nicholas D. Wood. Temperature dependence of the absorption spectrum of the methyl viologen cation radical and use of methyl viologen as a scavenger for estimating yields of the primary radicals in the radiolysis of high-temperature water. *International Journal of Radiation Applications and Instrumentation. Part C. Radiation Physics and Chemistry*, 33(6):519–522, 1989.
- [179] Victoria L. Bridewell, Rabeka Alam, Christopher J. Karwacki, and Prashant V. Kamat. CdSe/CdS nanorod photocatalysts: Tuning the interfacial charge transfer process through shell length. *Chemistry of Materials*, 27(14):5064–5071, 2015.
- [180] Peng Zeng, Nicholas Kirkwood, Paul Mulvaney, Klaus Boldt, and Trevor A. Smith. Shell effects on hole-coupled electron transfer dynamics from CdSe/CdS quantum dots to methyl viologen. *Nanoscale*, 8(19):10380–10387, 2016.
- [181] Joseph R. Lakowicz. *Principles of Fluorescence Spectroscopy*. Springer-Verlag New York Inc., 2006.
- [182] Emanuel Istrate, Sjoerd Hoogland, Vlad Sukhovatkin, Larissa Levina, Stefan Myrskog, Peter W. E. Smith, and Edward H. Sargent. Carrier relaxation dynamics in lead sulfide colloidal quantum dots. *The Journal of Physical Chemistry B*, 112(10):2757–2760, 2008.
- [183] Stuart A. Rice. Small angle scattering of x-rays. a. guinier and g. fournet. translated by c. b. wilson and with a bibliographical appendix by k. l. yudowitch. wiley, new york, 1955. 268 pp. 7.50. *Journal of Polymer Science*, 19(93):594–594, 1956.

# Appendix

## Photoluminescence Quantum Yield

Photoluminescence quantum yield (PLQY) is defined as the fraction of emitted photons per absorbed photons by a material.[181] It can be estimated by the PL decay rate

$$PLQY = \frac{k_{rad}}{k_{rad} + k_{nonrad}} \quad (8.1)$$

, where  $k_{rad}$  is the radiative decay rate and  $k_{nonrad}$  the nonradiative decay rate.

## Additional Raman Spectroscopy Measurements Data

If the incident photon contains the same energy as the excitonic energy transition, the scattered light becomes very strong. The enhancement of the Raman scattered light near an electronic transition is also known as resonant Raman scattering. In case of core/shell NCs the transition energy of the core differs from the shell. Changing the excitation wavelength can lead to the enhancement of either the shell or core-related LO frequency.

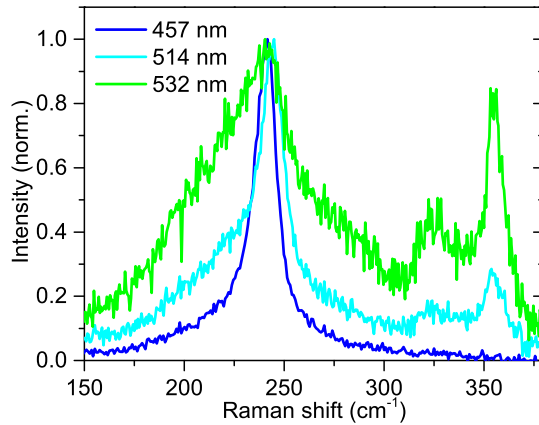


**Figure 8.1:** Raman spectra of InP/Zn<sub>0.98</sub>Cd<sub>0.02</sub>Se QDs measured with different excitation wavelengths. Changing the wavelength to 532 nm leads to a resolving the core-related band. Changing the excitation wavelength towards the shell electronic transition enhances the shell-related LO frequency.

(Reprinted (adapted) with permission from (Strain Engineering in InP/(Zn,Cd)Se Core/Shell Quantum Dots, Mona Rafipoor, Dorian Dupont, Hans Tornatzky, et al). Copyright (2018) American Chemical Society.)

To resolve the different LO frequencies of different QDs, the excitation wavelength was changed (Table 8.1).

**Table 8.1:** Raman spectroscopy was performed with different excitation wavelengths (and accordingly different spectral resolutions) for different samples.

Sample	Excitation wavelength (nm)	Resolution (cm <sup>-1</sup> )
InP	514	2.2
InP/ZnSe 0% Cd	458	4
InP/(Zn,Cd)Se 2.5% Cd	514	2.2
InP/(Zn,Cd)Se 5% Cd	514	2.2
InP/(Zn,Cd)Se 13% Cd	830	2
InP/(Zn,Cd)Se 21% Cd	532	4
InP/(Zn,Cd)Se 42% Cd	633 & 846	2.2
InP/(Zn,Cd)Se 70% Cd	830	2
InP/(Zn,Cd)Se 87% Cd	830	2
InP/(Zn,Cd)Se 98% Cd	830	2
InP/(Zn,Cd)Se 100% Cd	830	2

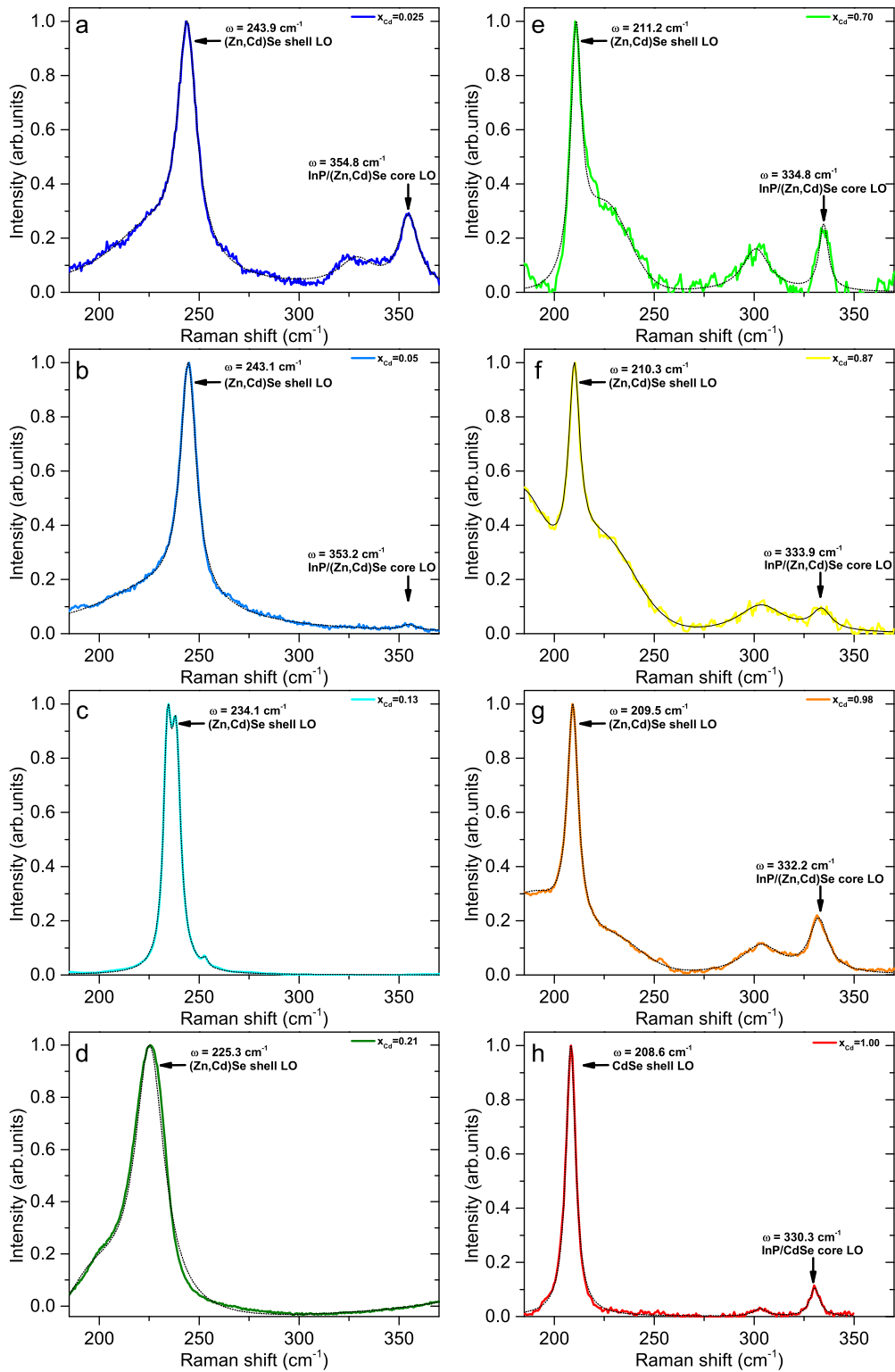


**Figure 8.2:** Raman spectra of a) InP/Zn<sub>0.98</sub>Cd<sub>0.02</sub>Se, b) InP/Zn<sub>0.95</sub>Cd<sub>0.05</sub>Se, c) InP/Zn<sub>0.87</sub>Cd<sub>0.13</sub>Se, d) InP/Zn<sub>0.79</sub>Cd<sub>0.21</sub>Se, e) InP/Zn<sub>0.30</sub>Cd<sub>0.70</sub>Se, f) InP/Zn<sub>0.13</sub>Cd<sub>0.87</sub>Se, g) InP/Zn<sub>0.02</sub>Cd<sub>0.98</sub>Se and h) InP/CdSe.

(Reprinted (adapted) with permission from (Strain Engineering in InP/(Zn,Cd)Se Core/Shell Quantum Dots, Mona Rafiqpoor, Dorian Dupont, Hans Tornatzky, et al). Copyright (2018) American Chemical Society.)

The shell-related LO of InP/Zn<sub>0.58</sub>Cd<sub>0.42</sub>Se QDs with an different excitation wavelength than the core-related LO. The core-related LO Phonon could be resolved under other condition (an excitation wavelength of 846.163 nm) and a longer longer integration time of 30 min). Changing the experimental conditions can also lead to the ligand-related organic vibrations, which are also Raman active, are also visible. The DFT calculations of the organic ligand molecules (oleic acid and dodecanethiol) shows a vibration around 347 cm<sup>-1</sup> for oleic acid. According to the DFT data the Raman bands around 340 cm<sup>-1</sup> are in a frequency region without organic vibrations. This asymmetric band was fitted in the same way as the common InP Raman bands with two Lorentzian functions.

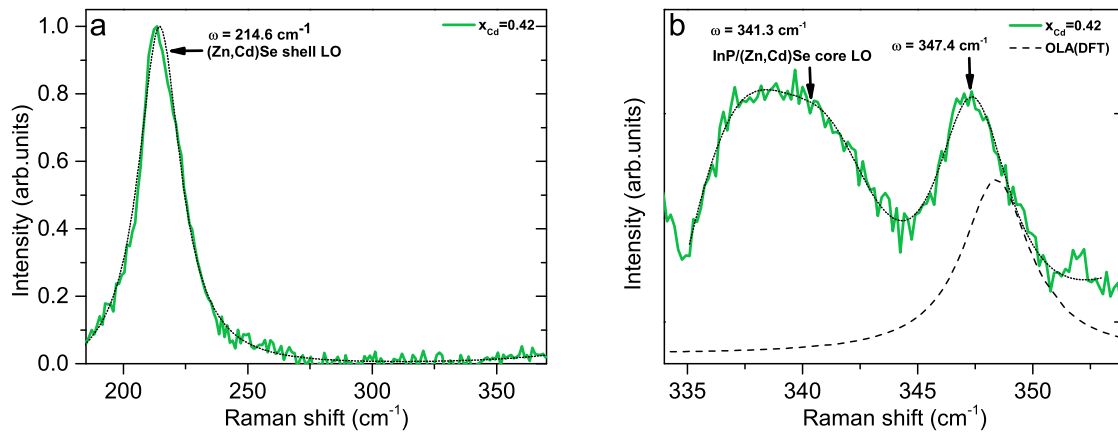


**Figure 8.3:** Raman spectra of InP/Zn<sub>0.58</sub>Cd<sub>0.42</sub>Se QDs a) in the region of the shell-related LO, measured with an excitation wavelength of 633 nm. b) In the core-related LO frequency region, measured with an excitation wavelength of 846.163 nm, the dashed curve are DFT calculations of oleic acid.

(Reprinted (adapted) with permission from (Strain Engineering in InP/(Zn,Cd)Se Core/Shell Quantum Dots, Mona Rafiqpoor, Dorian Dupont, Hans Tornatzky, et al). Copyright (2018) American Chemical Society.)

## Additional Photoluminescence Spectroscopy Measurements Data

The PL intensity of the single encapsulated QDs/QRs fluctuate during the experiment time, while the PL intensity of the clustered QDs/QRs remain constant.

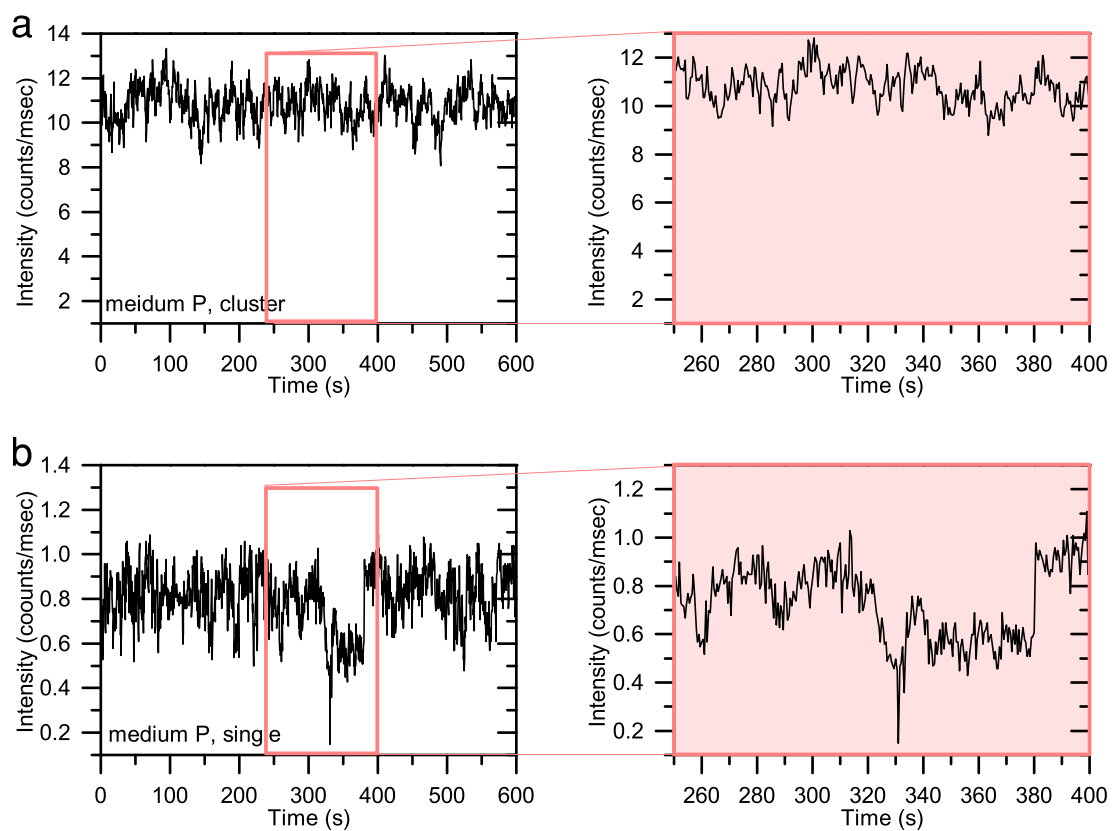


**Figure 8.4:** Time evolution of PL Intensity for a) clustered and b) single encapsulated QDs/QRs with medium polymer.

Reprinted (adapted) with permission from (Clustering of CdSe/CdS Quantum Dot/Quantum Rods into Micelles Can Form Bright, Non-blinking, Stable, and Biocompatible Probes, Mona Rafipoor, Christian Schmidtke, Christopher Wolter, et al). Copyright (2015) American Chemical Society.

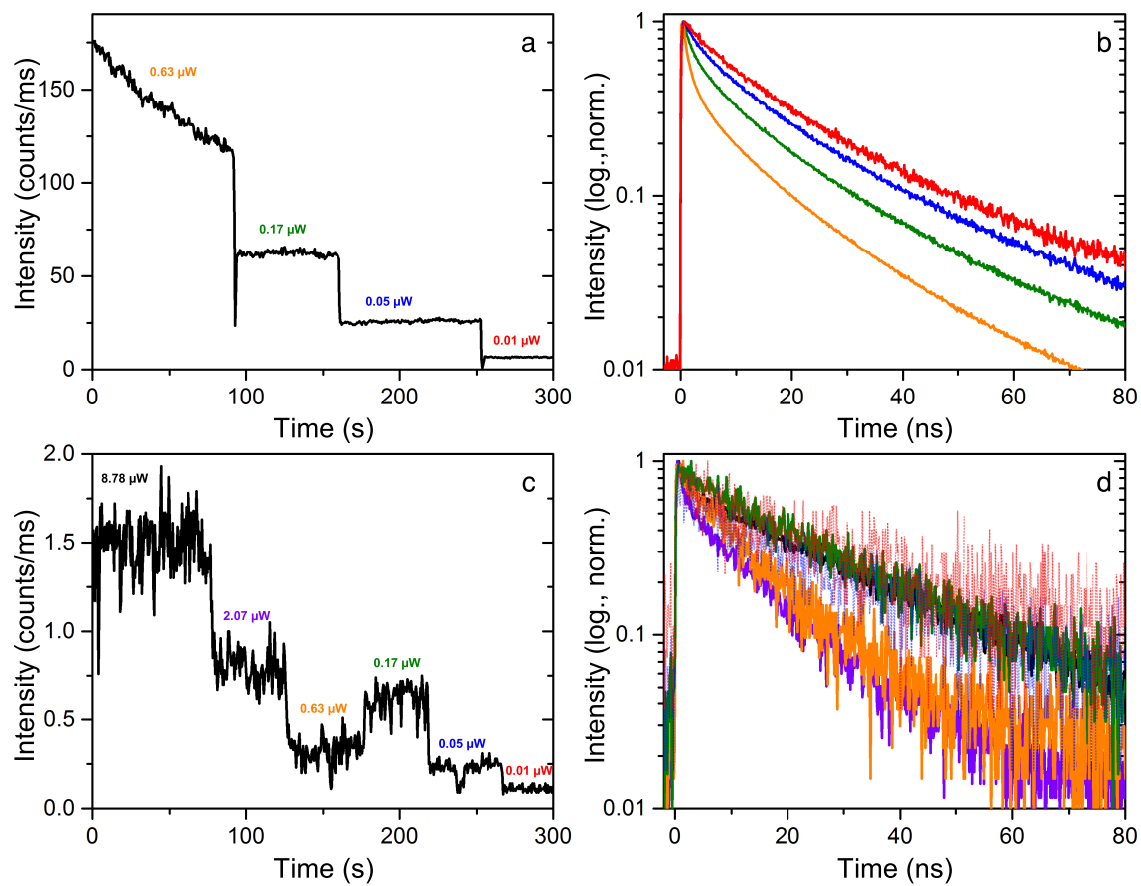


**Figure 8.5:** PL intensity traces for different excitation powers of a) medium polymer clustered QDs/QRs and c) medium polymer single QDQR and b) and d) the corresponding PL decays.

The extreme fast damping of the PL decay of the single encapsulated QDs/QRs by higher excitation power, is a sign of generating defects. The PL intensity vanishes in this case.

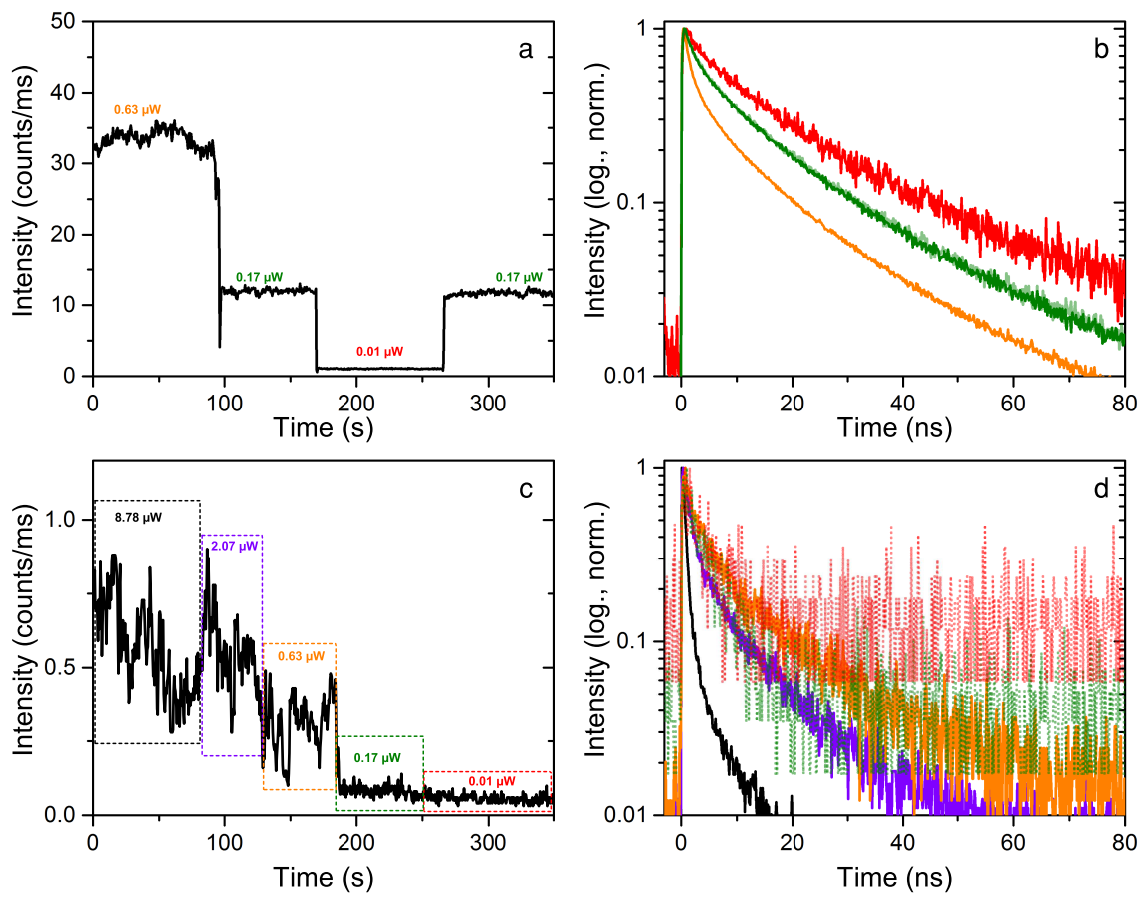


**Figure 8.6:** PL intensity traces for different excitation powers of a) small polymer clustered QDs/QRs and c) small polymer single QDQR and b) and d) the corresponding PL decays.

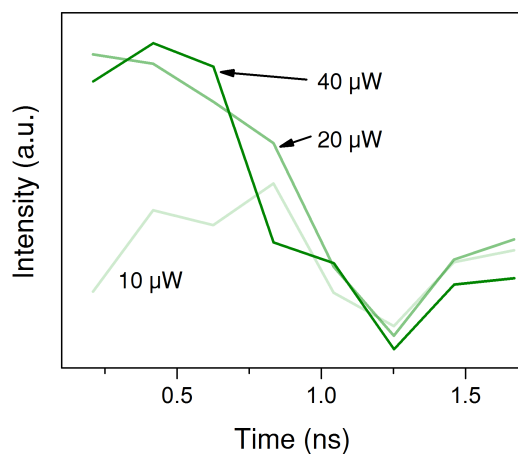


**Figure 8.7:** Spectral integrated PL decays of single NCs for different excitation powers. The data are normalized to the maximum intensity and the mono-exponential and biexponential components are removed. The onset of the three exciton regime is at 20  $\mu\text{W}$ .

## Additional Transient Absorption Measurements Data

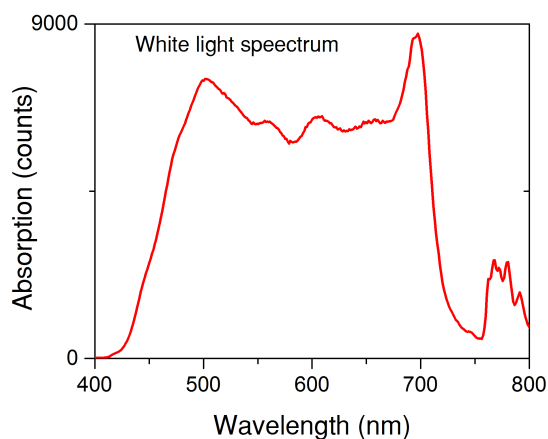


**Figure 8.8:** The white light probe pulse probes the system after the excitation by the pump beam.

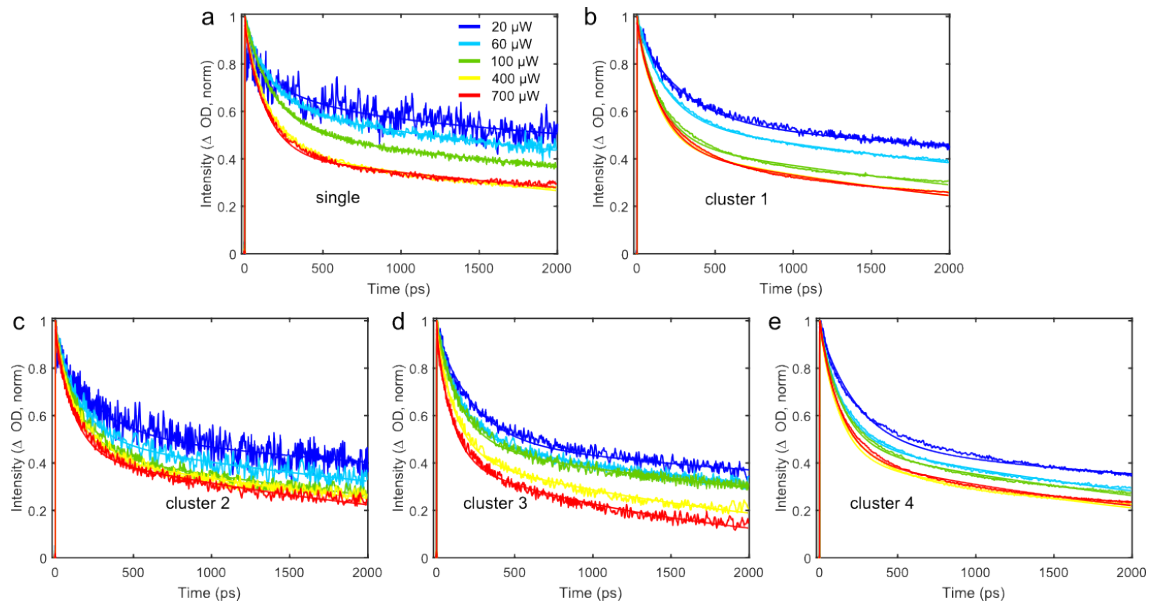


**Figure 8.9:** Increasing the excitation power leads to biexciton recombination. TA dynamics of a) single, b) cluster 1, c) cluster 2, d) cluster 3 and e) cluster 4.

The biexciton lifetime is instrument limited in the case of PL measurements. Thus from the TA dynamics (single QDs/QRs), one can estimate an biexciton lifetime of 180 ps.[182]

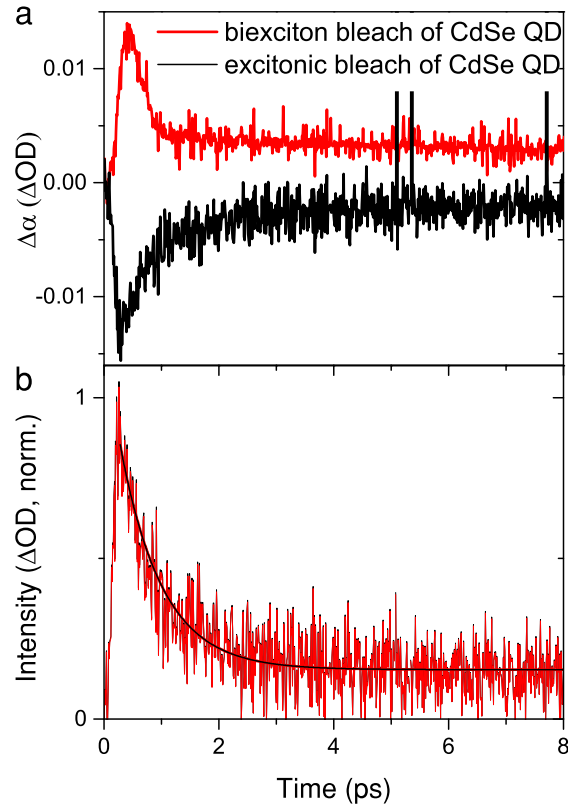


**Figure 8.10:** a) TA dynamic of CdSe excitonic bleach and the positive biexciton bleach (also seen in Figure 6.2 c at 497 nm). b) The TA dynamics in (a) normalized, one can see that the two bleaches have the same dynamic and the relaxation time is about 730 fs.

The CdSe excitonic bleach in Figure 6.2 has the same TA dynamic as the positive bleach at 497 nm. The positive bleach can be referred to the generation of biexciton in the higher energy levels (Figure 8.10).

## Scattering Vector

The scattered vector  $Q = k - k'$  is the difference between the wavevector of the incident beam  $k$  and the outgoing beam  $k'$ . In SAX measurements  $Q$  is estimated by the angle of the scattered light  $\theta$ . [183]

$$Q = \frac{4\pi}{\lambda} \sin \theta \quad (8.2)$$

The angle of the scattered light  $\theta$  depends on the wavelength  $\lambda$  by Bragg's law via

$$2d \sin(\theta) = n\lambda, \quad (8.3)$$

---

where  $n$  is an integer and  $d$  is the distance between layers of atoms in a crystal.[25] From these two equations the center-to-center distance of the particles  $d$  can be estimated by the SAX measurements.

$$d = \frac{2\pi n}{Q} \quad (8.4)$$

## Chemicals

Table 8.2: Chemicals

Substance	GHS	Hazard Statements	Precautionary Statements
CdSe/CdS/ZnSe	02, 07, 08	225-304-315-336-361d-373-412	210-261-273-281-301-310-331
Cadmium(II)acetat	07, 09	332-312-302-400-410	273-302+352
Selen	06, 08	331-301-373-413	273-304-340
Toluol	02, 07, 08	225-361d-304-373-315-336-361d-373	210-301+310-331-302+352
Zink(II)acetat	07, 09	302-400-410	262-273

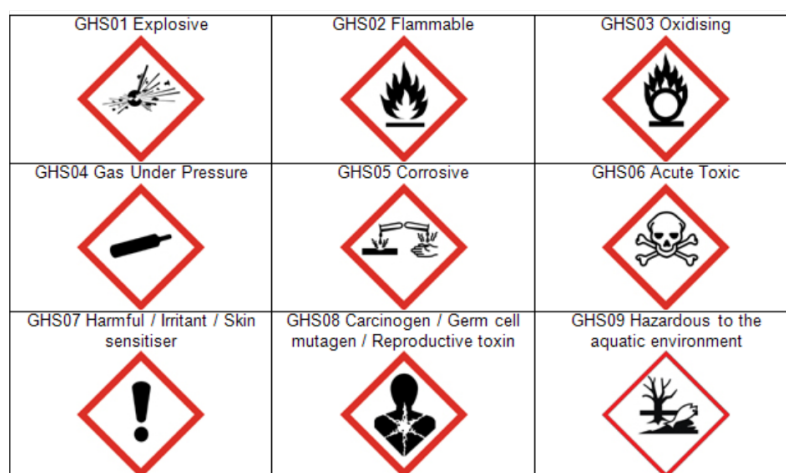


Figure 8.11: Pictogram Symbols

<http://findbestessayshere.info/msds-safety-symbols>

## Danksagung

Ich bedanke mich bei

- Prof. Dr. Holger Lange für die Möglichkeit in seiner Arbeitsgruppe meine Doktorarbeit anzufertigen und für die hervorragende Betreuung.
- Prof. Dr. Stephanie Reich für die Übernahme des Zweitgutachtens.
- Prof. Dr. Janina Maultzsch und Prof. Dr. Alf Mews dafür, dass sie mir ihre Labore zur Verfügung gestellt haben.
- Prof. Dr. Horst Weller und Prof. Dr. Zeger Hens für die gemeinsame Arbeit.
- Dr. Christian Strelow, Dr. Sandra Flessau und Hans Tornatzky für die Unterstützung in den optischen Laboren.
- Dr. Christian Schmidtke, Dr. Jan-Philip Merkl und Rieke Koll für die Nanokristalle.
- Dr. Stefanie Kietzmann und Michael Deffner für die Korrektur dieser Arbeit und die Hilfe mit Latex.
- Meiner Familie.

## **Eidesstattliche Versicherung**

Hiermit versichere ich an Eides statt, die vorliegende Dissertation selbst verfasst und keine anderen als die angegebenen Hilfsmittel benutzt zu haben.

Die eingereichte schriftliche Fassung entspricht der auf dem elektronischen Speichermedium. Ich versichere, dass diese Dissertation nicht in einem früheren Promotionsverfahren eingereicht wurde.

Hamburg, den 13. August 2018

Mona Rafipoor